Human Cardiac ^{31}P Magnetic Resonance Spectroscopy at 7 Tesla



Jane Ellis

St Edmund Hall

University of Oxford

A thesis submitted for the degree of

Doctor of Philosophy

Michaelmas 2020

Human Cardiac ^{31}P Magnetic Resonance Spectroscopy at 7 Tesla

Jane Ellis, St. Edmund Hall, Michaelmas term 2020.

This thesis is submitted for the degree of Doctor of Philosophy.

Abstract

Phosphorus Magnetic Resonance Spectroscopy (^{31}P-MRS) is unique in its ability to study high-energy phosphate metabolism noninvasively; when applied in the human heart, ^{31}P-MRS is a sensitive marker of the occurrence and progression of heart failure. To date, ^{31}P-MRS has been hindered by the inherent low signal-to-noise ratio (SNR) of acquisitions. In recent years, however, whole-body 7 T MRI scanners have brought a step change in the available SNR, increasing the precision of cardiac ^{31}P-MRS measurements.

The work in this thesis quantifies how the increased SNR afforded by using a 7 T scanner translates into improved reproducibility of human ^{31}P-MRS in the heart. A 'short' (6.5 minute) uttra-short echo chemical shift imaging (UTE-CSI) protocol is also established that is both sufficiently short and reproducible to allow multiple 7 T ^{31}P-MRS spectra to be acquired in the same scanning session. This 'short' UTE-CSI scan is used in a proof-of-principle study testing the feasibility of a using a commercially available ketone ester drink as a treatment for heart failure in diabetic subjects.

Finally, a novel multiple spin-echo ^{31}P CSI sequence is developed. The limitations of a low, varying transmit field are overcome by designing a novel composite refocusing pulse. While scanning restrictions due to the COVID-19 pandemic meant that this sequence is not yet tested *in vivo*, simulations are performed to explore the potential of this sequence to measure cardiac ^{31}P transverse relaxation times and further improve SNR of cardiac ^{31}P-MRS at 7 T.

Impact of disruptions caused by the COVID-19 pandemic

In March 2020, university buildings closed to non-COVID-19 research. The pandemic therefore altered the contents of this work, most notably in Chapter 8, where I develop a multiple spin echo ^{31}P 3D-CSI sequence.

Prior to the closure, I had performed simulations to design a sequence, and had programmed the proposed sequence into 'IDEA', Siemen's pulse programming environment. Owing to the pandemic, the following experiments were planned but were not possible to complete:

- Validating the designed refocusing pulse in a phantom.
- Validating the multiple spin echo sequence by comparing T_2 values measured in calf muscle to literature values.
- Testing the sequence by performing cardiac scans in 10 healthy subjects.

These planned experiments are discussed in detail in Chapter 8. There are plans for these experiments to be performed in spring 2021, which will hopefully enable T_2 values to be measured in the human heart at 7 T for the first time.

Acknowledgements

While I have been writing this thesis, the world has changed a lot. One constant, however, has been the support of the people around me, and for that I am truly grateful.

Thank you to my supervisor, **Professor Chris Rodgers,** and co-supervisor, **Dr Ladislav Valkovič**. In addition to being huge sources of MR knowledge and ideas, you are both (seemingly endlessly!) patient and fundamentally kind – a cocktail of qualities that have made you great supervisors. A special thanks to Chris: despite the 84 miles between Oxford and Cambridge, you never felt far away.

Thank you to **everyone at OCMR**; I've missed you all over the last year. **Liam:** while our conversations during the many overnight scanning sessions are fond memories, thank you for making me appreciate having a project of my own which allowed a sensible sleep schedule. Thank you also **Adrienne**, for sitting beside me and all your words of encouragement; watching you made me believe I could too. **Jack**, your enthusiasm is contagious. Thank you for all the ideas and advice.

I am grateful to **Dr Adrian Soto** for all his help with Chapter 7 and for the friendship that resulted from it. I am also indebted to **Vencel Somai** for the interesting discussions and input regarding refocusing pulses in Chapter 8.

A big thank you to everyone who has volunteered to be scanned over this project.

My family – Mum, Dad and Libby – thanks to you, I've never had far to fall. Your unfaltering support props me up in my most doubtful of moments.

Finally, Paolo. How lucky we are to have found each other; you mean the world to me.

Contents

1 Introduction 1

1.1 Motivation 1

1.2 Objectives 2

1.3 Thesis outline 2

2 Principles of magnetic resonance 5

2.1 Larmor precession 5

2.1.1 Classical description 5

2.2 Quantum mechanical description 7

2.3 Classical description 8

2.4 Excitation and reception 9

2.5 Relaxation 13

2.6 Reception 15

2.7 Chemical Shift 16

2.8 Localisation 17

2.8.1 Localisation methods 18

2.9 Analysis 22

2.9.1 Fourier transform 22

2.9.2 Phase correction 24

2.9.3 Apodisation 25

2.9.4 Zero filling 25

2.10 Combatting low SNR in a ^{31}P experiment 26

2.10.1 Hardware approaches 28

2.10.2 Sequence Modifications 29

2.11 Appendix A Acquisition weighting and the point spread function 32

3 ^{31}P-MRS and cardiac metabolism 36

3.1 Metabolism in the healthy heart 36
3.1.1 Substrate utilisation 37
3.1.2 Oxidative phosphorylation 38
3.1.3 ATP transfer and utilisation – the Creatine Kinase energy shuttle 39
3.2 Altered metabolism in heart failure 40
3.2.1 Heart failure aetiology 40
3.3 ^{31}P-MRS of the heart 43
3.3.1 The ^{31}P spectrum of the heart 43
3.3.2 Measurement parameters 45
3.3.3 Causes of signal contamination 51
3.4 Summary 52
4 Data acquisition 55
4.1 Hardware 55
4.1.1 MR Scanner 55
4.1.2 RF Coils 55
4.1.3 Performance comparison 56
4.2 Determining the *in vivo* B_1^+ performance of the Quad Coil 58
4.3 Data acquisition 59
4.3.1 ^{1}H localisation and shimming 59
4.3.2 Calibration scans 60
4.3.3 Base spectroscopy sequence 60
4.4 Data analysis 62
4.4.1 Saturation correction 63
4.4.2 Blood correction 64
4.4.3 Reporting PCr/ATP 64
5 Reproducibility of the existing cardiac 7 T ^{31}P MRS protocol 66
5.1 Experimental 67
5.1.1 Data acquisition 67
5.1.2 Data analysis 68

5.1.3 Assessment of reproducibility 68
5.2 Results 69
5.2.1 Analysis methods 69
5.2.2 Assessment of reproducibility 72
5.2.3 Power calculations and sample size 72
5.3 Discussion 73
5.3.1 Analysis methods 75
5.3.2 Assessment of reproducibility 76
5.3.3 Power and sample size 77
5.3.4 Limitations 78
5.4 Conclusion 78
6 Development of a short cardiac 7 T ^{31}P MRS protocol 80
6.1 Data acquisition 80
6.1.1 Per-subject shimming 81
6.2 Data analysis 82
6.3 Results 83
6.3.1 Per-subject shimming 86
6.3.2 Power calculations and sample size 89
6.4 Discussion 89
6.4.1 Assessment of reproducibility 90
6.4.2 Per-subject B_0 shimming 92
6.5 Conclusion 92
7 The effect of a ketone drink on cardiac energetics 95
7.1 Introduction 95
7.1.1 Background 96
7.1.2 The potential role of ketone bodies 97
7.1.3 Study design and hypothesis 98
7.2 Methods 98
7.3 Results 99

7.4 Discussion 102
7.5 Conclusions 104
8 A multiple spin-echo CSI sequence for ^{31}P MRS at 7 T 106
8.1 Background and motivation 107
8.1.1 Aim 1: MSE sequences to measure T_2 values 107
8.1.2 Aim 2: MSE sequences for SNR enhancement 107
8.2 Previous measurement approaches 110
8.2.1 Suitability of previous approaches for cardiac ^{31}P-MRS at 7 T 111
8.3 Refocussing pulse design 112
8.3.1 Methods 114
8.3.2 Results 118
8.3.3 Planned point-source phantom validation 120
8.3.4 Chosen refocusing pulse 122
8.4 Proposed ^{31}P MSE CSI sequence 122
8.4.1 Simulations 124
8.4.2 Planned in vivo experiments 128
8.5 Discussion 129
8.5.1 Refocusing pulse 129
8.5.2 MSE sequence 130
8.6 Conclusions 137
8.8 Appendix B Sequence implementations in IDEA 138
9 Conclusion and future work 140
9.1 Improved reproducibility of ^{31}P-MRS at 7 T 140
9.1.1 Specific achievements 140
9.1.2 Extensions and potential improvements 141
9.2 A multi-echo sequence for ^{31}P-MRS at 7 T 142
9.2.1 Specific achievements 142
9.2.2 Extensions and potential improvements 142
10 References 145

Publications

These pieces of work were produced during the same timeframe as the work in this thesis, although they are not necessarily represented in the following chapters.

Journal articles

[1] **Ellis J,** Valkovič L, Purvis LA, Clarke WT, Rodgers CT. Reproducibility of human cardiac phosphorus MRS (31P-MRS) at 7 T. *NMR Biomed*. 2019; **32**:e4095.

[2] Valkovič L, Clarke WT, Schmid AI, Raman B, **Ellis J**, Watkins H, Robson MD, Neubauer S, Rodgers CT, "Measuring inorganic phosphate and intracellular pH in the healthy and hypertrophic cardiomyopathy hearts by in vivo 7T ^{31}P-cardiovascular magnetic resonance spectroscopy", *J Cardiovasc Magn Reson*. 2019; **21**: 19.

[3] Apps A, Valkovič L, Peterzan M, Lau J, Hundertmark M, Clarke WT, Tunnicliffe L, **Ellis J**, Tyler DJ, Neubauer S, Rider OJ, Rodgers CT, Schmid A, "Quantifying the effect of dobutamine stress on myocardial Pi and pH in healthy volunteers: A ^{31}P MRS study at 7T", Magnetic Resonance in Medicine, 2020, **85**, 3, (1147-1159).

Conference abstracts

[1] **Jane Ellis**, Mabel Li, Michael Chappell, Mathew Robson, and Christopher Rodgers. Human cardiac creatine by CrCEST: potential improved fitting method. In: Proceedings of the 25th Annual Meeting of ISMRM; 2017

[2] Ladislav Valkovic, Alex Batzakis, **Jane Ellis**, Lucian Purvis, Albrecht I Schmid, Matthew D Robson, Dennis WJ Klomp and Christopher T Rodgers. Whole-body 7T 31P birdcage transmit coil driven by a 35kW RF amplifier with an integrated 30-element 31P receive array and an 8-element 1H transmit/receive array. In: Proceedings of the 26th Annual Meeting of ISMRM; 2018.

[3] **Jane Ellis**, Ladislav Valkovic, Lucian A. B. Purvis, William T. Clarke and Christopher T. Rodgers. Reproducibility of cardiac 31P MRS at 7 T. In: Proceedings of the 26th Annual Meeting of ISMRM; 2018.

[4] Ladislav Valkovic, Albrecht I Schmid, Lucian AB Purvis, **Jane Ellis**, Matthew D Robson, Stefan Neubauer, and Christopher T Rodgers. Quantification of human cardiac inorganic phosphate content in vivo by 31P-MRSI at 7T. In: Proceedings of the 26th Annual Meeting of ISMRM; 2018.

[5] Liam AJ Young, Carlo DL Ceresa, Jack Miller, Ladislav Valkovic, Daniel Voyce, Elizabeth M Tunnicliffe, **Jane Ellis**, Damian J Tyler, Peter J Friend, Constantin C Coussios, and Christopher T Rodgers. Assessing metabolism and function of normothermically perfused ex vivo livers by multi-nuclear MR imaging and spectroscopy. In: Proceedings of the 26th Annual Meeting of ISMRM; 2018.

[6] Liam AJ Young, Carlo DL Ceresa, Ferenc E Mozes, **Jane Ellis**, Ladislav Valkovic, Constantin C Coussios, Peter J Friend, and Christopher T Rodgers. Temperature sensitivities of T1, fat fraction and water resonance frequency characterised in ex vivo human livers. In: Proceedings of the 27th Annual Meeting of ISMRM; 2019.

[7] Ria Forner, Martijn Lunenburg, Quincy van Houtum, Ladislav Valkovic, **Jane Ellis**, Christopher T. Rodgers, and Dennis Klomp. Necessity for detuning large volume coils? In: Proceedings of the 27th Annual Meeting of ISMRM; 2019.

[8] Ladislav Valkovic, **Jane Ellis**, Lucian AB Purvis, Albrecht Ingo Schmid, Stefan Neubauer, and Christopher T Rodgers. First assessment of cardiac energy metabolism in the lateral and inferior segments of the left ventricle in vivo at 7T. In: Proceedings of the 27th Annual Meeting of ISMRM; 2019.

[9] **Jane Ellis**, Moritz Hundertmark, Marco Spartera, William Watson, Christopher T. Rodgers, and Ladislav Valkovic. Comparison of human cardiac 31P-MRS on 3 T Trio and Prisma scanners. In: Proceedings of the 27th Annual Meeting of ISMRM; 2019.

[10] Andrew Apps, Justin Lau, **Jane Ellis**, Mark Peterzan, Moritz Hundertmark, Damian Tyler, Albrecht Ingo Schmid, Stefan Neubauer, Oliver Rider, Ladislav Valkovic, and Christopher T Rodgers. Myocardial Pi/PCr and pH during stress at 7T with STEAM 31P MRS in dilated cardiomyopathy; heart failure beyond the ejection fraction. In: Proceedings of the 28th Annual Meeting of ISMRM; 2020.

[11] Andrew Apps, **Jane Ellis,** Justin Lau, Mark Peterzan, Damian Tyler, Albrecht Ingo Schmid, Stefan Neubauer, Oliver Rider, Christopher Rogers, Ladislav Valkovic. Quantifying Pi by STEAM 31P MRS provides novel insights in to impaired myocardial energetics and diastolic dysfunction in the diabetic heart. In: SCMR 23rd Annual Scientific Sessions; 2020.

[12] Andrew Apps, Justin Lau, **Jane Ellis**, Mark Peterzan, Moritz Hundertmark, Damian Tyler, Albrecht Ingo Schmid, Stefan Neubauer, Oliver Rider, Christopher Rogers, Ladislav Valkovic. Myocardial Pi and pH during catecholamine stress at 7T with STEAM 31P MRS in non-ischaemic cardiomyopathy; heart failure beyond the ejection fraction. In: SCMR 23rd Annual Scientific Sessions; 2020.

List of Figures

Figure 2.1 Larmor precession of a spin around an external magnetic field, B_0..... 7

Figure 2.2 A Energy level splitting for I=1/2. 8

Figure 2.3 the effect of B_1 excitation in the laboratory and the rotating frame of eference. 10

Figure 2.4. RF pulses and their corresponding response function in the frequency domain 11

Figure 2.5 Longitutindal and transverse magnetisation relax over time..... 14

Figure 2.6 Vector diagram of spin evolution in a spin-echo experiment. 15

Figure 2.7 The free induction decay (FID) of magnetisation following an excitation pulse. 16

Figure 2.8 Three free induction decays (FIDs) and the corresponding real part of the frequency domain spectra after the Fast Fourier transform (FFT) has been applied to the signal. 23

Figure 2.9 Absorption (real), dispersion (imaginary) and magnitude of a single peak. . 24

Figure 2.10 Effect of zero filling on a simulated triplet peak. 26

Figure 2.11 Magnetisation components of a fully relaxed experiment versus a steady state experiment. 31

Figure 2.12 Effect of discrete and truncated sampling on the real space image. 33

Figure 2.13 A unfiltered k-space sampling filtered using a Hamming window function 34

Figure 3.1. The three stages of human cardiac energy metabolism..... 38

Figure 3.2 Heart failure leads to changes in all three stages of ATP production 42

Figure 3.3 Cardiac ^{31}P-MRS spectrum from a healthy volunteer at 7 T..... 43

Figure 3.4 Variation in literature PCr/ATP measurements. 47

Figure 4.1 Photographs of the 7 T ^{31}P-MRS surface coils used in this thesis..... 56

Figure 4.2 A Transmit (B_1^+) performance of the 7 T ^{31}P surface coils at maximum transmit voltage as a function of distance from the coil and receive (SNR). 58

Figure 4.3 Bloch Siegert B_1 maps in the short axis view of the heart using the Quad coil at 7 T 59

Figure 4.4 Plot of a single TR in the UTE-CSI sequence. 62

Figure 5.1 Study protocol. 67

Figure 5.2 Position of the CSI matrix showing the rotation of the CSI grid in the short axis view of the heart and spectra from the corresponding coloured voxel marked on the localiser images 70

Figure 5.3 Variation in PCr/ATP value measured at 4 voxel locations 71

Figure 5.4 Bland altman plots for matched ^{31}P CSI protocols at 3 T and 7 T. 72

Figure 5.5 Intersubject variability between scans Error bars show ±1 SD 76

Figure 6.1 study protocol. 82

Figure 6.2 **A** Position of the CSI matrix showing the rotation of the CSI grid in the short axis view of the heart. Spectra from the corresponding coloured voxel marked on the localiser images 84

Figure 6.3 Variation in PCr/ATP value measured at 4 voxel locations and combinations of spectral sums of these voxels. 85

Figure 6.4 Spectra from the same scanning session acquired with tune-up and per-subject shim settings. 87

Figure 6.5 Inter-subject variability. 87

Figure 6.6 Bland–Altman plots of inter-session variability in PCr/ATP 88

Figure 7.1 The role of insulin in non-esterified fatty acid (NEFA) dynamics. 96

Figure 7.2 Activation of the UCP1 channel by fatty acids (via PPAR-α) lowers the proton gradient by allowing H^+ to return to the mitochondria, producing heat. 2) The reduced proton gradient leads to a drop in the production of ATP 97

Figure 7.3 Study protocol 99

Figure 7.4 Plasma concentrations of the ketone body β-OHB, non-esterified fatty acids (NEFA), glucose and lactate before and after the concentrations of ΔG. 101

Figure 7.5 Example of a typical midseptal cardiac ^{31}P spectra before and after consumption of ΔG 101

Figure 7.6 PCr/ATP before and after consumption of ΔG. 102

Figure 8.1 **A** Expected SNR enhancement by performing a weighted average of one FID and n symmetric echoes with fixed TR and T_1. 110

Figure 8.2 The AMESING (**A**) and composite-block refocusing (**B**) 111

Figure 8.3 Amplitude (black) and phase (red) modulation waveforms for the 8 refocusing pulses considered for the MSE sequence. 117

Figure 8.4 Simulation results indicating performance of refocusing pulse on $B_{1+} - \gamma\Delta B_0$ grids relevant to ^{31}P cardiac MRS in the human heart at 7 T. 119

Figure 8.5 Pulse sequence for 180º pulse phantom validation. 120

Figure 8.6 Sketch of expected signal as a function of B_{1+} in proposed phantom validation experiment 121

Figure 8.7 Sketch of expected signal as a function of frequency offset in proposed phantom validation experiment..... 122

Figure 8.8 Pulse sequence diagram of proposed ^{31}P MSE CSI sequence. Each TR is made up of five time intervals (TI), each centred on a different metabolite from the ^{31}P spectrum. 123

Figure 8.9 Amplitude (**A**) and phase (**B**) modulation waveforms of the 12ms sinc excitation pulse. **C** Simulated flip angle of sinc pulse on $B_{1+} – \Delta B_0$ grid relevant to ^{31}P cardiac MRS in the human heart at 7 T. 123

Figure 8.10 Simulated SNR enhancement using the COMP-SINC refocusing pulse in a multi echo sequence with a ΔTE = 45ms, TR=5s. 125

Figure 8.11 A Number of echoes vs. corresponding minimum TI to comply with 10 s SAR limitations. **B-D** Number of echoes vs. fitted T_2 at a range of SNRs..... 127

Figure 8.12 A Accuracy and **B** precision of Monte-Carlo T_2 fitting at a range of B_1^+... 128

Figure 8.13 Variation of T_2 with field strength.. 135

Figure 8.14 Screenshot of modified IR-FID sequence for phantom validation scans. 138

Figure 8.15 Screenshot of a single TI from the MSE CSI sequence using the selective COMP-SINC refocusing pulse..... 138

List of Tables

Table 2.1 IEC guidelines on 6 minute SAR and heating in human MRI studies..... 12

Table 3.1 Overview of peaks typically observed in human *cardiac* ^{31}P-MRS spectra. In molecules that contain multiple ^{31}P atoms, shaded cells correspond to peaks arising from the phosphorous atom of the corresponding colour indicated in the chemical structure..... 44

Table 3.2 Example cardiac PCr/ATP values in healthy volunteers reported in the literature. Values have been blood and saturation corrected. 46

Table 3.3 Sensitivity of PCr/ATP to 'normal' physiological variations and changes in disease. All measurements in humans. 48

Table 3.4 Summary of ^{31}P-MRS findings in heart failure 52

Table 4.1 7 T cardiac ^{31}P-MRS prior knowledge. Bounds are indicated by 'lower bound':'upper bound'. All peaks were fitted to a Lorentzian line shape..... 63

Table 5.1 Power calculations showing the sample size needed in a paired study to determine statistical significance (α = 0.05) for 28 min CSI sequence at 7 T, and 31 minute CSI sequence at 3 T, for a change of 0.2 in the measured PCr/ATP. 73

Table 5.2 Reproducibility values of human cardiac ^{31}P-MRS from the literature 74

Table 6.1 UTE-CSI sequence parameters for the established 28 minute CSI used in chapter 5, and the modified 6 ½ CSI acquisition in this chapter..... 81

Table 6.2 Power calculations showing the sample size needed in a paired study to determine statsitcal significance (α = 0.05) for both 28 min and 6.5 min CSI sequences at 7 T, and 31 minute CSI sequence at 3 T, for a change of 0.2 in the measured PCr/ATP..... 89

Table 8.1 Pulse length and relative SAR for all considered pulses. Relative SAR calculated as $B1 + 2dt$ where peak B_{1+} was the same for all pulses. Rows are grouped by target bandwidth of the refocusing pulse. 118

Table 8.2 Papers reporting attempts to measure T_2 values of ^{31}P metabolites in humans. Grey shaded cells indicate where a multi-echo sequence has been used to acquire data..... 132

List of common abbreviations

^{1}H	proton
^{31}P	phosphorus-31
θ	flip angle
γ	gyromagnetic ratio
ADC	analogue-to-digital conversion
ADP	adenosine diphosphate
AHP	adiabatic half-passage
AMARES	advanced method for accurate, robust and efficient spectral fitting
AMESING	adiabatic multi-echo ^{31}P imaging
ATP	adenosine triphosphate
B	magnetic field
B_0	static magnetic field
B_1	oscillating magnetic field
B_1^+ / B_1^-	B_1 in the positive / negative rotating reference frame
BISTRO	B_1-insensitive train to obliterate signal
BMI	body mass index
CR	coefficient of repeatability
CRLB	Cramér-Rao lower bound
CSI	chemical shift imaging δ chemical shift in ppm
CV	coefficient of variation
DCM	dilated cardiomyopathy
DFT	discrete Fourier transform
DICOM	Digital Imaging and Communications in Medicine data format
DM	diabetes mellitus
DRESS	depth-resolved surface coil spectroscopy
EM	electromagnetic

emf	electromotive force
FFA	free fatty acids
FID	free induction decay
FLASH	fast low angle shot
FOV	field of view
FT	Fourier transform
FWHM	full width at half maximum
HCM	hypertrophic cardiomyopathy
HF	heart failure
ISIS	image-selected in vivo spectroscopy
k-space	spatial wavelength i.e. Fourier transform of position
MR	magnetic resonance
MRI	magnetic resonance imaging
MRS	magnetic resonance spectroscopy
MSE	multiple spin echo
OXSA	Oxford Spectroscopy Analysis toolbox
PA	pulse acquire
PCr	phosphocreatine
Pi	inorganic phosphate
PSF	point spread function
RF	radiofrequency
ROI	region of interest
SE	spin echo
SAR	specific absorption rate
SD	standard deviation
SNR	signal-to-noise ratio
STEAM	stimulated echo acquisition mode
T	tesla

T_1	spin-lattice relaxation time
T_2	spin-spin relaxation time
T_2*	apparent T2
T2DM	type-2 diabetes mellitus
TA	total acquisition time
TE	echo time
TI	inversion time
TR	repetition time
UTE	ultra-short echo time
WSVD	whitened singular value decomposition

1 Introduction

1.1 Motivation

Heart failure (HF) is one of the most prevalent diseases in the UK. It is a debilitating condition that is often deadly: approximately 50% of people diagnosed with heart failure die within five years.[1,2] An expensive condition to treat, HF accounts for approximately 1-2% of the annual NHS budget.[3] It therefore constitutes a significant burden, both in terms of impact on quality of life, and in an economic sense.

Phosphorus magnetic resonance spectroscopy (^{31}P-MRS) is a useful tool, unique in its ability to study cardiac energy metabolism noninvasively. Altered energetics is widely acknowledged as a basic mechanism of HF. Over the last 40 years, ^{31}P-MRS has been found to be a sensitive marker of HF;[4] ^{31}P-MRS continues to give insights into the mechanism and causes of a range of cardiomyopathies.[5]

Despite its clear value, ^{31}P MRS is currently limited by the relatively low signal-to-noise (SNR) of acquisitions. To date, this has led to long acquisition times and meant that large cohorts have been required for studies. In recent years, whole-body 7 T MRI scanners have brought a step change in the available SNR, increasing the precision of cardiac ^{31}P-MRS measurements.[6] However, what this increased precision means in practice for studies is still being discovered. Furthermore, at 1.5 T and 3 T, chemical shift imaging to measure the phosphocreatine to ATP ratio has emerged as a typical ^{31}P-MRS approach. Using 7 T, many more possibilities are opened for advanced pulse sequence development to probe cardiac energy metabolism in greater depth.

1.2 Objectives

The aims of this thesis are therefore to quantify the benefits of the improved SNR available due to scanning at 7 T. I also seek further SNR improvements by the development of a spin-echo ^{31}P-MRS pulse sequence. My specific objectives were:

- Determining what the improved SNR at 7 T means in practice for future studies. Specifically, answering the following:
    - To what extent do SNR improvements translate into better reproducibility of PCr/ATP measurements? This will allow required sample sizes for future studies to be calculated.
    - Can the improved SNR be used to reduce ^{31}P-MRS acquisition times while still providing data of acceptable quality?
- Investigating the suitability of spin-echo methods as candidates for ^{31}P-MRS in the human heart at 7 T.

1.3 Thesis outline

The remainder of this thesis is organised as follows:

In **Chapter 2**, I cover the fundamental principles of magnetic resonance (MR), from the origins of MR signal to its localisation and analysis. Particular attention is paid to the experimental considerations for maximising SNR.

Chapter 3 contains a brief description of cardiac metabolism and the ^{31}P-MRS spectrum of the human heart. In the second half of this chapter I present a survey of human cardiac studies performed to date.

In **Chapter 4** I describe the standard ^{31}P measurement approaches used in this thesis. I give details of the MR hardware, the base ultra-short echo chemical shift imaging (UTE-CSI) 28 minute spectroscopy sequence, and analysis methods.

In **Chapter 5** I assess the reproducibility of the base UTE-CSI protocol in 10 healthy volunteers. The impact of the technical improvements gained by moving to 7 T are

illustrated by comparing the sample sizes and approximate scan costs of studies using a literature 3 T and this 7 T protocol.

I develop a short, 6½ minute, CSI scan in **Chapter 6** with the aim of it being both sufficiently short and reproducible to allow multiple 7 T ^{31}P-MRS spectra to be acquired in the same scanning session. This short CSI scan is used in **Chapter 7** to investigate the potential of a commercially available ketone drink as a treatment for heart failure in the diabetic heart.

In **Chapter 8** I develop a multiple-spin-echo ^{31}P-CSI sequence. Careful attention is paid to the optimisation of a 180º refocussing pulse suitable for use with inhomogeneous B_1^+ produced by surface coils. This work had two aims: the measurement of cardiac ^{31}P T_2 values at 7 T and investigating the potential of using such an approach to improve SNR by combining signal from the free induction decay and echoes. Experiments in this chapter were interrupted by the COVID-19 pandemic and closure of university buildings: planned experiments that were unable to be completed are discussed in detail.

Finally **Chapter 9**, summarises the specific achievements of this thesis, and suggests areas for future work and development.

2 Principles of magnetic resonance

This chapter covers the basic principles underpinning magnetic resonance spectroscopy (MRS) that are needed in the interpretation and understanding of results in later chapters. The primary reason that ^{31}P-MRS is not yet used clinically is that it is an SNR limited technique; careful consideration is therefore paid to the physical factors that SNR depends on, and acquisition approaches that can be used to improve SNR. The contents of this chapter are based on a number of sources that may be referred to for further details.[4,7–9]

2.1 Larmor precession

Atomic nuclei are made up of protons and neutrons which, collectively, are referred to as nucleons. Nucleons pair up, meaning that when the total number of protons and neutrons in a nucleus are both even, all nucleons will be paired in stable isotopes. When this is not the case, some of the nucleons will remain unpaired. This leads to a property known as nuclear spin, a form of angular momentum quantified by the spin quantum number I. Each unpaired nucleon contributes a value of ½ to I: for example, in the case of ^{31}P, 15 protons and 16 neutrons, leave 1 unpaired proton and $I = \frac{1}{2}$.

2.1.1 Classical description

In the classical approximation, the angular momentum around the spin axis is described by:

$$J = \hbar I \, .$$

[2.1]

In many respects, this nuclear spin appears like an orbiting charge that creates a magnetic moment μ around the nucleus, such that:

$$\mu = \gamma J.$$

[2.2]

γ is the gyromagnetic ratio and is a constant for any given nucleus. The units of γ are $rad\, T^{-1} s^{-1}$. In the absence of an external magnetic field, the magnetic moments will have a random orientation. When placed in an external magnetic field, B_0, the moments will alter their orientation according to:

$$\frac{d\mu}{dt} = \mu\gamma \times B_0.$$

[2.3]

As the magnetic moment is constant, equation [2.3] shows that μ rotates about B_0 over time, which can also be described as follows:

$$\frac{d\mu}{dt} = \mu \times \omega_0$$

[2.4]

where ω_0 is known as the Larmor frequency. Combining equations [2.3] and [2.4] gives the well-known Larmor equation:

$$\omega_0 = \gamma B_0,$$

[2.5]

which describes the relationship of a nuclei's processional frequency to the field strength. It is conventional to express the gyromagnetic ratio in $\mathrm{MHz\,T^{-1}}$, so by this convention we can rewrite equation [2.5] as

$$f_0 = \frac{1}{2\pi}\gamma B_0.$$

[2.6]

In these units the gyromagnetic ratio of ^{31}P nuclei is equal to 17.24 $MHz\, T^{-1}$. Larmor precession is the fundamental physical basis of NMR.

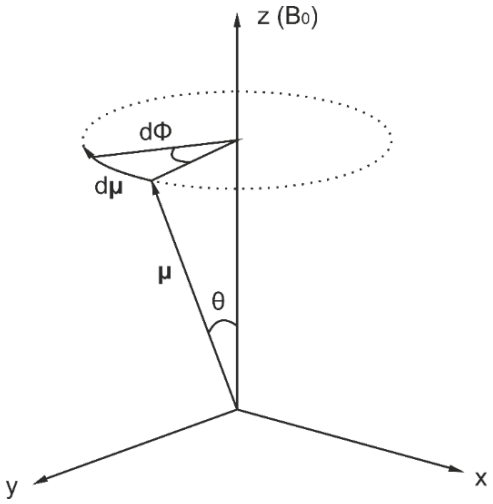


Figure 2.1 Larmor precession of a spin around an external magnetic field, B_0

2.2 Quantum mechanical description

In the quantum formulation, nuclei have $J_z = m_z\hbar$ where m varies from –I to +I in integer steps. This means that nuclei have 2I + 1 possible energy states in a magnetic field. Since ^{31}P has a spin $I = \frac{1}{2}$, a ^{31}P nucleus has two different energy states (Figure 2.2). The nuclei in the lower energy state have magnetic moments that are aligned with the direction of B_0 and are said to be in the α state, or 'spin up'. Those antiparallel to B_0 are higher in energy and in the β state or 'spin down'. In the specific case where $I = \frac{1}{2}$, the difference, ΔE, between these energy states is given by:

$$\Delta E = \gamma\hbar B_0.$$

[2.7]

The proportion of spins in each of the energy levels will therefore depend on the magnitude of the magnetic field and also the thermal energy of the nucleus in question. This proportion is given by:

$$\frac{N_l}{N_u} = e^{\frac{\Delta E}{kt}},$$

[2.8]

Where N_l and N_u are the number of spins in the lower and upper energy levels, k is the Boltzmann constant ($k = 1.381 \times 10^{-23}\, JK^{-1}$) and T is the temperature in kelvin (K). In

MRS, the difference in these two population sizes is of interest. This can be approximated by:

$$\frac{(N_l - N_u)}{N_u} \approx \frac{\hbar\omega_L}{kT} = \frac{\hbar\,\gamma B_0}{kT}.$$

[2.9]

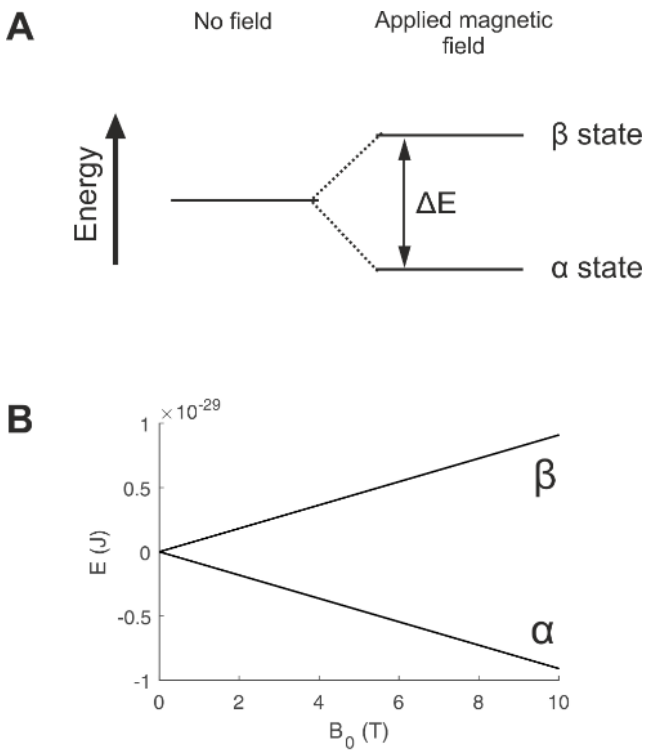


Figure 2.2 A Energy level splitting for I=1/2. **B** Energy difference in α and β states of a ^{31}P nucleus as a function of field strength.

2.3 Classical description

The previous section described the behaviour of a single spin (nucleus) in the presence of a magnetic field. However, in an NMR experiment, we do not observe just one nucleus, but a large collection and it is the net behaviour of all of them that we measure. While we need quantum mechanics to describe the behaviour of a single spin, the net behaviour of all the observed spins can be described well by classical mechanics in many instances. This net magnetisation, M, is equal to the sum of the individual magnetic moments:

$$M = \Sigma\, \mu.$$

[2.10]

If the magnetic moments of each of the individual nuclei are all pointing in random directions, then they will cancel each other out. However, in an applied field, there will be a net magnetisation along the line of B_0. This magnetisation can be represented by the magnetisation vector M. This is the sum of the individual magnetic moments. We can generalise equation [2.3] to give the time dependence of the total magnetisation under the influence of B_0.

$$\frac{dM}{dt} = M\gamma \times B_0.$$

[2.11]

In an MR experiment, we are detecting the precession of the magnetisation vector.

2.4 Excitation and reception

At equilibrium, the magnetisation vector precesses around B_0 at the Larmor frequency – there is no component of this magnetisation in the transverse, or xy, plane. In order to detect signal, it is necessary to 'tip' the magnetisation away from the direction of B_0 into the transverse plane. This is done by applying a magnetic field oscillating at the Larmor frequency (an RF pulse) perpendicular to the direction of B_0 – a field that is termed B_1 or sometimes more specifically B_1^+. When an RF pulse is applied, the spins will precess about both the static B_0 and the irradiating B_1 fields. If the B_1 is applied for long enough, the spins will obtain a non-random orientation with a component in the xy plane – at the molecular level, spins are said to have gained phase coherence. However, it's fine for us to think of this process as the magnetisation vector being tipped away from the longitudinal axis. The angle that $\boldsymbol{M}$ is tipped away from the z axis is known as the flip angle, α.

Until now, we have described the precession of the magnetisation vector in the 'laboratory frame'. It is, however, easier to define a new coordinate system: the 'rotating frame'. Here, the effects of B_1 are clearer. As the name might suggest, the rotating frame rotates around

B_0 at the Larmor frequency, meaning that B_1 appears static (if circularly polarised). Excitation of magnetisation in the rotating frame is depicted in Figure 2.3B.

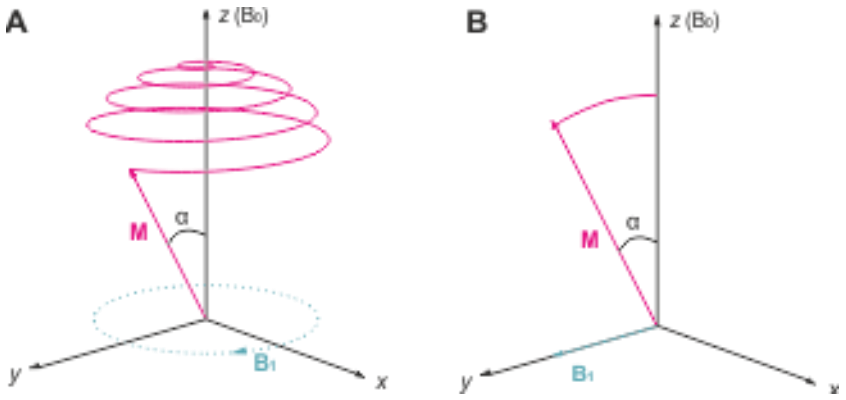


Figure 2.3 the effect of B_1 excitation in **A** the laboratory frame of reference and **B** the rotating frame of reference.

In the rotating frame, the frequency Ω at which the magnetisation vector rotates around the z axis will be different from the Larmor frequency, ω_0. Using the Larmor equation [2.3], it therefore follows that the apparent static magnetic field will be different too:

$$\Delta B = -\frac{\Omega}{\gamma}. \qquad [2.12]$$

We call the apparent field, ΔB, the reduced field. From equation [2.12], we can see that when the rotating frame is rotating at the Larmor frequency (i.e. $\Omega = 0$), the reduced field will also be zero. This helps us to understand how a much weaker B_1 field (on the order of μT) is able to tip $\boldsymbol{M}$ away from the direction of B_0 (on the order of T): as frequency of an RF pulse becomes close to Larmor frequency (i.e. we are on resonance), ΔB approaches zero and the B_1 field becomes dominant in the rotating frame.

The simplest RF pulse is a block, or hard, pulse – a pulse of duration, τ, that has constant amplitude and phase relative to the RF waveform. The bandwidth of a block excitation pulse is inversely proportional to the length of the pulse.

A shorter, pulse therefore excites a larger bandwidth. The frequency response of a pulse is given (neglecting relaxation) by the Fourier transform of its time domain envelope, shown

in Figure 2.4. Another common pulse is a sinc pulse, which is an example of a selective pulse (ideally constant for frequencies of interest and zero elsewhere). A sinc function is infinite, so in practice needs to be truncated.

RF pulses can be designed according to requirements – for example, they might need to be frequency selective while also being insensitive to variations in the B_1 field amplitude in terms of the flip angle they produce (adiabatic) or even selectively excite multiple frequencies. Considerations of RF pulse design for a refocusing (180º) pulse are discussed more in Chapter 8.

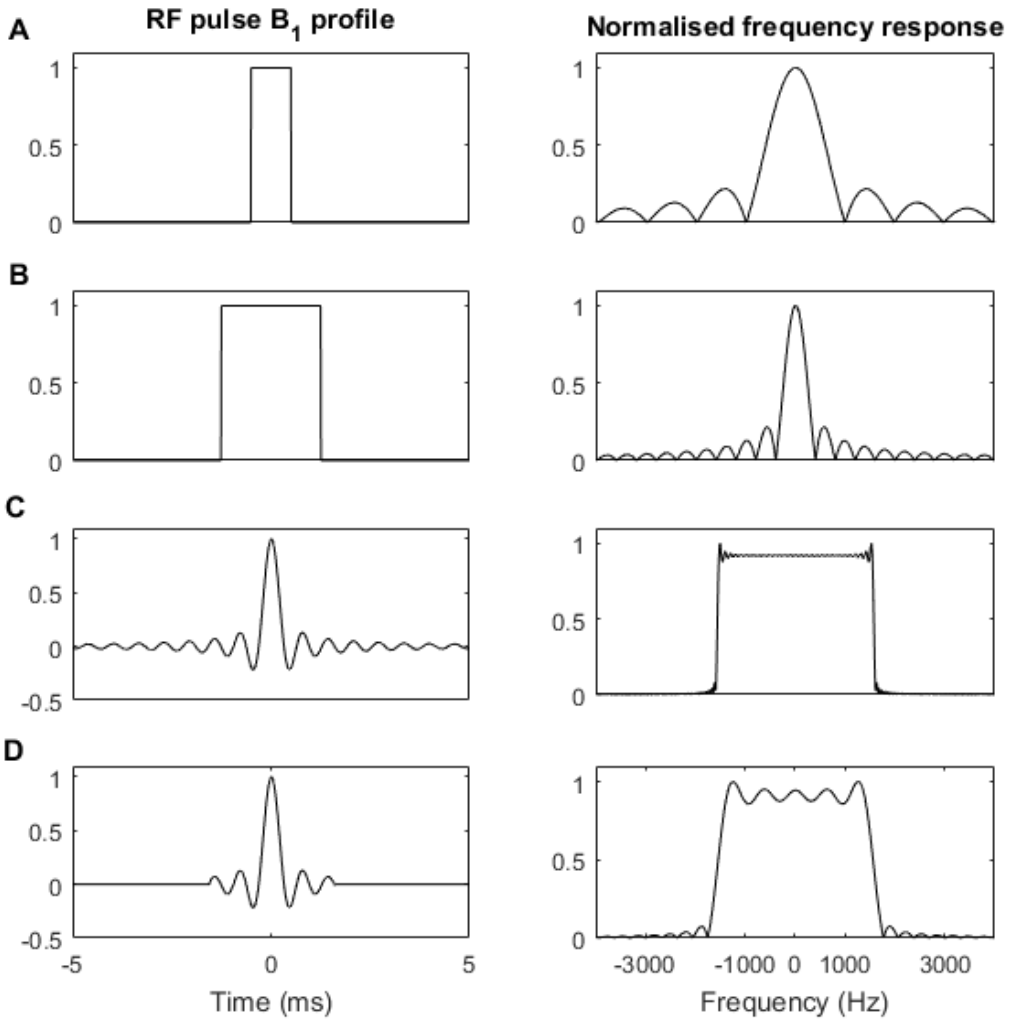


Figure 2.4. RF pulses (left) and their corresponding response function in the frequency domain (right). (a) shows a 1 ms hard pulse. (b) shows a 2.5 ms hard pulse, with the longer pulse duration corresponding to a narrower bandwidth. (c) shows a sinc pulse, which in practice needs to be truncated like in D.

When designing RF pulses, the amount of heat deposited in the body by the pulse is an important safety consideration. The electrical conductivity of biological tissue means that the transmitted RF magnetic field induces an electrical current in the tissue – the majority of which is transformed to heat. Sometimes tissue heating can reach a point where it becomes a safety concern. The power deposited during an RF pulse of length t is proportional to the square of the main magnetic field strength and the amplitude of the B_1:

$$P \propto \omega_0^2 \int_0^t B_1^2(t)$$

[2.13]

Deposited power is usually quantified by the specific absorption rate (SAR) – the mass and time normalised rate at which RF energy is deposited in biological tissue. The ω_0^2 term in equation [2.13] means that more heating is produced at higher static field strengths, so SAR considerations are more important as field strengths increase. In the UK the International Electrotechnical Commission (IEC) determines the maximum limits for SAR.[10] These limits are given as maximum values averaged over both a 10-second and 6-minute average. SAR is normally expressed in units of Wkg^{-1}.

The scanner predicts the SAR of a sequence depending on the B_1 profile of sequence, the participant's bodyweight and a coil specific scaling factor (the "k-factor"). Pulse sequences need to be designed within the constraints of these limits.

Table 2.1 IEC guidelines on 6 minute SAR and heating in human MRI studies.[10]

	Whole-Body Average	**Heat Average**	**Head, Trunk Local SAR**	**Extremities Local**
Normal	2 W/kg (0.5°C)	3.2 W/kg	10 W/kg	20 W/kg
Localized heating limit	39°C in 10 g	38°C in 10 g		40°C in 10 g

2.5 Relaxation

After an RF pulse has ended, magnetisation 'relaxes' back to the thermal equilibrium state. There are two distinct relaxation process: spin-lattice and spin-spin relaxation.

Spin-lattice relaxation

Spin lattice relaxation is the process of the longitudinal component of the magnetisation, M_z, returning to its equilibrium value, M_0. Spins give up energy to their surroundings (the "lattice") at a rate that is characterised by time constant T_1. M_z recovers according to:

$$\frac{dM_z}{dt} = -\frac{M_z(t)-M_0}{T_1}.$$

[2.14]

Mathematically, T_1 is the time required for M_z to return from zero to 63% of the value of M_0.

Spin-spin relaxation

Spin-spin relaxation describes how spins return to their equilibrium random phase orientation, causing the transverse magnetisation (M_{xy}) to decay. This dephasing is characterised by time constant T_2.

$$\frac{dM_x}{dt} = -\frac{M_x(t)}{T_2}$$

[2.15]

$$\frac{dM_y}{dt} = -\frac{M_y(t)}{T_2}$$

[2.16]

Magnetic fields produced by nuclei interacting with those of surrounding nuclei ("spin-spin") result in local, random, time-dependant field variations when the molecules rotate relative to one another or translate relative to one another. This causes intrinsic T_2 decay. Field variations cause nuclei to process at slightly different frequencies and spins to dephase. The magnitude of the transverse magnetisation ($M_{xy} = M_x + iM_y$) decays according to:

$$M_{xy}(t) = M_{xy}(0)e^{\frac{-t}{T_2}}.$$

[2.17]

In practice, observed transverse relaxation originates from two sources of dephasing: the intrinsic T_2 decay as well as additional dephasing caused by local, fixed, inhomogeneities in B_0. Such variations in B_0 can arise from the MRI scanner, or the presence of paramagnetic substances such as iron. The combination of both of both intrinsic T_2 decay and local variations in B_0 can be characterised by the time constant T_2^*:

$$\frac{1}{T_2^*} = \frac{1}{T_2} + \frac{1}{T_2'} \qquad [2.18]$$

Where T_2'' is the relaxation time of spins due to inhomegieties in B_0.

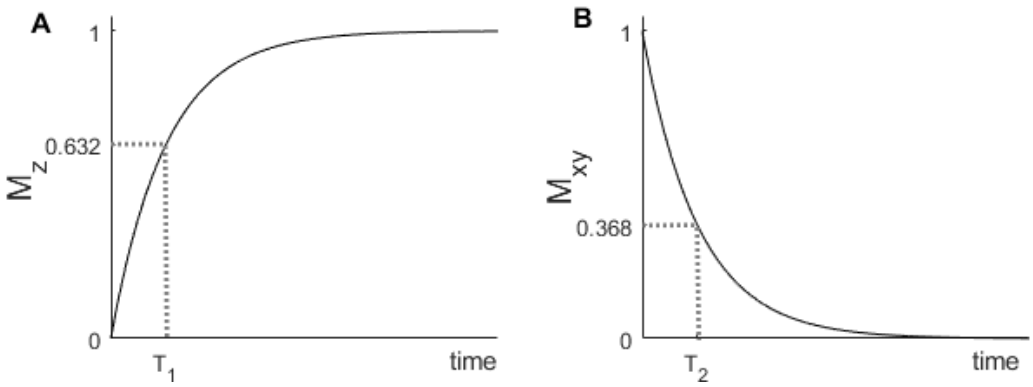


Figure 2.5 Longitutindal (**A**) and transverse (**B**) magnetisation relax over time.

It is possible to measure T_2. One approach is in a spin-echo experiment (Figure 2.6). After a 90º excitation, the spins start to dephase. In the rotating frame, this can be visualised as the spins 'fanning out' around the $+y$-axis. By applying a second RF pulse that inverts the spins 180º around the x-axis after a delay of TE/2, the phase of the spins is changed, such that $\phi \rightarrow \phi + \pi$. This means that after a period of time TE/2 the spins are refocused. The echo time (TE) is the time interval between the excitation and the spins refocusing to form an echo. We can measure T_2 by repeating this experiment at multiple echo times and fitting the measured signals to equation [2.17].

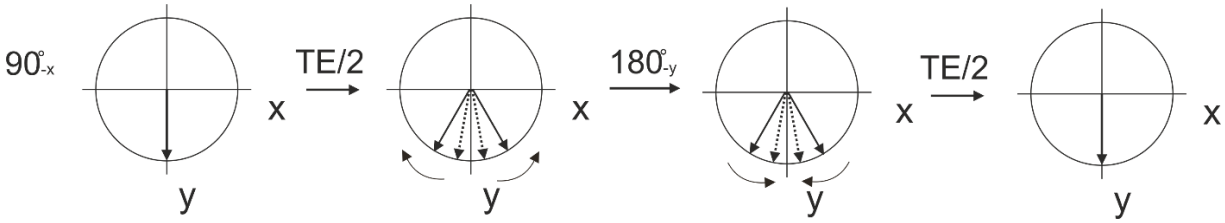


Figure 2.6 Vector diagram of spin evolution in a spin-echo experiment. **A** immediately following excitation, spins are in phase. **B** the spins lose their phase coherence

There are numerous physical mechanisms behind relaxation: common to all is the generation of fluctuations in the magnetic field. When NMR data is collected *in vivo,* the biological environment of ^{31}P metabolites will have a significant effect on the relaxation times. ^{31}P molecules will have a range of T_1 and T_2 values. Knowledge of relaxation times is important as they allow for the optimal choice in parameters for a given acquisition method. Understanding relaxation effects is also important for signal quantification when measurements are to be treated in absolute terms.

2.6 Reception

Following excitation, the magnetisation vector precesses around B_0 at the Larmor frequency. In order to detect signal, a receive coil is placed in the transverse plane where the precessing transverse component of the magnetisation vector induces an electromotive force (EMF). This EMF is measured as signal intensity. Over time, the EMF will decrease due to T_2^* relaxation. The time dependence of the EMF is known as the free induction decay (FID).

The FID is complex valued and can be represented by projections onto both the x-t and y-t planes:

$$M_x = M_0 \cos\left[(\omega_0 - \omega)t + \phi\right] e^{\frac{-t}{T_2^*}} \qquad [2.19]$$

$$M_y = M_0 \sin\left[(\omega_0 - \omega)t + \phi\right] e^{\frac{-t}{T_2^*}}$$

[2.20]

ϕ is the phase at $t = 0$. These projections ($M_x(t)$ and $M_y(t)$) are known as the real and imaginary components respectively.

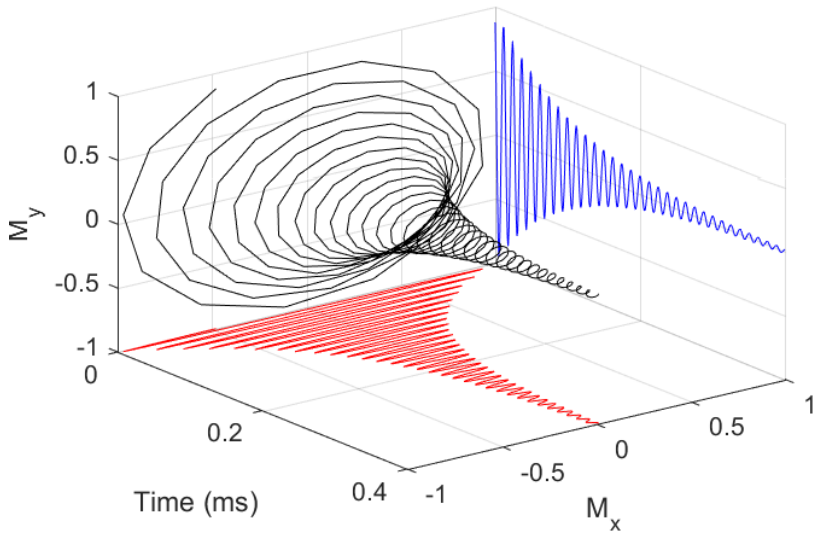


Figure 2.7 The free induction decay (FID) of magnetisation following an excitation pulse. M_{xy} decays with time constant T_2^*. The complex 3D FID (black line) can be represented by projections onto (M_x,t) and M_y,t. Which correspond to the real and imaginary components of the FID respectively.

2.7 Chemical Shift

The Larmor equation [2.5] depends only on γ and B_0, suggesting that the resonant frequencies of all nuclei of the same isotope will be identical. However, in practice this does not hold: the resonant frequency of a nucleus also depends on its chemical environment. This is due to a phenomenon known as shielding, which can be explained as follows.

Charged electrons orbit nuclei, inducing a small magnetic field that counteracts B_0, slightly reducing the field that a nucleus sees. We say that the nuclei are 'shielded'. In general, the more electrons that surround a nucleus, the greater the extent of the shielding. In molecules, the electron density surrounding a ^{31}P nucleus depends on properties of the surrounding atoms. This means that not all of the nuclei of the same isotope are shielded

to the same extent, leading to differing resonant frequencies for ^{31}P nuclei. The Larmor equation can be adapted to account for this by inclusion of a shielding constant, σ.

$$\omega = \gamma B_0(1 - \sigma)$$

[2.21]

Luckily, this is a beneficial effect as it allows us to distinguish between nuclei in different chemical environments; we can use MR to study different ^{31}P containing metabolites, rather than just total phosphorus.

So that we can compare the effect of shielding across different field strengths, we talk about 'chemical shift'. Chemical shift is the relative shift in frequency from a chosen standard and is given in parts per million (ppm):

$$\delta = 10^6 \frac{\omega - \omega_{ref}}{\omega_{ref}}.$$

[2.22]

2.8 Localisation

It is useful to be able to isolate signal originating from an organ or defined region of interest – there are a variety of different methods to localise signal from a specified volume of interest (a voxel). If a surface coil is used for excitation, the simplest method of localisation is to utilise the diminishing B_1 field with increased distance from the coil: signal can only come from a region that is close to the coil, as spins in regions that are further away are not excited. However, this approach is not specific to the target tissue and signal will be susceptible to contamination (e.g. from skeletal muscle in the chest wall or liver). This method can be suited to small loop coils, as the volume they excite is smaller and therefore the amount of contaminating tissue in the coils sensitive region will be less.

More sophisticated localisation methods employ spatially varying magnetic fields to alter the frequency of the spins in different regions:

Slice selection

A gradient, G, is applied during the excitation pulse. This means that only the targeted volume of excitation will have the same Larmor frequency as the excitation pulse and be excited. The portion of the spins excited is dependent on the bandwidth of the pulse.

Phase encoding

Phase encoding involves applying a gradient blip between excitation and signal acquisition, so that the phase of the signal will depend on the spatial location. Owing to the periodic nature of the localisation, areas outside the field of view (FOV) will have the same phase as those in the voxel. Attention therefore needs to be taken to avoid 'phase-wrap' artefacts.

Frequency encoding

A frequency encoding gradient is applied when the signal is received (i.e. during the ADC). By modifying the frequencies of the, this results in signal that has a spatial dependant frequency in the direction of the applied gradient. A disadvantage of frequency encoding methods are that chemical shift displacement artifacts will be present as the frequency differences due to chemical shift getting mixed with the spatial frequency differences.

2.8.1 Localisation methods

The following localisation methods have been applied to ^{31}P-MRS in the human heart: the choice of localisation method is often a balance between specificity of localisation and acquisition time.

DRESS

The first localised ^{31}P spectrum of the human heart was acquired using depth resolved surface coil spectroscopy (DRESS).[11] Slice-selective excitation in a slab parallel to the coil gives localisation in 1 dimension. Localisation in the other two dimensions is therefore determined by the B_1 profile of the coil. DRESS is therefore better suited to smaller surface coils, as there will be a smaller sensitive volume, minimising contamination from surrounding tissue.

CSI

Chemical shift imaging can be used to localise signal in 1-, 2- or 3-D. Phase encoding gradients are used in each required dimension to localise signal to multiple voxels.[12] The nominal resolution in a given dimension is given by:

$$\Delta x = \frac{FOV_x}{N} \quad [2.23]$$

where N is the number of phase encoding gradients in that dimension, and FOV is the field of view. The FOV must be large enough to cover the sensitive volume of the coil, otherwise signal from outside the field of view will 'wrap around' and be detectable within the CSI matrix. The number of acquisitions required to achieve an acceptable scan resolution quickly adds up – for example, a fully sampled scan with an 8x8x8 resolution, (i.e. eight phase encoding steps in each dimension) would require 512 acquisitions. CSI scans therefore often have long acquisition times.

CSI methods are preferably 'acquisition weighted', by the collection of more samples in the centre of *k*-space, or by using a Fourier series window (FSW) strategy in post processing.[13,14] Acquisition weighting is helpful as it reduces the 'ripple' in the point spread function (PSF, see Appendix A) but leads to a larger central lobe, meaning that the real voxel size is much larger than the 'nominal' voxel size that is defined in the scan parameters.

Compartmentalised spectroscopy

Compartmentalised spectroscopy methods including SLIM, SLAM and SLOOP build on a conventional CSI acquisition by incorporating prior knowledge about anatomical structure into the optimisation of phase encoding gradients.[15–17]

They rely on the assumption that one can split the sample into homogenous compartments with identical MR parameters. This assumption leads to a series of simultaneous equations. If a solution to these equations exists where the spatial function matches a compartment of

interest, the number of phase encoding gradients needed for an acquisition are reduced, reducing the minimum acquisition time required to achieve localisation.

Furthermore, as the spatial response function is exactly one within the compartment, and zero elsewhere, the acquired spectra can be used to measure absolute concentrations of metabolites. Of course, the assumption that chosen compartments are indeed homogenous *in vivo* does not entirely hold true, which can lead to signal contamination from outside the compartment.

STEAM

The single voxel spectroscopy using the Stimulated Echo Acquisition Mode (STEAM) method uses three sequential slice-selective 90^0 pulses applied in three orthogonal directions (i.e. with slice select gradients along three orthogonal directions). A stimulated echo (STE) is formed from the central 3D volume that has experienced all three RF pulses. The spacing of the three RF-pulses determines when the STE will occur: if the first two pulses are separated by time TE/2, the STE will appear at a time TE/2 after the third pulse. During the mixing time (TM) – the time between the second and third 90^0 pulse – the magnetisation is 'stored' along the z-axis and does not undergo T_2 decay. TM is usually kept to a minimum.

STEAM has been used as a localisation method for human ^{31}P-MRS studies in the heart.[18,19] However, STEAM suffers a 50% SNR penalty compared to spin-echo based methods because half of the spins do not form the stimulated echo.

ISIS

Image selected in vivo spectroscopy (ISIS) uses the addition and subtraction of multiple acquisitions to localise signal in 1-, 2-, or 3-D. A frequency selective inversion pulse is used in each dimension. Permutations of each of the pulses being 'on' or 'off' allow localisation. A non-selective 90^o pulse is used for excitation, followed by a FID readout. As multiple acquisitions are required (2^n, where n is the number of dimensions of localisation), ISIS is

sensitive to motion which tends to cause mis-assignment of signals between the different compartments.

PRESS

The point resolved spectroscopy (PRESS) sequence comprises a 90° slice-selective excitation pulse and two 180° slice-selective refocusing pulses applied alongside three orthogonal gradients (x, y, and z). This produces a spin echo at time TE resulting only from spins that have experienced all 3 RF-pulses.

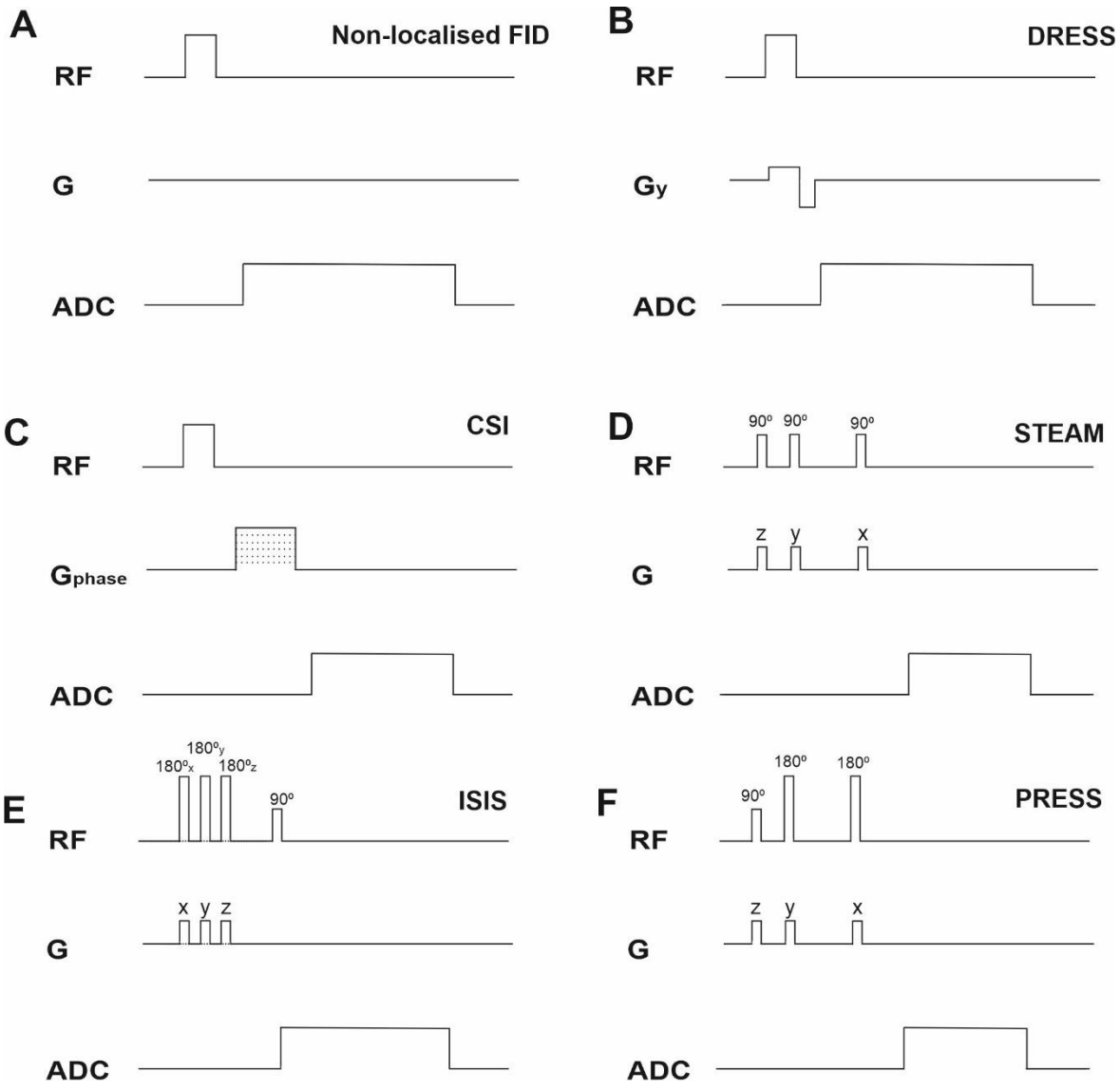


Figure 2.8 Pulse sequences. Each sequence shows the RF, gradient, and ADC (i.e. signal acquisition).

2.9 Analysis

2.10 Fourier transform

Data is collected in the time domain form of a FID (Figure 2.7): while these FIDs contain all the information about the frequency and intensity of a signal, they are usually not used directly. For ease of interpretation, the FID is usually converted into the frequency domain (a spectrum) by performing a Fourier transform. The frequency domain ($F(\omega)$) signal is given by:

$$F(\omega) = \int_{-\infty}^{\infty} f(t) e^{-i\omega t} dt$$

[2.24]

Where $f(t)$ is the signal in the time domain. Fourier transformation is a reversible operation – the frequency domain signal can also be calculated from the time domain signal by performing the inverse Fourier transformation:

$$f(t) = \frac{1}{2\pi} \int_{-\infty}^{\infty} F(\omega) e^{+i\omega t} d\omega$$

[2.25]

The real and imaginary components of the spectrum are as follows:

$$Re[F(\omega)] = A(\omega)\cos(\phi) + D(\omega)\sin(\phi)$$

[2.26]

$$Im[F(\omega)] = A(\omega)\sin(\phi) + D(\omega)\cos(\phi).$$

[2.27]

Where

$$A(\omega) = \frac{M_0 T_2}{1 + (\omega_0 - \omega)^2 T_2^2}$$

[2.28]

$$D(\omega) = \frac{M_0(\omega_0 - \omega) T_2}{1 + (\omega_0 - \omega)^2 T_2^2}$$

[2.29]

are the absorption and dispersion components of a Lorentzian line-shape.

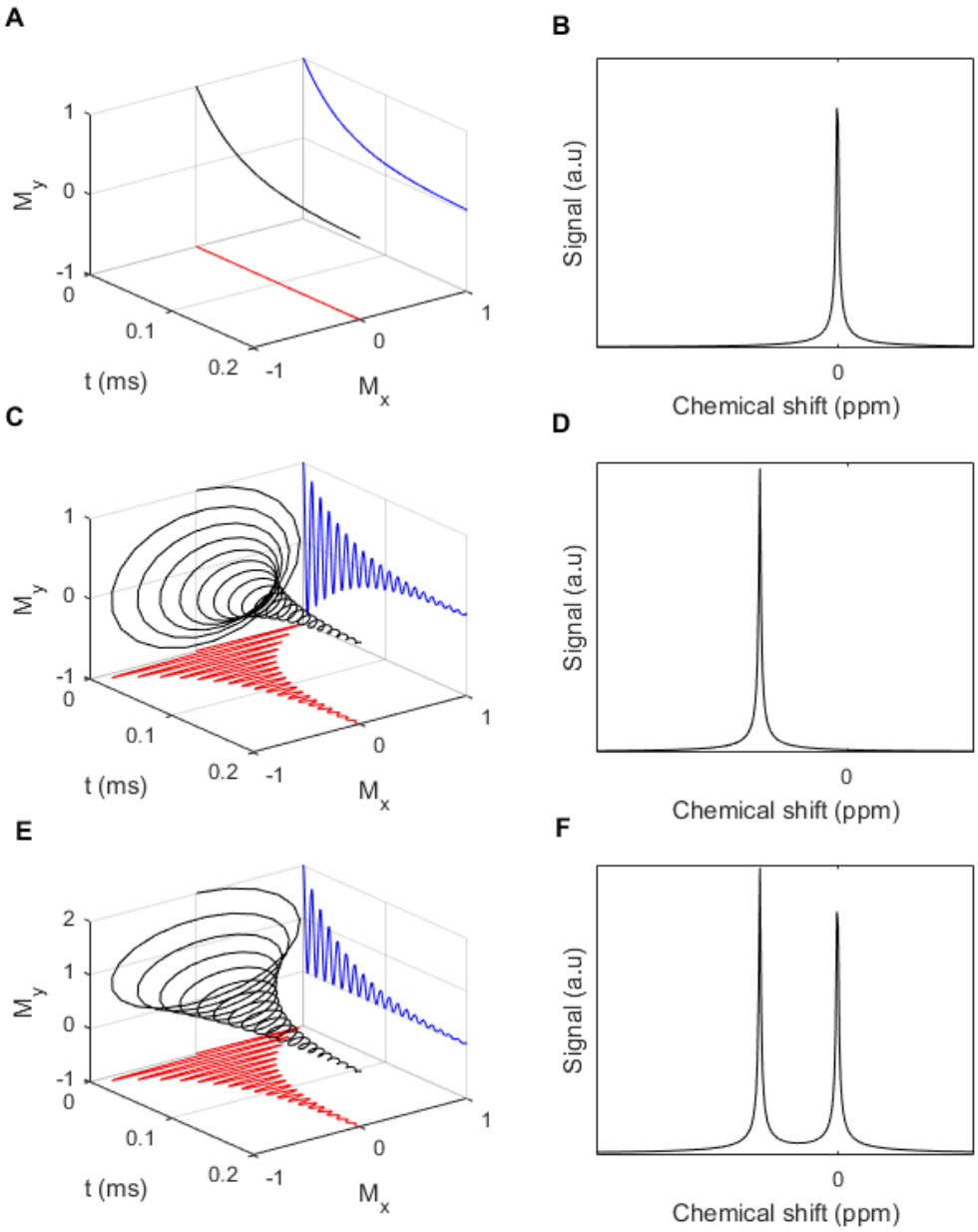


Figure 2.9 A,C,E Three free induction decays (FIDs) and the corresponding real part of the frequency domain spectra (**B,D,F)** after the Fast Fourier transform (FFT) has been applied to the signal. The FIDs contain signal from (**A**) a single on-resonance species, (**B**) a single off-resonance species, and (**c**) the sum of both signals.

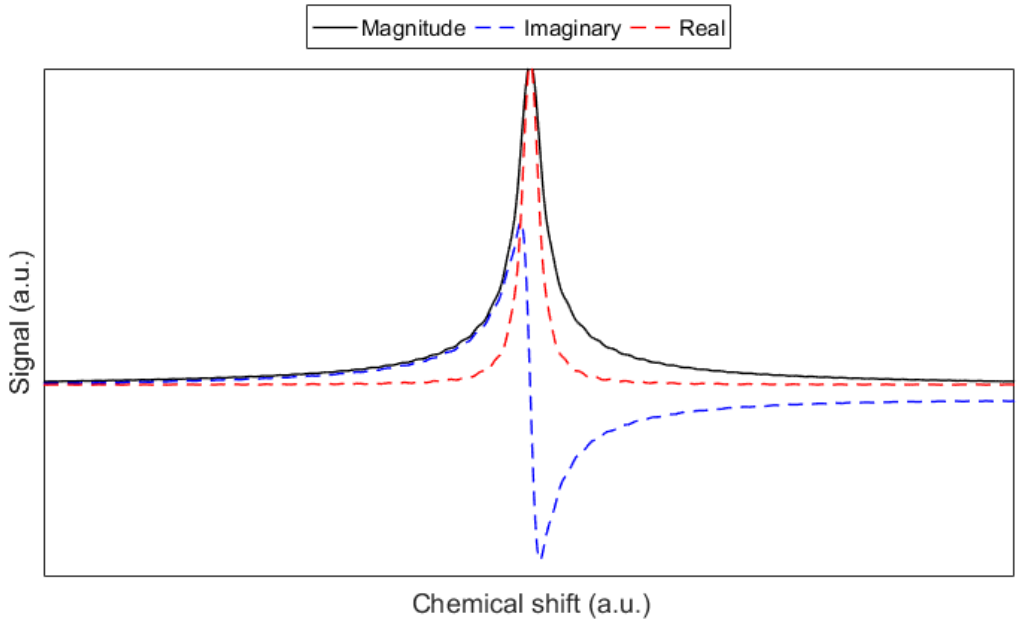


Figure 2.10 Absorption (real), dispersion (imaginary) and magnitude of a single peak.

2.10.1 Phase correction

Absorption mode spectra are desirable: the full width half maximum (FWHM) of the absorption component is $\frac{1}{\pi T_2}$, whereas the dispersion component is wider and has an integral of zero (Figure 2.10). Purely absorption mode spectra (i.e. $\phi = 0$) are rare – normally receive hardware or excitation pulses introduce 'zero order' phase offsets. Additionally, time delays between excitation and reception introduce a frequency dependant 'first order' phase offset. Both of these phase offsets can be corrected for, giving a predominantly absorptive spectrum:

$$A(\omega) = Re[F(\omega)]\cos(\phi_c) + Im[F(\omega)]\sin(\phi_c) \qquad [2.30]$$

where $\Phi_c = \Phi_0 + (\omega_0 - \omega)\Phi_1$, with Φ_0 the zero-order and Φ_1 the first order phase correction terms. Alternatively, if bigger spectral linewidths are acceptable, or it is not possible to perform phase correction, the magnitude information can be displayed:

$$M(\omega) = \sqrt{R(\omega)^2 + I(\omega)^2}\,.$$

[2.31]

2.10.2 Apodisation

Time domain filtering (refered to as apodisation) is a data processing step prior to Fourier transformation that can improve the SNR, or general appearance of a spectrum. Apodisation involves multiplying the time domain signal with a filter function: there are numerous possible filter functions, the choice depends on the desired sensitivity and resolution charactersistics.[20] One of the most commonly used is exponential weighting:

$$f(t) = e^{-t/T_w},$$

[2.32]

where T_w is a rate constant that determines the rate of decay of the filter function. Applying this filter improves the apparent SNR of the frequency domain spectra by reducing the contribution of points collected at the end of the FID that have higher relative noise than those at the beginning. However, as the function increases the rate decay of the FID, the resulting spectra will have broader linewidths – in effect, the observed T_2^* of the spectrum is reduced. Thus, there is an optimum value for T_w that is a balance between improved SNR and avoiding excessive line broadening. This occurs when the rate of decay of the filter is equal to the original rate of decay of the FID (i.e. when $T_w = T_2^*$) forming a so-called "matched filter".

2.10.3 Zero filling

Appending zeros to the end of the FID prior to Fourier transformation (zero filling) can greatly improve the apparent spectral resolution (Figure 2.11). If N points are sampled by the ADC from the FID, then the resulting spectrum after the discrete Fourier transform will also have N points. The intermediate frequencies of a peak are stored in the time domain data, but not displayed in the frequency domain owing to the Fourier transform only calculating the signal intensities at certain frequencies. One possibility to improve the spectral resolution would be extending the acquisition time of the FID, thereby increasing N and the number of points in the spectrum. However, this approach leads to unnecessary

addition of additional noise to the measurement after the signal has already decayed to zero, as well as increased data storage. Zero filling is a good solution: by simulating the decayed signal, extra points are added to the end of the FID without the addition of extra noise. Improvements from zero filling are limited however– only frequencies that are stored in the FID can be displayed and it cannot show data that was not collected at the outset.

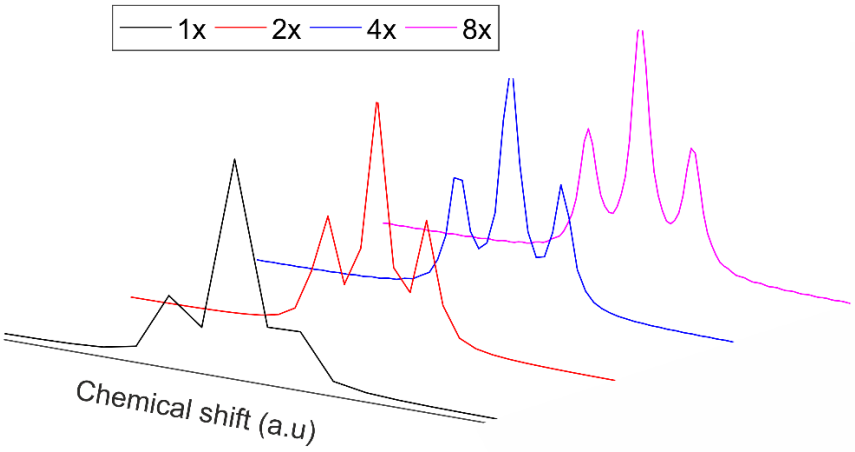


Figure 2.11 Effect of zero filling on a simulated triplet peak.

2.11 Combatting low SNR in a ^{31}P experiment

Signal to noise ratio (SNR) is one measure of the quality of a spectrum. In the MR literature there are multiple ways to define SNR: in the frequency domain, the SNR of a metabolite is often defined as the amplitude of a metabolite peak divided by the standard deviation of the noise from a region in the spectrum where there are no peaks. SNR can also be calculated from time domain data – here it is common to divide the average of the first few points of the FID by the noise at the end of the FID when all the signal has decayed away.[21] As SNR (along with the linewidth) determines the quality of the information that a spectrum can provide, the SNR of a proposed acquisition is a key consideration in experimental design.

^{31}P-MRS is primarily an SNR limited technique. Human ^{31}P-MRS has contributed to our understanding of metabolism by studying groups of healthy volunteers, or patient cohorts – it does not yet have the sensitivity to be used on a subject specific basis in the heart.

Therefore, despite having great value as a method uniquely able to probe ^{31}P energetics noninvasively (Chapter 3), the low SNR of acquisitions mean that ^{31}P-MRS is not yet used clinically.

The primary reason for the low SNR in ^{31}P-MRS is the low concentrations of phosphorous containing metabolites compared to tissue water imaged in conventional MRI. In the healthy heart, [ATP] and [PCr] are respectively approximately 6 and 10 $\mu molg^{-1}$ wet weight.[22] This compared to the tissue water—which that makes up 77% of the human body by weight – has a ^{1}H concentration of $86mmolg^{-1}$.

SNR has a quadratic dependence on gyromagnetic ratio, and so the lower gyromagnetic ratio of ^{31}P to ^{1}H ($\frac{\gamma_{^{31}P}}{\gamma^{1}H} = 0.40$) also contributes to the relatively lower SNR. After accounting for this sensitivity difference, the SNR of PCr in a cardiac ^{31}P experiment is about 1.9×10^{-5} times lower than the equivalent experiment on ^{1}H tissue water. Clearly, these SNR deficits need to be made up somehow.

More detail of ^{31}P-MRS specific acquisition methods in the heart are given in chapter 3; this section uses concepts introduced earlier in this chapter to explain the theoretical basis of some of the factors affecting SNR, and what specific approaches can therefore be taken to improve it. Many of the methods are a balance between improving SNR and maintaining satisfactory scan length, resolution and spectral linewidth.

2.11.1 Hardware approaches

Increasing magnetic field strength

SNR is approximately proportional to static field strength, B_0. The signal detected in the receive coil is proportional to B_0^2:

$$signal \propto \gamma^3 B_0^2$$

[2.33]

For an *in vivo* experiment, noise is dominated by noise from the sample, rather than noise from the electronics or the coil. Sample noise varies with ω_0 (i.e. γB_0). SNR can therefore be written as:

$$SNR \propto \gamma^2 B_0$$

[2.34]

Thus, from an SNR perspective, it is advantageous to use an MR scanner with the highest possible static field strength. However, higher field strengths are not without their challenges – they can bring major technical challenges and cost and require experiments to be redesigned.

Choice of RF coil

The coil used to excite and detect signal also has a large effect on SNR, and different coil designs have different strengths and weaknesses. The size of an RF coil and its distance from the tissue of interest are key in determining the sensitivity of a coil. In general, small coils have better SNR but are limited by the volume they can acquire – including the depth at which they cover. Larger coils excite a larger volume more uniformly, but this also means they detect noise from a larger region.

For a surface loop coil:

- Sensitvity drops off significantly with increased distance from the coil
- Penetration depth for reception is about 50-75% of the coil's diameter.

SNR is often considered when designing or choosing coils, and different coils can be used for excitation and reception. For example, using a large volume excitation coil together with a smaller surface coil for reception can give a good combination of a uniform excitation, while still benefitting from the better SNR of a small surface receive coil. Following the work by Hyde *et al*[23] and Roemer *et al*[24], it is also common to replace a single element receive coil with an array of smaller coils to give improvements in SNR as well as good anatomical coverage. These coils are called 'array coils' or 'receive arrays'.

2.11.2 Sequence Modifications

Voxel size

Voxel size is one of the primary determinants of SNR in an MR experiment. There is a linear relationship between the measurement volume and signal; the size of a peak is roughly proportional to the number of spins that give rise to it. Increased voxel sizes make the most significant contribution to bridging the gap between SNR in ^{31}P (or non-water ^{1}H) MRS and ^{1}H MRI experiments: for example, choosing a 5ml MRS voxel compared to a $0.05 \times 0.05 \times 0.3\ cm^3 = 7.5 \times 10^{-4}$ ml pixel used in ^{1}H MRI, yields an SNR improvement of approximately 13,000 times.

Larger voxel sizes are not without cost, however. The bigger the voxel, the lower the spatial resolution of an experiment, limiting the study of regionalised changes in ^{31}P metabolism. One of the primary measurements in ^{31}P MRS, the PCr/ATP ratio (§3.3.2.1), is not known to differ across the healthy heart[4], but there may be regional changes in disease. Perhaps more significant, is the increased susceptibility to contamination from other tissues (such as blood and muscle). Larger voxels are more likely to contain other tissues in addition to the one that is of interest – these other tissues can have similar, but different, spectra. The measured spectrum is a combination of contributions from all the spectra that are in the voxel. A more detailed discussion of 'signal contamination' is given in section 3.3.3.

Multiple averages

We can also improve the SNR of an experiment by increasing the number of averages (i.e. adding the FIDs from n consectutive measurements). The signal increases linearly with n averages, whereas noise only increases with $\sqrt{n}$, resulting in an SNR increase of $\frac{n}{\sqrt{n}} = \sqrt{n}$. Deciding the number of averages for ^{31}P-MRS experiments is a balance between good SNR and the practical consideration of scan length: n is proportional to scan duration T_A. This approach also has diminishing returns – to double the SNR of an acquisition, T_A needs to increase 4-fold, whereas if you wanted a 5x increase in SNR you would need 25 times more averages!

Increasing the transverse magnetisation

Signal is the component of the magnetisation vector that is in the xy plane. While a 90^0 will tip all of the magnetisation into the xy plane, this approach is not always optimal in terms of signal per unit time. This is because we need to wait for time $T_R > 5T_1$ before repeating the experiment – the majority of acquisition time is therefore spent waiting for the longitudinal magnetisation to recover by T_1 relaxation. However, if we repeat this experiment with a smaller excitation flip angle, α, the magnetisation follows the black line in Figure 2.12. In the first few transients, the M_z does not recover back to its starting value before the next excitation pulse tips it further away from the z-axis. After a few scans, the rate of relaxation by T_1 and the excitation become equal – the magnetisation has reached the 'steady state' and, even though the signal from each TR is less than would be the case where there was 90^0 excitation, overall the SNR per unit time is greater. In ^{31}P-MRS, most measurements are performed under this regime, owing to typically long T_1s of the metabolites of interest. The steady state is achieved by "dummy scans" prior to the measurement – in which the excitation pulses are played out but no FIDs are recorded.

The optimal angle (known as the Ernst angle) for SNR depends on the T_R of the sequence and the T_1 of the metabolite of interest. The Ernst angle therefore needs to be found for each specific experiment: [25]

$$\theta_E = \cos^{-1}(e^{\frac{-T_R}{T_1}})$$

[2.35]

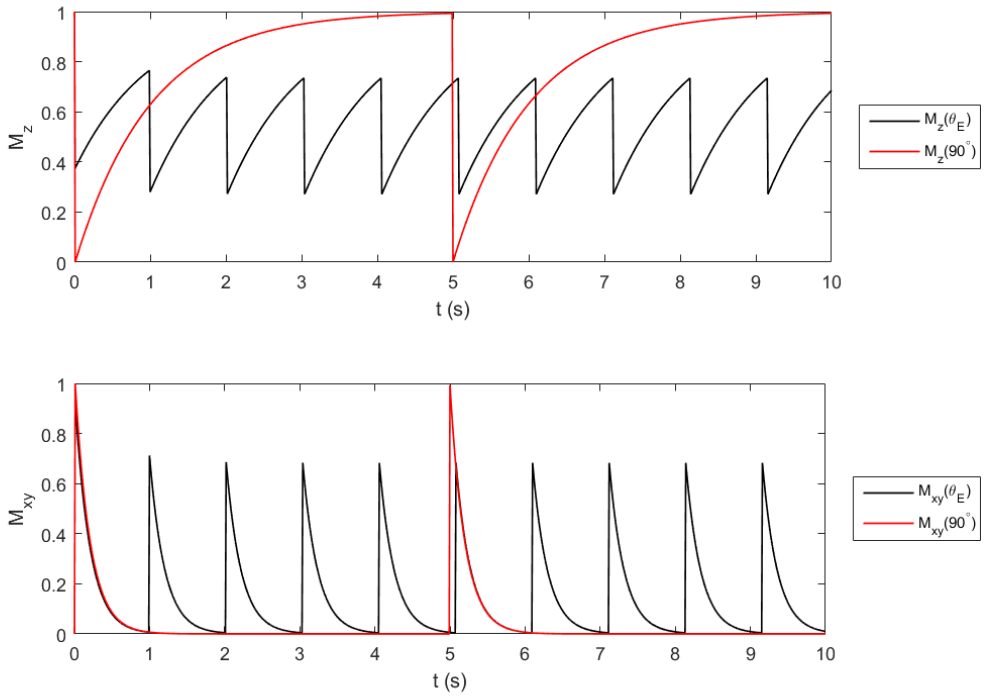


Figure 2.12 Magnetisation components of a fully relaxed experiment (red) versus a steady state (black) experiment.

Appendix A

2.12 Appendix A Acquisition weighting and the point spread function

Phase encoded data from a CSI acquisition can be Fourier-transformed to return the data to real space. For example, in 1-D:

$$f(x,\omega) = \int_{-\infty}^{+\infty} f(k_x,\omega)\, e^{-ik_x x} dk_x$$

[2.36]

Equation [2.36] assumes that k-space sampling is infinitely wide and occurs in infinitely small steps. In practice, sampling of k-space is both truncated (i.e. not infinitely wide) and discrete (in steps). We therefore need to substitute the Fourier transform for the discrete Fourier transform (DFT):

$$f(\Delta x,\omega) = \sum_{q=-N_x/2}^{\frac{N_x}{2}-1} F(q\Delta k_x,\omega) e^{-iq\Delta k_x \frac{x}{N_x}}.$$

[2.37]

Both discrete sampling and truncation affect the real space image (Figure 2.13). Discrete sampling introduces aliasing to the real space image – the image is repeated once every FOV. This means that we are unable to distinguish signal arising from outside the FOV from signal originating from inside the FOV that appears in the corresponding position.

Truncating can be thought of as a rectangular filter – when Fourier transformed this results in a sinc function. The combination of both of these effects is a repeating sinc function, known as the point spread function (PSF). The PSF tells us which voxels contain signal from a particular point in space. Or equivalently which points in space contribute signal to a particular voxel.

The PSF has positive and negative lobes. Particularly this anti-phase blurring can be hard to visualise intuitively when interpreting spectra. The PSF side lobes can be suppressed but at the cost of a wider central PSF lobe.

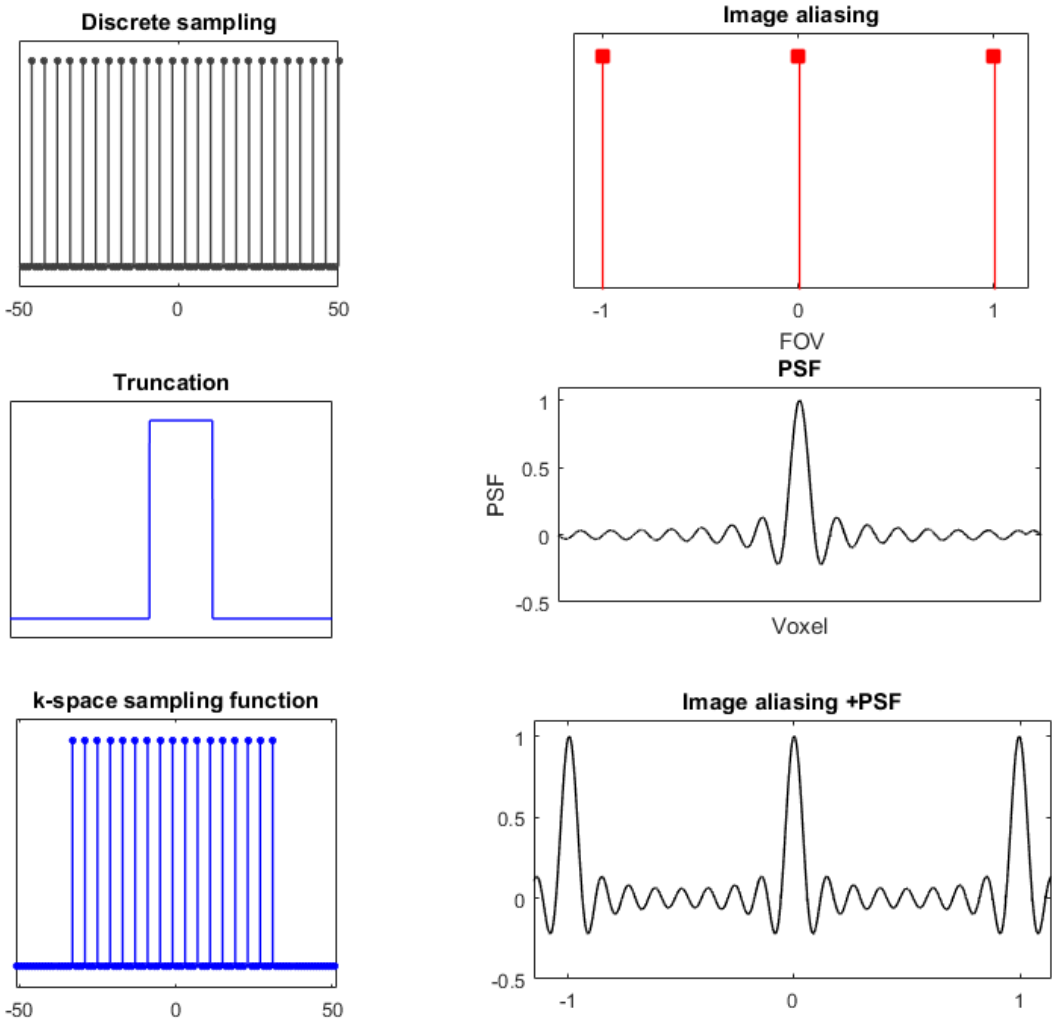


Figure 2.13 Effect of discrete and truncated sampling on the real space image.

The PSF has positive and negative lobes, making it hard to determine the relationship between the spatial origin of the signal and the signal intensity of a given voxel. Applying a Hamming window filter suppresses the lobes, but at the cost of a wider PSF (Figure 2.14).

Filtering can either be applied in the reconstruction stage, or at run time (by sampling more averages in the centre and less on the edges of k-space). This is known as

'acquisition-weighting'. Therefore, a fortuitous side effect of this weighting is that the whole of k-space need not be collected, which drastically reduces the minimum number of points to acquire, and hence the minimum acquisition time. For example, a fully encoded 16 × 16 × 8 CSI matrix with 10 averages would take 5 hours and 41 minutes to acquire with a 1 s T_R. In contrast, the same CSI matrix size with Hamming filtered acquisition scheme could be acquired in 28 minutes.

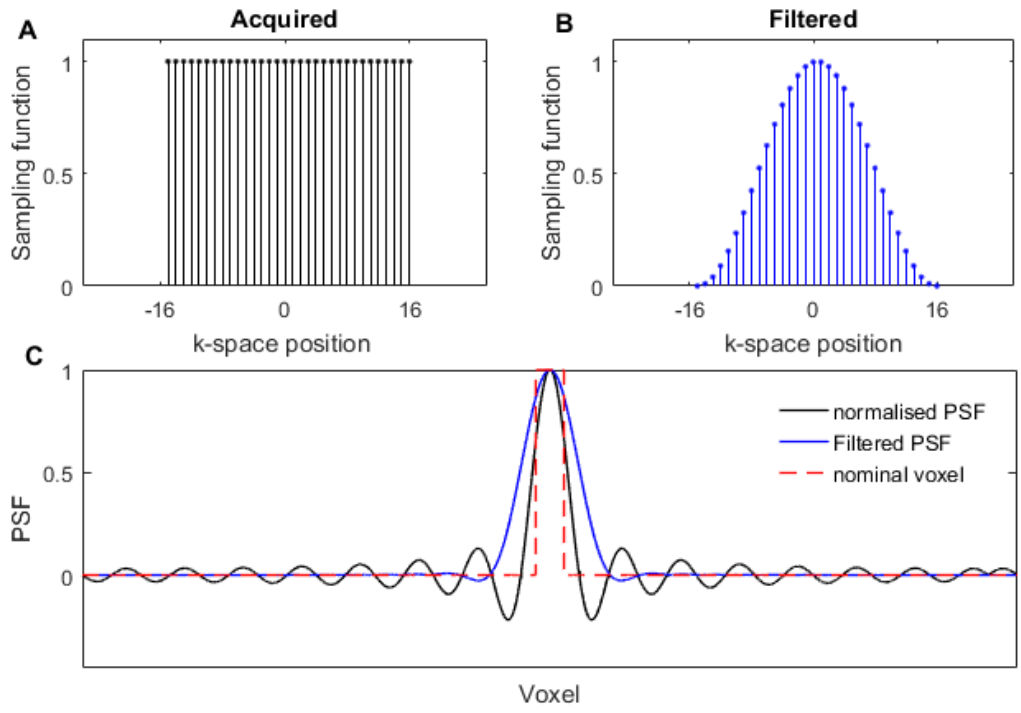


Figure 2.14 A unfiltered k-space sampling is filtered using a Hamming window function (**B**). **C** Filtering reduces the side lobes of the PSF, but at the cost of a increasing the effective size of the voxel. Both PSFs contain signal contributions from areas outside of the 'nominal voxel' given in the scan parameters.

3 ^{31}P-MRS and cardiac metabolism

This chapter provides an overview of the metabolic principles necessary to appreciate the clinical motivations that underpin this work, and the previous contributions of ^{31}P-MRS to the field. I begin by briefly describing cardiac metabolism in the healthy and failing heart, a description that is intended to equip readers new to human cardiac metabolism with the essential knowledge to navigate the succeeding chapters. More thorough information can be found in numerous reviews and textbooks on the topic.[26–29]

Over the years, phosphorus spectroscopy (^{31}P MRS) has played a unique role in aiding our study of metabolism of the heart – the second part of this chapter is a summary of the different ^{31}P MRS measurement approaches and a brief review of the existing human cardiac ^{31}P MRS literature.

3.1 Metabolism in the healthy heart

The role of the heart is to pump blood around the body. In order to do this, it needs to be supplied with energy which is done so in the form of adenosine triphosphate (ATP). ATP is known as a “high energy” phosphorous-containing metabolite because it has a high Gibbs free energy of formation which can be released in cells to power numerous biochemical processes. The heart uses more energy per gram of tissue than any other organ: around 6kg of ATP per day.[26] 60-70% of this ATP is used to fuel contractile work to circulate blood.[30,31]

The production of ATP can be broken down into 3 distinct stages: substrate utilisation, oxidative phosphorylation, and ATP transfer and utilisation (Figure 3.1).

3.1.1 Substrate utilisation

Substrate utilisation refers to importing substances into cells as a fuel source. Free fatty acids (FFAs) and glucose are taken up by cells; metabolism of either of these substances results in the formation of acetyl co-A, which enters the Krebs cycle (also known as the Tricarboxylic Acid [TCA] cycle). The Krebs cycle produces CO_2, NADH, FADH2 and ATP. In the healthy heart at rest, utilisation of FFAs accounts for 60-90% of ATP production with the remainder coming from the oxidation of pyruvate derived from the oxidation of glucose or lactate.[28] During periods of increased metabolic stress, such as increased heart rate, there is a shift towards greater utilisation of glucose.

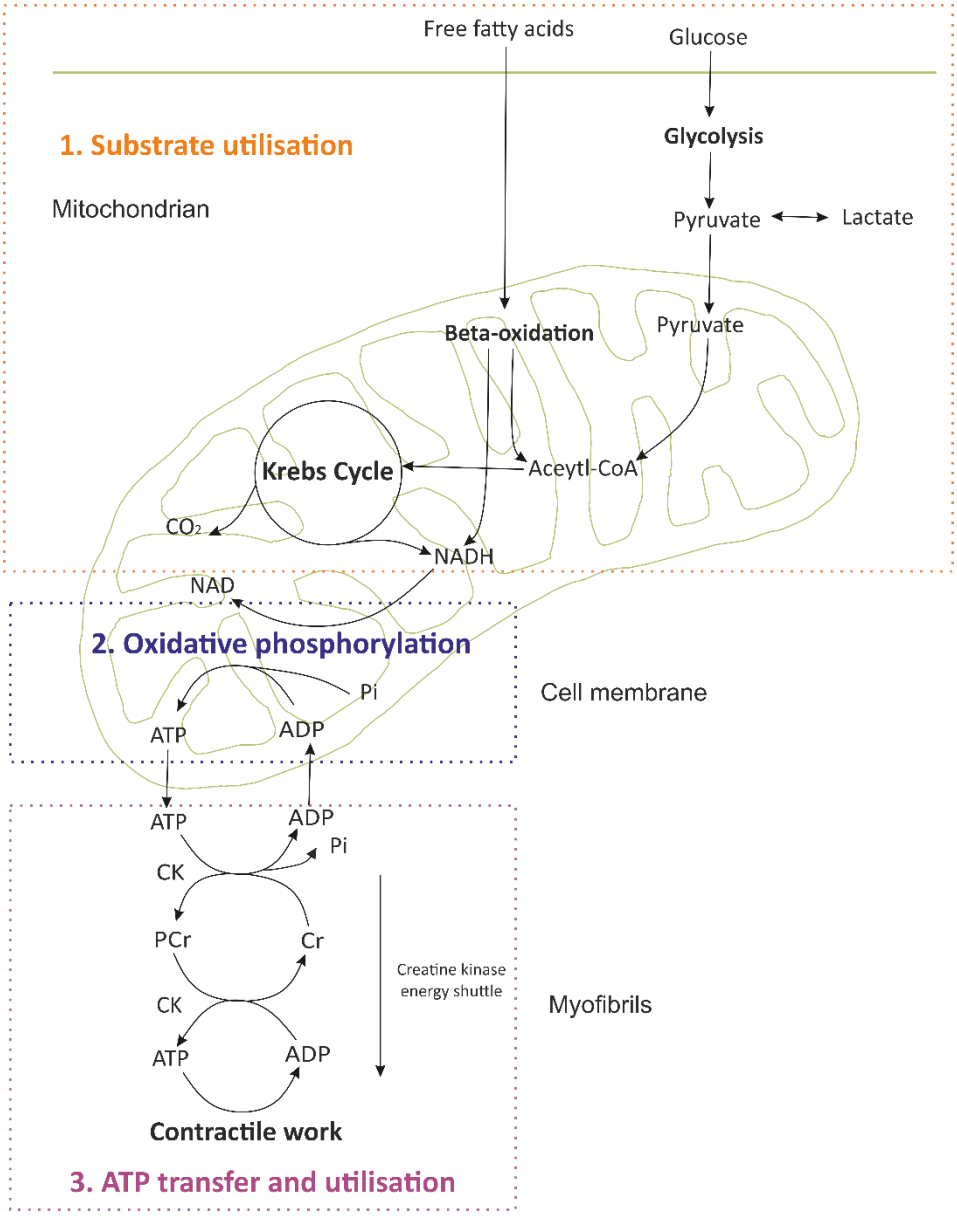


Figure 3.1. The three stages of human cardiac energy metabolism. In step 1, substrates are taken up by the cell and catabolised into acetyl-co A. Aceytl co-A enters the Krebs cycle. The second stage is oxidative phosphorylation: thegeneration of ATP. This is done via the enzyme ATP synthase at the final step in the electron transfer chain which is driven by the mitochondrial proton concentration gradient. The final step, the “CK shuttle”, transfers the ATP produced in the mitochondria to the myofibrils, where it is used to drive contractile work. Figure redrawn from Neubauer.[5]

3.1.2 Oxidative phosphorylation

It is in this step that the majority of ATP is produced. The transfer of electrons from the NADH and FADH2 produced in the Krebs cycle to oxygen creates an electrochemical gradient across the mitochondrial inner membrane. This gradient drives the mitochondrial enzyme ATP synthase to produce ATP by phosphorylating ADP.

3.1.3 ATP transfer and utilisation – the Creatine Kinase energy shuttle

Oxidative phosphorylation produces ATP in the mitochondria. In order to fuel contractile work, it needs to be transported to the myofibrils (contractile fibres). It has been claimed that passive diffusion of ATP from the mitochondria to the myofibrils is not quick enough to be the sole source of ATP transfer. Therefore, transport is facilitated by a family of enzymes, called the Creatine Kinase (CK) isozymes in a process known as the Creatine Kinase energy shuttle.[32] Briefly, the transfer of a high energy phosphate group from ATP to creatine (Cr) is catalysed by CK forming adenosine diphosphate (ADP) and phosphocreatine (PCr). As PCr is a smaller molecule than ATP, PCr is able to diffuse to the myofibrils much quicker than ATP. Once PCr has reached the myofibrils, myofibril CK catalyses the reverse reaction forming ATP in situ; the ATP is then used to drive contractile work.

Another important feature of this process is that the in-situ formation of ATP by creatine kinase is 10 times faster than by oxidative phosphorylation. This means that PCr acts as a temporal buffer to assure a consistent supply of ATP, even during bursts of increased metabolic demand, such as systole.[33]

Of course, this model is only a simplification. Recent work by Balaban's group in 2015 showed that mitochondria are also involved in the distribution of energy within the cell. The group used high-resolution electron and confocal microscopy to show that in mouse skeletal muscle, an *electrical* conduction process between mitochondria via what they termed the "mitochondrial reticulum" plays a significant role in energy distribution in the form of the mitochondrial chemical potential. ATP does not then need to be transported between the mitochondrion adjacent to a blood vessel where the fat and carbohydrate substrates are metabolised to create the mitochondrial chemical potential and the mitochondrion where the electron transport chain ATPase creates ATP because this energy is conducted electrically instead.[34] The authors concluded that the metabolic diffusion pathways, such as the CK shuttle, play a smaller, yet important, role in energy distribution becoming significant as one approaches maximum performance levels. This is an area that is still

controversial. However, what is clear is the ATP and PCr are intimately implicated in cardiac energetics.

3.2 Altered metabolism in heart failure

Simply put, heart failure (HF) is a state when the heart is no longer able to pump enough blood around the body. It is a major public health issue, with an incidence rate of 1-2% in developed countries.[35] An expensive condition to treat, HF costs the NHS approximately 1-2% of its annual budget and accounts for 5% of medical admissions.[3]

HF is not an easily-definable single entity: it is a clinical syndrome where characteristics may vary depending on age, sex, ethnicity, and HF aetiology.[36] It is a debilitating condition with patients experiencing symptoms such as breathlessness and fatigue. Sadly HF is often deadly: approximately 50% of people diagnosed with heart failure die within five years.[1,2] Heart failure therefore constitutes a significant burden, both in terms of compromising patient's quality of life, and in an economic sense.

3.2.1 Heart failure aetiology

In heart failure, the myocardium gradually changes shape and/or size (it is said to be remodelled). While remodelling is initially beneficial, in the long term it reduces the contractile function of the heart. Heart failure has multiple causes and there are many risk factors; usually, these factors cause "wear and tear" that, eventually, lead to HF.

- **Dilated cardiomyopathy (DCM).** Heart failure caused by DCM is characterised by increased ventricular volume and decreased cardiac function.[37] DCM is itself a broad categorisation – it may be idiopathic, familial/genetic, viral, and/or immune.[38]
- **Hypertrophic cardiomyopathy (HCM).** HCM is the most common inheritable cardiovascular disorder and is responsible for approximately 35% of sudden deaths in young athletes.[39,40] In late stages, HCM leads to hypertrophy (thickening) of the ventricle walls.

- **Ischaemic cardiomyopathy.** Ischemia refers to decreased blood flow. If blood flow to the heart is blocked – for example in the case of a myocardial infarction – the denial of oxygen and nutrients damages the cardiac muscle. This damaged cardiac tissue does not contract as well, which weakens the heart's ability to pump blood.
- **Type 2 diabetes mellitus (T2DM).** Patients with T2DM are twice as likely to develop heart failure.[41] Patients with T2DM often have concentric left ventricular (LV) remodelling. While the exact cause is unclear, it is thought to be linked to cardiac steatosis (abnormal retention of fat).[42] The links between type 2 diabetes and heart failure is discussed in more detail in Chapter 7.

Metabolic failure is widely understood to be the basic mechanism of these types of HF, The failing heart can be thought of as an 'engine out of fuel', an analogy that suggests that given sufficient energy, it will be able to recover and function again, albeit at a reduced capacity.[5] Being able to study cardiac metabolism is therefore beneficial; understanding metabolism's role in HF helps us to understand disease progression and could lead to new therapeutic opportunities for patients.[43–45]

HF leads to changes occurring in all three stages of cardiac ATP production (Figure 3.2). In the third stage – ATP transfer and utilisation – [ATP][i], [PCr], creatine kinase activity and ATP transfer are all reduced. ^{31}P-MRS is sensitive to changes in these parameters and is therefore a valuable tool for cardiac metabolism assessment. It is particularly valuable because of its unique ability to study metabolism non-invasively. The alternative is cardiac biopsy which is highly invasive and has significant associated morbidity making it impractical for routine examinations. Also, it requires stringent biopsy methods (freeze

[i] Square brackets indicate concentration

clamping) to avoid degradation of PCr and ATP in biopsied tissue between biopsy and analysis.[46]

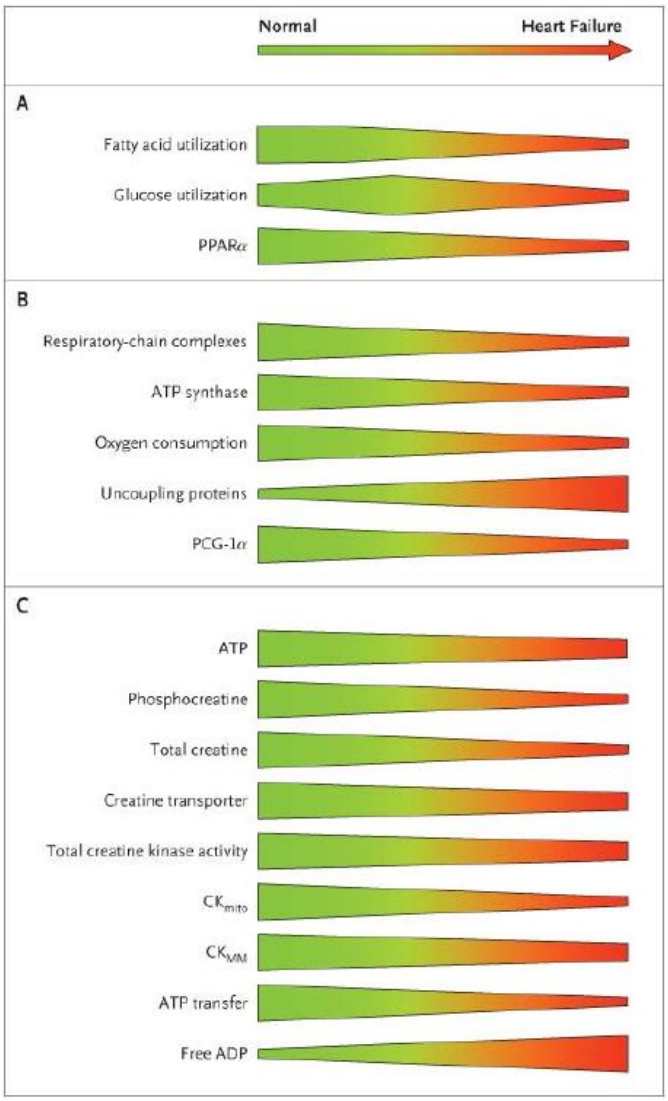


Figure 3.2 Heart failure leads to changes in all three stages of ATP production: (**A)** substrate utilisation; (**B**) oxidative phosphorylation; and (**C**) ATP transfer and utilisation. PPARα = peroxisome proliferator–activated receptor α, PCG-1α = PPARα coactivator 1α, CK_{mito} = mitochondrial creatine kinase isoenzyme, and CK_{MM} = myofibrillar creatine kinase isoenzyme. Figure reproduced with permission from Neubauer.[5]

3.3 ^{31}P-MRS of the heart

^{31}P-MRS has been used to study metabolism in both humans and other mammals. Although applied in numerous organs, this section focuses on applications in the heart. The metabolism of skeletal muscle is very similar to the myocardium's. Skeletal muscle ^{31}P-MRS is technically easier (for example, lack of motion due to the cardiac cycle). As a result, ^{31}P-MRS in skeletal muscle is often used to validate methods before they are applied in the heart. Historically, most ^{31}P MRS studies in the human heart have been performed at either 1.5 or 3 T but recent technical developments have meant that cardiac ^{31}P MRS has been able to benefit from the increased SNR at 7 T.[6,47–49]

3.3.1 The ^{31}P spectrum of the heart

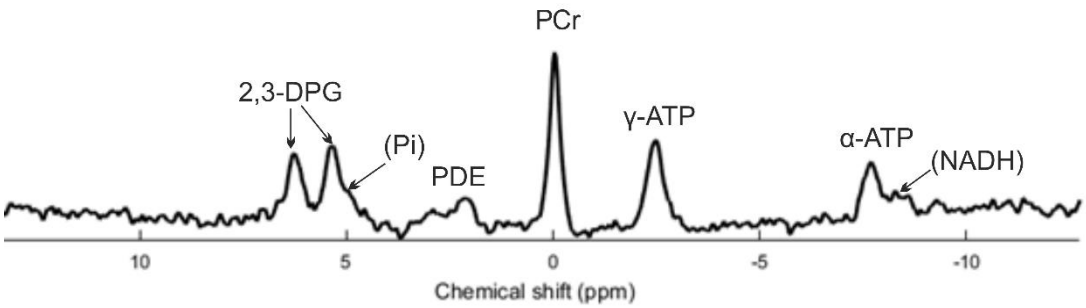
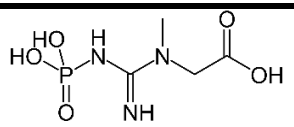
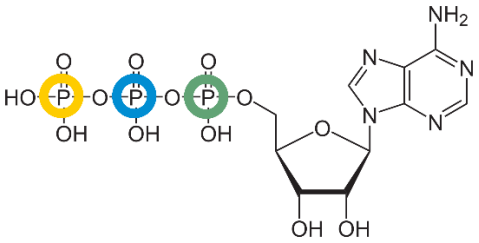
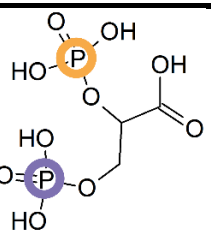
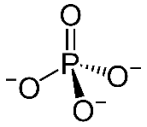


Figure 3.3 Cardiac ^{31}P-MRS spectrum from a healthy volunteer at 7 T.

Seven peaks are generally observable in the human ^{31}P-MRS spectrum of the heart (Figure 3.3). PCr is the most prominent peak. It is therefore used as an internal reference and assigned a chemical shift of 0ppm. Chemical shifts and structures of metabolites visible in the cardiac spectrum are summarised in Table 3.1.

Table 3.1 Overview of peaks typically observed in human *cardiac* ^{31}P-MRS spectra. In molecules that contain multiple ^{31}P atoms, shaded cells correspond to peaks arising from the phosphorous atom of the corresponding colour indicated in the chemical structure.

Peak name*	Chemical structure	Chemical shift (ppm)	Multiplet?	Comments
PCr		0	Singlet	Most prominent peak. Used as an internal reference.
γ-ATP		-2.48	Doublet	Splitting of ATP peaks not observed at 7 T *in vivo* due to magnetic field inhomogeneities.
α-ATP		-7.52	Doublet	Owing to large chemical shift, β–ATP is sometimes out of the excitation pulse bandwidth, so not always visible in the spectrum.
β -ATP		-16.26	Triplet	
2-DPG		6.58	Singlet	Arises as a result of contamination from the blood pool in the atria.
3-DPG		5.10	Singlet	Used in blood-correction of ^{31}P-MRS spectra.
PDE	*glycerol 3-phosphorylethanolamine*	2.67	Singlet	Broad, poorly resolved peaks.
	glycerol 3-phosphorylcholine	3.20	Singlet	
Pi		~5	Singlet	Obscured by 2,3-DPG signal, often not observable. Chemical shift is pH dependant.

*other peaks that are present in the spectrum, but typically unobservable: ADP, NADH/NAD+. ADP has a low concentration in the healthy heart, and the two peaks are obscured by the much larger γ- and α-ATP peaks. In high SNR acquisitions, NADH/NAD+ is observed as a broad peak, partially overlapped by the α-ATP.

3.3.2 Measurement parameters

^{31}P-MRS can probe cardiac metabolism by either direct measurement or calculation of various parameters. This section gives an overview of different measurement approaches by ^{31}P-MRS, and discusses the sensitivity of these parameters to the altered cardiac energetics in heart failure.

3.3.2.1 The PCr to ATP ratio

The most commonly reported parameter in cardiac ^{31}P-MRS is the ratio of PCr to ATP concentrations (PCr/ATP). In principle, PCr/ATP is a simple parameter to compute – it can either be calculated as the ratio of the phosphocreatine peak to a single ATP peak or the average of two or three of the α-, β- and γ-ATP peaks. Inclusion of all three peaks in the calculation provides the most precise results, but often experimental limitations require calculation of PCr/ATP using only a single peak. For example, α-ATP contains contributions from the broad underlying NADH/NAD+ peak and β-ATP, at 16ppm from PCr, is often outside (or at the edge of) the bandwidth of the excitation pulse at 7 T.

Long longitudinal relaxation times of ^{31}P metabolites[6,50–52] mean that ^{31}P-MRS spectra are often acquired in the "steady state" (i.e $T_R \leq 5T_1$, §2.11.2). As the T_1s of PCr and ATP peaks are different, there will be different levels of saturation in the spectrum. This means that the amplitudes of the PCr and ATP peaks need to be "saturation corrected" before they reflect the true ratio of PCr/ATP.

Additionally, a "blood correction" should be applied to cardiac PCr/ATP values. Blood in the ventricles results in contamination of "cardiac" spectra; blood contributes ATP, Pi and 2,3-DPG to the spectra but not PCr, and so blood contaminated spectra appear to have a lower PCr/ATP. As a 2,3-DPG peak is not present in a 'true' myocardial spectrum, the amplitude of the DPG peak can be used to apply a correction by subtracting 30% of the mean DPG peak amplitudes from ATP (as ATP/DPG≈ 0.3).[53]

A selection of literature cardiac PCr/ATP ratios in healthy controls is given in Table 3.2. Reassuringly, the measured PCr/ATP does not appear to vary with field strength, or with choice of localisation method (Figure 3.4). The reported standard deviations accompanying PCr/ATP as a function of field strength (Figure 3.4b) do not make it immediately clear that the SNR gains associated with higher B_0 correspond to an increase in precision of measurements, but such a simple comparison does not do higher field strengths justice. Measurements at higher field strengths often use the gain in SNR to reduce scan time, or voxel dimensions, rather than focusing on measurement precision. Furthermore, variations in measurement scatter could be due to physiological differences, even within 'normal' subjects. In order for a fair comparison, matched protocols need to be used; such direct comparative studies have indeed shown improved PCr/ATP precision as B_0 increases.[54,55]

Table 3.2 Example cardiac PCr/ATP values in healthy volunteers reported in the literature. Values have been blood and saturation corrected.

Reference	Field strength (T)	N[a]	PCr/ATP	SD
Bottomley, 1985[56]	1.5	-	1.3	0.4
Löffler 1998[57]	1.5	6	1.9	0.33
Smith, 2006[58]	1.5	14	1.9	0.3
Weiss,1990[59]	1.5	11	1.72	0.15
Beer, 2002[60]	1.5	10	1.59	0.33
Tyler, 2008[54]	1.5	10	1.76	0.38
Bashir, 2014[50]	3	15	1.94	0.15
Dass, 2015[61]	3	20	2.14	0.35
Rodgers, 2014[55]	3	9	1.7	0.5
Tyler, 2008[62,b]	3	20	2.07	0.38
Tyler, 2008[62,b]	3	20	2.14	0.46
Tyler, 2008[54]	3	10	1.62	0.22
Rodgers, 2014[55]	7	9	2.1	0.3
Stoll, 2016[49]	7	10	1.95	0.25
Valkovič, 2016[48]	7	10	2.14	0.16
		Average	**1.86**	**0.31**
Bottomley, 2016[4,c]	various	1662	1.84	0.27

[a] number of subjects – some subjects will have participated in more than one of the studies listed in this table. [b] repeats in a reproducibility study [c] review article.

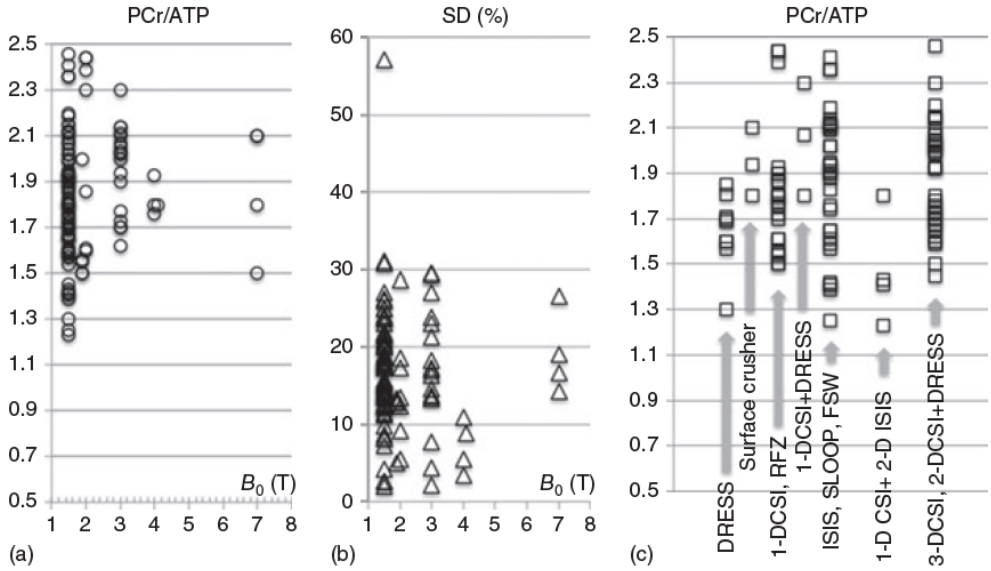


Figure 3.4 Variation in literature PCr/ATP measurements. Each data point represents a mean published value from a study in healthy controls. **A** PCr/ATP as a function of B0 (T), **B** SD of the mean PCr/ATP expressed as a percentage of the mean as a function of B0 (T), **C** PCr/ATP as a function of localisation method used. Localisation methods are discussed in section 2.8.1 Reproduced with permission from Bottomley, 2016.[4]

PCr/ATP is sensitive to certain 'normal' physiological variations and altered energetics in heart failure, summarised in Table 3.3. Reduced PCr/ATP has been shown to correlate with poorer New York Heart Association (NHYA) functional class,[63] and left ventricular ejection fraction.[64] Furthermore, reduced PCr/ATP is also a predictor of total and cardiovascular mortality in patients with DCM.[65] PCr/ATP has also been restored in DCM after treatment, supporting the heart failure 'energy starvation' hypothesis.[66–68]

Table 3.3 Sensitivity of PCr/ATP to 'normal' physiological variations and changes in disease. All measurements in humans.

	Parameter	Trend	References	Notes
'Normal' Physiological variations	Increasing cardiac workload	- or ↓	[69–75]	Up to 3x HRxBP†, no changes in PCr/ATP during exercise or pharmacologically induced stress. Reductions in PCr/ATP reported above 4x HRxBP[a].
	Increasing age	↓	[76–78]	Several studies have suggested a reduced PCr/ATP in those over 40 years old. We should be cautious about this trend – there are systemic age variations in amount of muscle in the chest wall, possibly affecting PCr/ATP if voxel contamination is present (§3.3.3).
	Cardiovascular fitness	- or ↑	[79,80]	No apparent correlation between PCr/ATP and cardiovascular fitness in the young, but reduced PCr/ATP as we age can reportedly be preserved by maintaining cardiovascular fitness.
	Obesity	↓	[81]	PCr/ATP 15% reduced in obese (BMI 39±7) compared to 'normal-weight' (BMI 22±2) controls. PCr/ATP restored following weight loss.
Disease	Ischemia	↓ ↓	[66,69,82,83]	Following myocardial infarction, decreased PCr/ATP of about 40%.
	DCM	↓	[17,63–65,84–89]	PCr/ATP reduced ~20% in DCM. Significant correlations between worse NHYA class and decreasing PCr/ATP, with PCr/ATP recovering in patients whose NHYA class improves.
	T2DM	↓	[90,91]	PCr/ATP reduced in T2DM. The causal link between T2DM and heart failure is still unclear. In addition to impaired energy metabolism, it is thought to be due to cardiac steatosis.
	HCM	↓	[61,78,87,92–95]	PCr/ATP reduced in HCM, including in patients who show no morphological changes

†HRxBP = heart rate blood pressure product, an index of cardiac workload.

3.3.2.2 Absolute quantitation

While PCr/ATP is the most commonly measured parameter in cardiac ^{31}P-MRS, it is typically used under the assumption that [ATP] remains constant until very late stage heart failure, and therefore PCr/ATP is a proxy for [PCr]. This assumption is reasonable in the healthy heart, but at high workloads [ATP] decreases and so using the PCr/ATP ratio may obscure changes in ATP concentration.[26] Furthermore, it has been shown that [ATP] starts to drop even before end-stage HF, so the PCr/ATP metric hides some early deterioration.[96]

Using ^{31}P-MRS to measure the absolute concentrations (i.e the concentrations calibrated to recognised units e.g. mol/L of mol/kg wet weight) of metabolites overcomes this limitation, but can be experimentally challenging; absolute quantitation requires a reference signal and knowledge of excitation flip angles, metabolite T_1 values and the receive sensitivity of the coil.[97]

Despite this, studies measuring absolute concentrations of human cardiac metabolites have revealed deficits in patients with cardiomyopathy, HF and myocardial infarction .[58,97–99]

3.3.2.3 Measurement of creatine kinase kinetics

^{31}P magnetisation transfer techniques can be used to calculate k_f^{CK}, the pseudo first order rate constant of the creatine kinase (CK) energy shuttle. The reversible CK catalysed reaction (§3.1.3) may be written:

$$\mathrm{Mg.ADP^{-}} + \mathrm{PCr^{2-}} + \mathrm{H^{+}} \underset{k_{-1}}{\overset{k_1}{\rightleftarrows}} \mathrm{Mg.ATP^{2-}} + \mathrm{Cr.} \qquad [3.1]$$

With the pseudo-first order forward rate constant, k_f^{CK} defined as

$$k_f^{CK} = k_1[\mathrm{Mg.ADP^{-}}][\mathrm{H^{+}}]. \qquad [3.2]$$

Myocardial k_f^{CK}s have been measured using accelerated methods such as FAST,[58,98,100] TRiST,[101,102] TwiST,[103] TDST[50] and more recently in a 3D localised method at 7 T.[47] Reduced

myocardial k_f^{CK} has been observed in patients with left ventricular hypertrophy (LVH) but not in those without HF, suggesting that reductions in k_f^{CK} might be specific to HF.[58]

Furthermore, combining measurement of k_f^{CK} with [PCr] in the same examination allows the calculation of the total forward CK flux of ATP:[98]

$$CKflux_f = k_f^{CK}[PCr]. \quad [3.3]$$

$CKflux_f$ has been shown to decline with progression to HF in nonischemic cardiomyopathy.[4,100] The reduction in $CKflux_f$ has also independently predicted cardiac events (e.g. HF hospitalization, transplantation) in HF patients occurring several years after the ^{31}P-MRS examination.[96] More recently, $CKflux_f$ measurements have provided a mechanistic link between declining CK flux, mechanical work, and cardiac events, by showing that CK flux correlated with cardiac mechanical work.[104]

3.3.2.4 Myocardial P_i and pH measurement

As the chemical shift of the P_i peak is pH dependent, ^{31}P-MRS can provide a measurement of intracellular pH.[105] The P_i terminal "OH" moieties are deprotonated or protonated depending on pH, affecting the degree to which the nucleus is shielded and thereby the metabolite chemical shift (§2.7). On the MR timescale, the exchange rate between the protonated and deprotonated forms is fast, so coalescence results in a single peak, whose position is pH dependant. The position of the PCr peak is much less pH dependant, so comparison of the positions of the Pi and PCr chemical shifts allows calculation of pH by:

$$pH = pK_a + \log\frac{(\delta - \delta_{HA})}{(\delta_A - \delta)}. \quad [3.4]$$

Where pK_a = 6.75, the dissociation constant of P_i, δ_{HA} = 3.27 ppm (the chemical shift of the mono-protonated form of P_i), δ_A = 5.63 ppm (the chemical shift of the fully de-protonated P_i). While easily resolvable in skeletal muscle, P_i in the heart has previously proven hard to

observe – the 2,3-DPG peaks in cardiac spectra that arise from blood in the ventricles overlap the Pi peak, obscuring it. However, the improved spectral resolution that comes at higher field strengths has recently enabled robust detection of Pi and therefore robust pH measurement in the myocardium.[106]

When combined with measurements of the PCr, ATP and free creatine (from ^{1}H-MRS[107]) concentrations, the Gibbs free energy for the hydrolysis of ATP (i.e. the maximum amount of chemical energy available to drive contraction work in the myofibrils) can be calculated.[108]

3.3.2.5 Combining measurements for more sensitive markers

In recent years, machine learning techniques using multi-layer neural networks have emerged as methods to identify and classify a vast array of multi-parametric data in many applications. In 2019, Solaiyappan *et al.* used such an approach to predict specific human heart disease and clinical severity.[109] Classifying [PCr], [ATP], k_f and $CKflux_f$ from 178 subjects provided a more specific marker than any single ^{31}P-MRS parameter. This could be a step closer to ^{31}P-MRS methods being able to classify HF severity with clinically relevant accuracy.

3.3.3 Causes of signal contamination

The heart lies close to a number of other tissues that have similar, but different, ^{31}P spectra. Therefore, any imperfections in the localisation technique, or partial volume effects from other tissues in the voxel of interest may lead to acquisition of a spectrum that inadvertently has contributions from more than one tissue type, often termed “signal contamination”.

As mentioned in §3.3.2.1, blood in the ventricles can contaminate “cardiac” spectra: blood contributes ATP, Pi and 2,3-DPG to the spectra. So PCr/ATP ratios should be “blood corrected” as described in §4.4.2.

The chest wall contains skeletal muscle, the ^{31}P spectrum of which contains PCr, ATP, Pi and PDE peaks. PCr/ATP in skeletal muscle is larger – about 3.5-4.5, compared to approximately 2 in the heart.[110] Contamination from skeletal muscle will therefore artificially raise measured

PCr/ATP and, as there aren't any differentiating metabolites, low levels of contamination can be hard to spot. Occasionally, contamination can be seen as 'splitting' of the PCr peak, resulting from different resonant frequencies that are the result of B_0 inhomogeneity between the chest wall and the heart. Furthermore, the chest wall is closer to the receive coil than the heart, resulting in a greater B_1^- sensitivity to signal originating from chest-wall skeletal muscle compared to myocardial tissue. Skeletal muscle contamination can be minimised by using RF saturation bands over the chest wall to reduce contamination[111] or by the use of a "crusher coil".[112] Different coils will have a different balance of B_1^- sensitivity between skeletal muscle close to the surface and the heart – this may account for some of the differences in PCr/ATP measurements in healthy subjects between sites.

Cardiac spectra can also be vulnerable to contamination from liver tissue, especially when volume excitation and reception are being used. The liver contributes ATP to a contaminated cardiac spectrum, but not PCr. Liver contamination will bias PCr/ATP measurements to be smaller than their true value.

3.4 Summary

Evidently cardiac ^{31}P-MRS is a valuable tool for studying cardiac metabolism. Altered energetics is widely believed to be a mechanism of HF – ^{31}P-MRS methods are able to detect such metabolic changes, making it a sensitive measure for the presence and severity of HF (Table 3.4**Error! Reference source not found.**). However, at the moment ^{31}P MRS is limited by the SNR of the acquisition, leading to long acquisition times and requiring large study cohorts to be sufficiently powered. Recently, however, whole-body 7 T MRI scanners have already brought a step change in the available SNR, increasing the precision of ^{31}P-MRS measurements.[6]

Table 3.4 Summary of ^{31}P-MRS findings in heart failure

	DCM	HCM	T2DM	MI	Reflects
PCr/ATP	↓	↓	↓	↓	Indicator of cardiac energy reserve
k_f^{CK}	↓	↓	↓	-	Forward rate constant in CK energy shuttle
CK_{flux}		↓		↓	Provides information about energy turnover
Pi		↑	↑		Net Pi when ATP hydrolysis exceeds synthesis
pH					If pH drops, is the result of lactic acid being produced by anaerobic respiration

↑Increases versus normal, ↓ decreases versus normal. Empty cells represent situations where no published data yet exist for newer methods.

4 Data acquisition

This chapter gives an overview of the general methods used to acquire cardiac ^{31}P-MRS data at 7 T at the Oxford centre for Clinical Magnetic Resonance (OCMR). I describe the hardware used for the research in this thesis. I also present an assessment of which of our surface coils delivers the highest B_1^+ in the myocardium. This is important as the refocusing pulses used in Chapter 8 are optimised to these values. Additionally, the base ultra-short-echo chemical shift imaging (UTE-CSI) spectroscopy sequence used to acquire ^{31}P spectra is described, along with the standard scanning protocol and post processing methods.

4.1 Hardware

4.1.1 MR Scanner

All the ^{31}P-MRS data in this thesis was acquired on a Magnetom 7 T MRI scanner (Siemens, Germany). It is an experimental-only whole-body MR scanner, with an actively shielded magnet. There is no ^{1}H 'body coil', meaning that ^{1}H images used in localisation or shimming needed to be acquired with ^{1}H surface coils.

4.1.2 RF Coils

Each RF coil relevant to my thesis is described below. The names given here are used throughout the remainder of the thesis to describe these coils.

^{31}P Surface coils

16 Channel Array Coil

This is a 16 element ^{31}P receive array coil (Rapid Biomedical, Rimpar, Germany), consisting of a single rectangular 28 × 27cm^2 transmit loop and a 4 × 4 matrix of sixteen 5.5cm-diameter

circular flexible receive loops.[113] This coil was used for data collection in Chapters 5-7. See Figure 1A.

Quadrature Coil

This coil was designed and built in-house. It contains a circular 9cm ^{1}H transceiver loop. There are two ^{31}P overlapping 15cm transceiver loops, which are driven in quadrature (i.e. with a 90^{0} phase offset).[48] See Figure 1B.

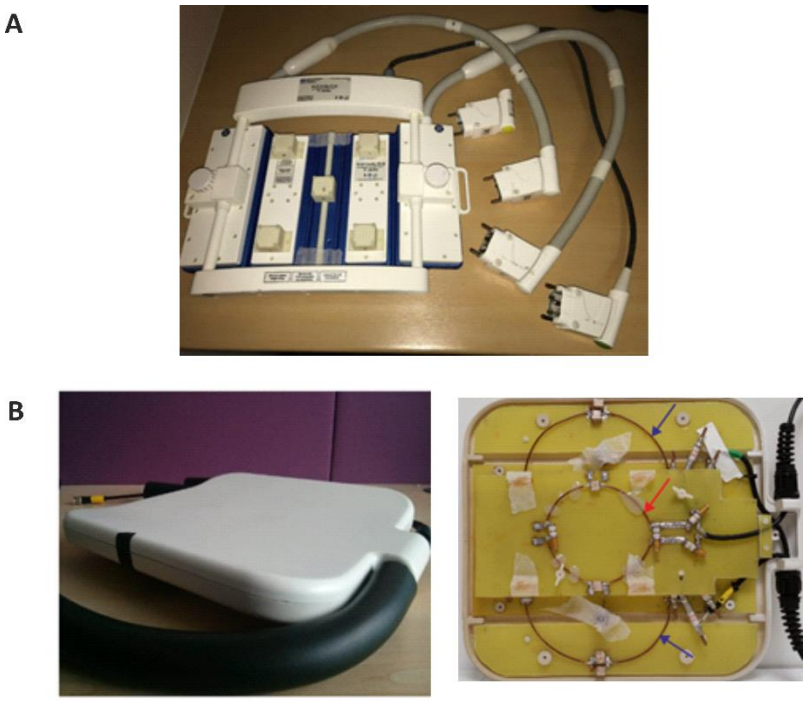


Figure 4.1 Photographs of the 7 T ^{31}P-MRS surface coils used in this thesis. **A** the '16-channel array' **B** the 'Quad coil'

^{1}H Loop

Since the 7 T has no built-in body coil, all ^{1}H measurements for chapters 5-7, were performed using a 10cm circular ^{1}H transceive surface coil. This coil was manufactured by Rapid Biomedical (Germany) and supplied with the scanner. The Quadrature ^{31}P coil has its own ^{1}H transceive loop with 9 cm diameter.

4.1.3 Performance comparison

Before I started this project, the transmit and receive performance of the 7 T ^{31}P surface coils had already been characterised in a point-source phantom.[114] The phantom contained a $2cm^{3}$

cube of $KH_2PO_{4(aq)}$, submerged in a tank of saline. Two screws at the top of the phantom drive threaded rods and allow the distance between the phosphate cube and the coil to be adjusted, permitting the performance of the coil to be characterised as a function of depth. Briefly, by varying the transmit voltage of a rectangular pulse of duration T_d, the corresponding signal amplitudes can be fitted to a sinusoidal function. The first null point in the curve corresponds to a flip angle of 180º. This can be used to compute the "reference voltage" (V_{ref}) used on Siemens systems to compute all other RF pulse voltages in a protocol. V_{ref} is defined as the voltage that produces a 180° nutation in 1ms. In terms of B_1^+, a 1ms 180° amounts to a nutation frequency of 500 whole rotations per second, i.e. γB1+ = 500 Hz at V_{ref}. The maximum B1+ for the coil is hence given by:

$$B_{1\ max}^{+} = \frac{500}{\gamma}\frac{V_{max}}{V_{ref}}. \qquad [4.1]$$

Being composed of smaller, multiple receive elements, the 16 channel array offers the best SNR of the two ^{31}P coils. In lean individuals, the depth of the heart is about 8-10cm from the anterior chest wall; the highest transmit B_1^+ that can be achieved at this distance is approximately 16μT, using the Quadrature Coil. It is important to know the characteristics of an RF coil, as it means that we can choose the most suitable coil for a given experiment. The 16-channel array was used preferentially except where B_{1+} > 10μT was needed.

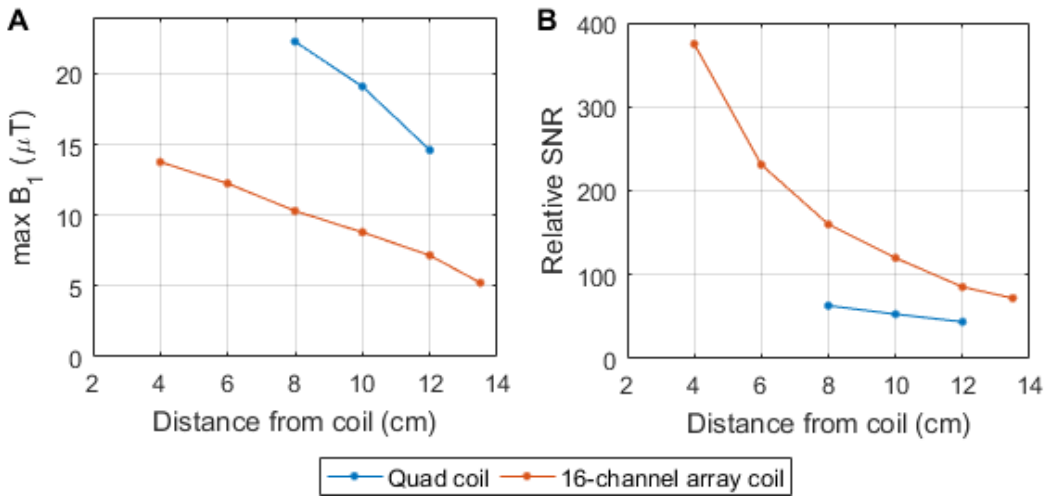


Figure 4.2 A Transmit (B_1^+) performance of the 7 T ^{31}P surface coils at maximum transmit voltage as a function of distance from the coil and receive (SNR).

4.2 Determining the *in vivo* B_1^+ performance of the Quad Coil

The development of a multi spin-echo sequence in Chapter 8, required high B_1^+ in order for the refocusing pulses to achieve a flip angle of 180^0, while maintaining a reasonable pulse length. I therefore planned to use the quadrature coil for these acquisitions. I validated that the *in vivo* B_1^+ performance of the coil was similar to phantom measurements using a Bloch-Siegert ^{31}P cardiac B_1 mapping method, designed and implemented in Oxford by Clarke *et al.*[115] The Bloch Siegert approach[116] measures B_1^+ by insertion of an additional RF-pulse (the "Bloch-Siegert pulse") between excitation and the readout in a sequence, altering the phases of the peaks in the spectrum. The Bloch-Siegert pulse is centred off resonance to minimise the effects of direct excitation, and to give a linear relationship between the phase of the peak and the B_1^+, encoding the B_1^+ measurement in the phase of the measured signal.[117]

The ^{31}P cardiac Bloch Siegert B_1^+ mapping developed by Clarke *et al* uses two measurements, with the Bloch-Siegert pulse (an optimised fermi pulse) centred at +2000Hz and -2000Hz respectively (relative to PCr).

I scanned three healthy volunteers (2M/1F, age 24-25, BMI 23±1.5 kg/m^2) in accordance with local ethical guidelines. Subjects were scanned head first supine. Localisation was performed

as described in §4.2.1. Acquisition parameters were: 240 × 240 × 200 mm^3 field of view, 16 × 8 × 8 resolution (16 perpendicular to the coil), acquisition weighting (§4.2.3) with 16 averages at k = 0, 6 kHz bandwidth and 2048 spectral samples. Total scan time was 2 × 21 min. B_1^+ maps of the heart are given in Figure 2. They confirm that a B_1^+ of 16μT is consistently achieved in the mid ventricular septum.

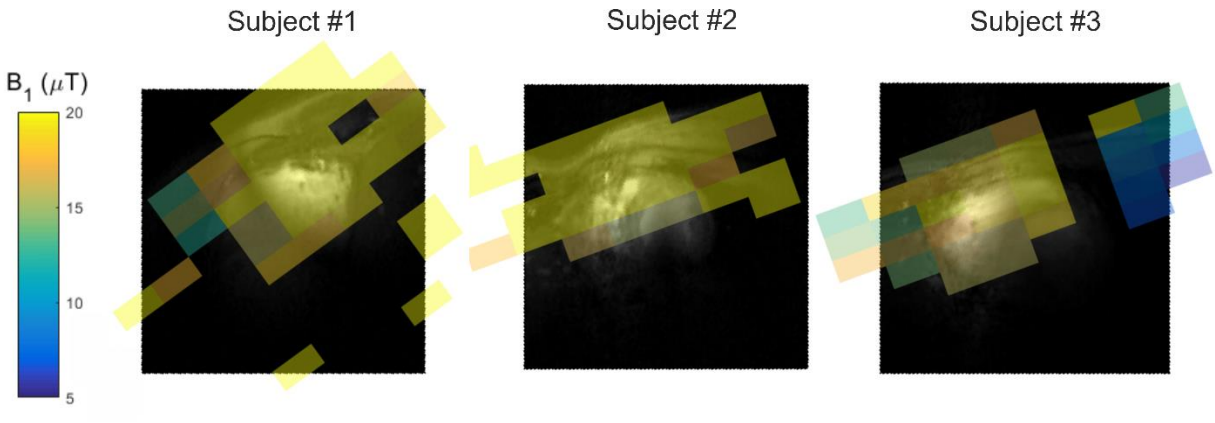


Figure 4.3 Bloch Siegert B_1 maps in the short axis view of the heart using the Quad coil at 7 T. The colour overlay is transparent in voxels below a minimum SNR threshold for robust B_1+ mapping as described in Clarke *et al*.[118]

4.3 Data acquisition

To reduce repetition in following chapters, this section describes the typical "base" cardiac 7 T ^{31}P UTE-CSI acquisition used in OCMR. Later references to the methodology described in this section will be described as a 'standard ^{31}P acquisition'.

4.3.1 ^{1}H localisation

^{1}H images for localisation were acquired prior to the main ^{31}P scan. The 10cm ^{1}H loop (§4.1.2) was used to acquire 2 chamber, 4 chamber and mid-short-axis (SA) ^{1}H fast low angle shot (FLASH) stacks of localiser cine images during breath hold. Cine scans were used because the continual pulses suppress intensity in the chest wall, minimising motion artefacts over the heart. Cardiac gating was performed using a pulse oximeter. After localisation, the patient table was removed from the magnet bore and the ^{1}H loop coil was replaced with a 16 channel array ^{31}P coil in the same position above the mid-ventricular septum. The subject lay still on

the patient table during the coil swap, to ensure identical position in the magnet for both scans. The bed is returned to the “0 mm” position without further laser position adjustment. The Siemens “table supervision” is disabled in the scanner software so that the localisers remain visible in the slice planning GUI in spite of the table move.

4.3.2 Calibration scans

The 16 channel array has 5 spherical fiducials mounted on the housing – one in the centre, and one in each corner. The fiducials contain phenylphosphonic acid (PPA) dissolved in either ethanol (for the central fiducial) or acetone (corner fiducials), chosen to shift the frequency of the centre fiducial slightly to make it distinct from the others. Transmit efficiency was calculated on a per-subject basis by using a series of inversion-recovery free induction decay scans (“IR FIDs”) to acquire signal from the central fiducial. This was processed in MATLAB. The coil position was determined from three orthogonal single-channel ^{31}P FLASH images which localise five PPA fiducials (including the centre fiducial used to compute the B_1 calibration).

4.3.3 Base spectroscopy sequence

The standard spectroscopy sequence used to acquire data in Chapters 5-7 was an acquisition weighted 3D ultra-short echo CSI sequence,[119] that had previously been applied in the human heart at 7 T.[6,49] UTE-CSI increases SNR above a standard CSI acquisition by minimising the echo time at each point in k-space, reducing the amount of signal lost to T_2^* decay. The minimum TE was set at 100μs to allow the coil to switch from transmit to receive mode (“ring down time”), the maximum TE was 200μs (used at the edge of k-space where the gradients were the longest). The TR was set to 1 second.

The standard acquisition matrix size was 16x16x8, with a nominal voxel size of 15x15x25 mm^3. 10 averages were acquired in the centre of k-space, leading to an acquisition time of 28 minutes.

RF excitation was performed using a shaped pulse that comprises a 0.5ms hard pulse, preceded by a numerically optimised 1.9ms part that improves homogeneity of excitation. It excites an approximately 2kHz bandwidth. Excitation was placed at +266Hz relative to PCr so as to cover metabolites from 2,3-DPG to γ-ATP. (In the scanner adjustments dialog this means 266Hz to the RIGHT of the PCr resonance.) The excitation was set to 400V peak amplitude (i.e. 3.2kW), giving a flip angle of approximately 30^0 in the interventricular septum.

A 25mm thick, B_1-insensitive train to obliterate signal (BISTRO), saturation band was placed in the anterior chest wall to suppress signal from skeletal muscle.[111] BISTRO consists of amplitude and frequency modulated pulses interleaved with spoiler gradients. It was developed for band-selective signal removal in applications where transmitted RF is inhomogeneous, such as when using a surface coil. The voltage of the saturation pulses was set to the maximum value allowed to comply with the legal specific absorption rate (SAR) limits in each subject, typically ~200V.

The CSI acquisition was not gated. This was a conscious decision: given the comparatively large voxel dimensions used for cardiac ^{31}P-MRS, a voxel containing inter-ventricular septum will continue to contain strong contributions from this tissue throughout the cardiac cycle. Gating is not without cost, because it introduces variations in TR between scans, and between subjects, which can affect the reproducibility of measurements due to varying T_1 relaxation.

In this standard acquisition, the CSI grid was positioned in the short axis view of the heart, such that the longest voxel dimension was aligned with the intraventricular septum and the in-plane voxel matrix was parallel to the chest wall. This reduced the PSF in the direction of the chest wall, minimising contamination from skeletal muscle.

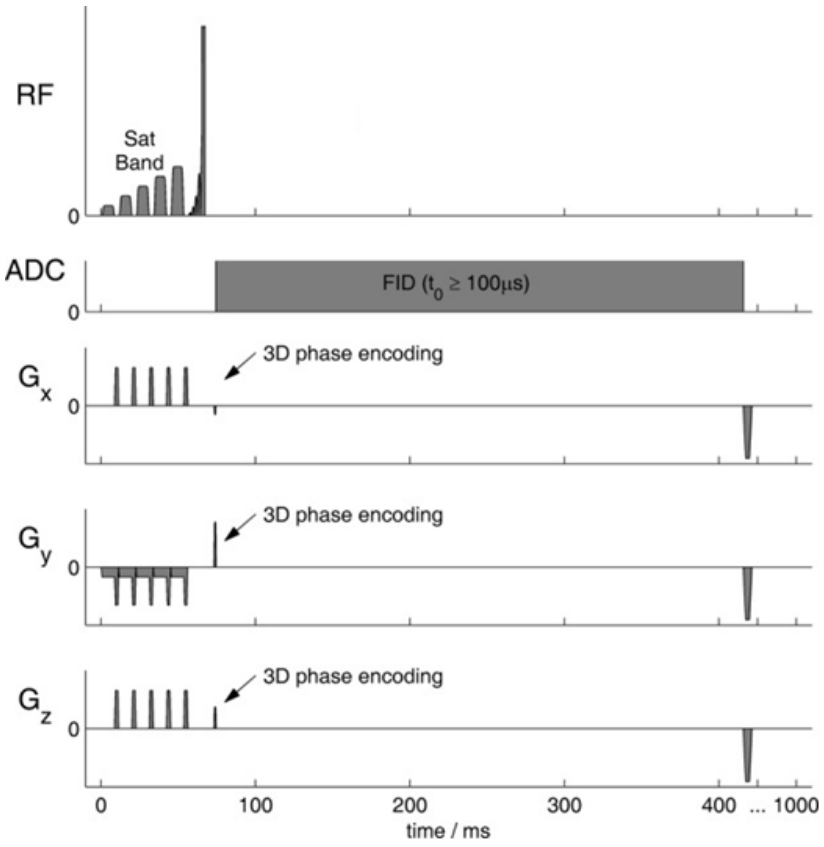


Figure 4.4 *Plot of a single TR in the UTE-CSI sequence. Figure adapted from reference* [6]

4.4 Data analysis

k-space data was Fourier transformed on the scanner to give a spatially localised CSI grid with a FID corresponding to signal from each voxel. This data was then exported in the DICOM format. Both the ^{31}P coils that were used in this thesis have multiple receive elements and so data from the individual coils was combined using the WSVD coil combination method.[120] DICOM data was then loaded into the Oxford Spectroscopy Analysis toolbox (OXSA),[121] a Matlab implementation of the AMARES fitting alogorithm.[122] AMARES is a time domain fitting algorithm which incorporates prior knowledge. This approach has improved accuracy and precision over the simpler approach of quantifying spectra in the frquency domain via peak integration.[123]

The prior knowledge used to fit cardiac spectra in this thesis (Table 1) specified 11 Lorentzian peaks with fixed amplitude ratios and literature values for the scalar couplings for the multiplets.

Table 4.1 7 T cardiac ^{31}P-MRS prior knowledge. Bounds are indicated by 'lower bound':'upper bound'. All peaks were fitted to a Lorentzian line shape.

Peak	Initial values		Bounds				Multiplet relations	
	Chemical shift (ppm)	Linewidth (Hz)	Chemical shift (ppm)	Linewidth (Hz)	Amplitude	Phase (deg.)	Relative chemical shift (ppm)	Relative amplitude
PCr*	0	10	-∞:∞	0:∞	0:∞	0:360		
α-ATP 1	-7.88	10	-∞:∞	0:∞	0:∞	0:360	-0.133	1
α-ATP 2							+0.133	1
β-ATP 1	-16.74	10	-∞:∞	0:∞	0:∞	0:360	-0.124	1
β-ATP 2							0	2
β-ATP 3							+0.124	1
γ-ATP 1	-2.82	10	-∞:∞	0:∞	0:∞	0:360	-0.124	1
γ-ATP 2							+0.124	1
2,3-DPG1	5.1	20	3.5:7.5	20:100	0:∞	0:360		1
2,3-DPG2	6.58	20	4.0:8.0	20:100	0:∞	0:360		1
PDE	2.69	20	-∞:∞	20:100	0:∞	0:360		

*PCr was defined in the prior knowledge as the reference peak

4.4.1 Saturation correction

Because the T_1s of PCr and ATP are different, and the UTE-CSI sequence was not run fully relaxed (i.e. $T_R < 5T_1$), PCr/ATP ratios needed to be corrected for partial saturation effects. Saturation correction necessitates knowledge of TR, metabolite T_1s and the achieved excitation flip angle. The sequence TR is obtained trivially from the scan's DICOM header; determining T_1 and flip angles are more involved.

Metabolite T_1s have been measured in healthy volunteers at 7 T[6] and were assumed to be the same in every subject. Of course, physiological variations will mean that this assumption is not strictly true – ideally T_1s would be measured on a per-subject basis, but time constraints make this impractical. This approach of fixed T_1 values is in some respects a limitation: while metabolite T_1 measurements are not available in disease, CK exchange rates are known to be different.[98] The apparent T_1 for exchanging metabolites such as PCr and ATP is a function of the chemical exchange rates and the intrinsic T_1 values, so it is therefore conceivable that ^{31}P T_1s (i.e. apparent T_1 values) are also altered in disease; perhaps if not possible to measure individually for each subject, T_1s in different diseased cohorts should be established.

Flip angles can be measured directly using a B_1^+ mapping method.[118,124,125] Again, owing to the limited time available during an *in vivo* human scan, this is not usually feasible to do on a per-subject basis in addition to the standard CSI measurement. We estimate flip angles by scaling a computed estimate of the coil's transmit field, calculated from the inversion recovery FID data (§4.2.2)

4.4.2 Blood correction

Blood in the ventricles results in contamination of "cardiac" spectra. Blood contributes ATP, Pi and 2,3-DPG to the spectra, and so blood contaminated spectra appear to have a lower PCr/ATP. This can be corrected by noting that ATP/DPG≈ 0.3.[53] 30% of the mean amplitude of the two 2,3-DPG peaks is subtracted from each ATP integral in the accepted method for correcting this effect.

4.4.3 Reporting PCr/ATP

In scans where PCr/ATP is reported in this thesis, unless otherwise specified I have chosen to give the ratio of PCr to γ-ATP, rather than the average of all three ATP peaks. This is because β-ATP is outside the bandwidth that is reliably excited by the shaped excitation pulse used in our standard UTE-CSI protocol and α-ATP contains additional underlying contributions from NADH/NAD+.

5 Reproducibility of the existing cardiac 7 T ^{31}P MRS protocol

Prior to this work in this chapter, an increase in SNR of 2.8× at 7 T vs 3 T of ^{31}P spectra in the human heart was demonstrated by Rodgers *et al*.[6] This established 7 T protocol, described in Chapter 4, was designed to record high quality spectra in 28 minutes, a scan time that is tolerable to the majority of patients.

Stoll *et al* used this protocol to compare PCr/ATP measurements in DCM patients at 7 T vs 3 T – they observed the expected gain in SNR from 3 T to 7 T, which consequently improved the metabolite quantification accordingly.[49] However, the inter-subject SD of measured PCr/ATP was only reduced slightly (PCr/ATP mean ± standard deviation, 1.48 ± 0.44 at 3 T vs 1.54 ± 0.39 at 7 T) by moving to the higher field strength. The authors hypothesised that this was because ^{31}P-MRS at 7 T was able to resolve the true biological variability in PCr/ATP in the DCM patient cohort. To test this, I performed the reproducibility study presented in this chapter. If the 7 T ^{31}P reproducibility is indeed improved over that previously measured at 3 T,[62] the scatter observed in the DCM patients is likely to be true biological variability. This would be an important step towards per-patient assessment of cardiac energetics which has been a key, but elusive, goal of ^{31}P-MRS research for decades.

In this chapter, I assess the reproducibility of the 7 T protocol in 10 healthy volunteers. I use this to illustrate the impact of the technical improvements gained by moving to 7 T by comparing the sample sizes and approximate scan costs of studies using the standard 3 T and 7 T protocols. Work from this chapter contributed to the publication:

Ellis, J., et al. 2019. Reproducibility of human cardiac phosphorus MRS (^{31}P-MRS) at 7 T. ***NMR Biomed****. 32, e4095; doi: 10.1002/nbm.4095.*

5.1 Experimental

Ten healthy volunteers (3 female, age = 29±6 years, BMI = 23±4 kg/m^2) were recruited according to local ethics regulations. Volunteers were scanned twice: during each scan, the standard cardiac ^{31}P-MRS 7 T protocol described in Chapter 4 was performed, using the manufacturer's default shim settings.

5.1.1 Data acquisition

Data acquisition followed the protocol detailed in section 4.2. In each session, I acquired a single ^{31}P dataset in 28 minutes with the standard 3D UTE-CSI sequence (§4.2.3). The CSI matrix was fixed at the point of acquisition, and not shifted in post-processing.

The established 28 minute scan tested in this chapter has the following parameters: matrix size 16×16×8; nominal voxel size 15×15×25mm^3; acquisition weighting with 10 averages at k=0; repetition time 1 s. The excitation was set to 400V peak amplitude (i.e. 3.2kW), giving a flip angle of approximately 30^0 in the interventricular septum. Subjects were then removed from the magnet – this constituted 'session 1'. After a short (~5min) break, I repeated localisation and acquired an identical 28-minute 3D UTE-CSI sequence in 'session 2'. These datasets are labelled "X" and "Y" for future reference (see Fig. 5.1 for detailed description).

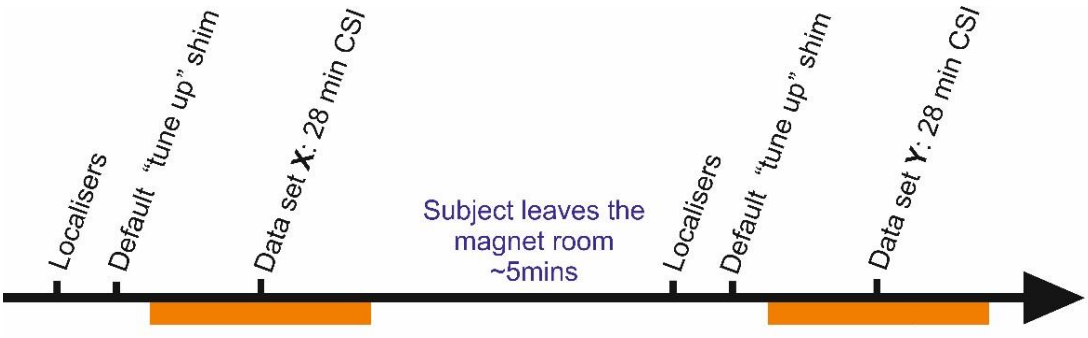


Figure 5.1 Study protocol.

5.1.2 Data analysis

I chose four voxels in the mid-interventricular septum for analysis: the midseptal, anteroseptal, anterior and posterior voxels (Figure 5.2). These were assigned anatomically; the midseptal voxel was two voxels posterior to the chest wall. Data from these voxels were fitted using the Oxford Spectroscopy Analysis (OXSA) toolbox's implementation of AMARES.[121,122] Prior knowledge specified 11 Lorentzian peaks, fixed amplitude ratios, and literature values for the scalar couplings for the multiplets. Blood contamination and partial saturation was corrected using T_1 values from the literature.[6,62] All scans were included in the analysis. Cramér-Rao lower bounds (CRLBs) were used to express the uncertainty in metabolite concentrations.[126] I calculated reproducibility statistics of both the four voxels in the mid-interventricular septum, as well as the statistics for their spectral sum.

5.1.3 Assessment of reproducibility

Inter-session variability was assessed through the mean and difference between PCr/ATP ratios for each subject.

Inter-subject variability was assessed by the mean and standard deviation of PCr/ATP ratios within the same datasets across all subjects.

The coefficient of repeatability (CR) was calculated from standard deviation of the *signed* differences in PCr/ATP between two scans for each subject according to:

$$CR = SD_{intrasubject} \times 1.96. \qquad [1]$$

A *lower* CR reflects a better method. A two-tailed Mann-Whitney U (non-parametric) test was used to compare repeated measurements. Variances were compared using a Brown-Forsythe test.[127] The coefficient of variation (CV), defined as the sample standard deviation divided by the mean, is also reported.

$$CV = SD \,/\, mean. \qquad [2]$$

I also compared our repeated PCr/ATP measurements in healthy volunteers to those collected from 25 patients with dilated cardiomyopathy (DCM) in Stoll *et al*'s study using the same 28-minute protocol, coils, and scanner.[49]

5.2 Results

Typical spectra from across the heart are shown in Figure 5.2. There is lower signal in the posterior voxels, owing to the use of a surface coil.

5.2.1 Analysis methods

Figure 3 gives reproducibility statistics for single voxels, and combinations of voxels summed prior to fitting. The midseptal voxel gives the most reproducible PCr/ATP values, shown by it having the lowest coefficient of reproducibility. The voxels closest to the chest wall (the anterior and anteroseptal voxels) have the highest PCr SNR, and the lowest PCr/ATP CRLB indicating a more precise quantification. However, the reproducibility in these voxels is lower than in the midseptal voxel. The posterior voxel has both a lower quantification precision (higher CRLBs) and worse reproducibility than the mid-septal voxel. Summing spectra from the midseptal voxel with anteroseptal and anterior voxels before fitting leads to a reduction in PCr/ATP CRLB but comes at a cost to the reproducibility of the measurement. All subsequent analyses therefore calculated PCr/ATP from the midseptal voxel, not the summed voxels.

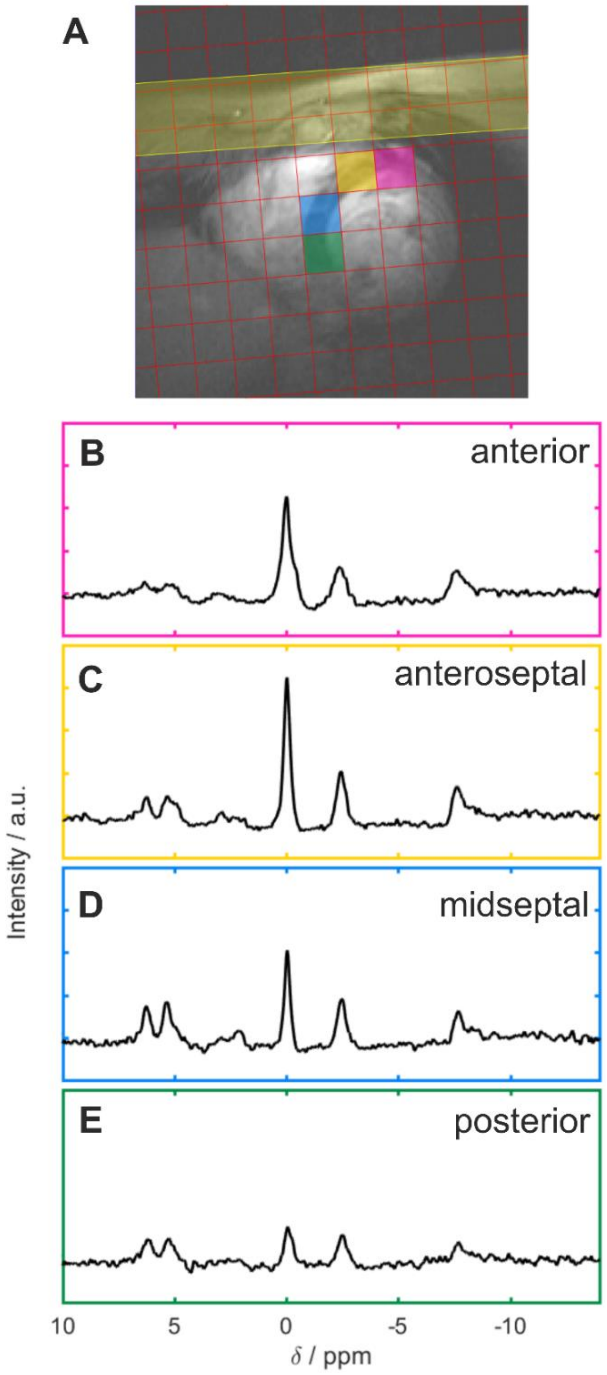
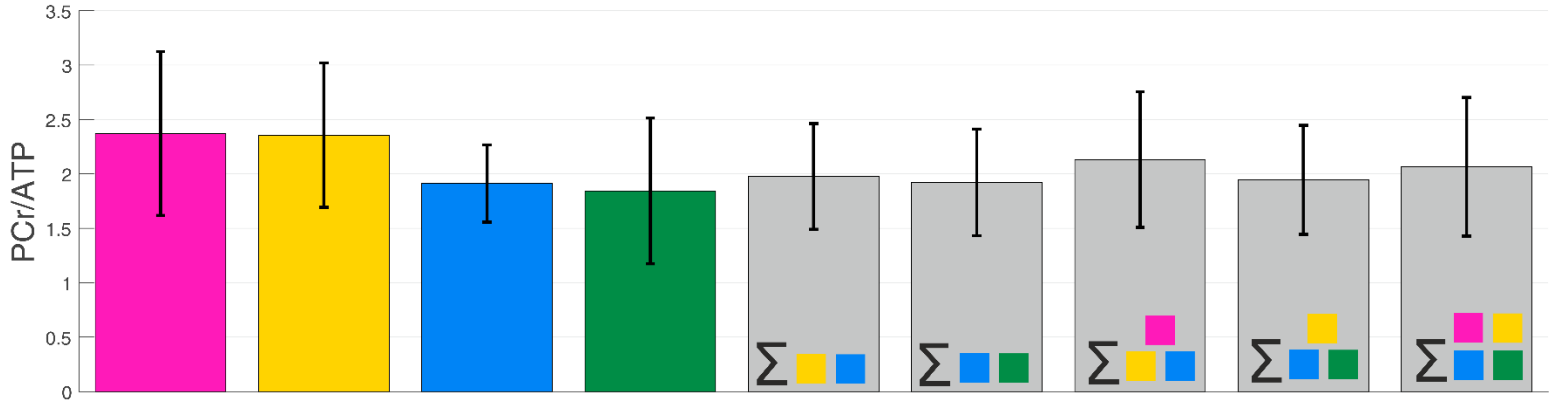


Figure 5.2 **A** Position of the CSI matrix showing the rotation of the CSI grid in the short axis view of the heart. Yellow band marks the location of the BISTRO saturation band intended to supress signal form skeletal muscle. **B-E** Spectra from the corresponding coloured voxel marked on the localiser images



	Anterior voxel	Anteroseptal voxel	Midseptal voxel	Posterior voxel	Anteroseptal + Midseptal	Midseptal + Posterior	Anterior + Anteroseptal + Midseptal	Anteroseptal + Midseptal + Posterior	All 4 voxels
PCr/ATP	2.37	2.35	1.91	1.84	1.98	1.92	2.13	1.95	2.06
PCr SNR	39	41	28	21	50	34	74	55	77
CRLB	9.1%	8.1%	9.9%	15%	8.8%	13%	8.6%	10%	9.8%
Coefficient of Variation	32%	28%	18%	37%	25%	26%	23%	26%	31%
Coefficient of Reproducibility	2.0	1.2	0.49	2.3	1.23	1.42	1.19	1.47	1.19

Figure 5.3 Variation in PCr/ATP value measured at 4 voxel locations and combinations of spectral sums of these voxels. The table below provide the PCr SNR, the Cramér Rao Lower Bound on PCr (CRLB), the coefficient of variation (CV = inter-subject SD / mean) and the coefficient of reproducibility (CR = 1.96 × inter-scan SD) of the measured PCr/ATP.

5.2.2 Assessment of reproducibility

There were no significant differences in PCr/ATP (1.86±0.32 vs 1.96±0.39, *P* = 0.79) between repeated measurements in the same subjects (Fig. 4). The mean PCr/ATP measured across all scans was 1.91±0.36, giving a CV of 18%. The intra-subject variability was 0.21± 0.16, giving a CR of 0.49. These values are shown on Bland-Altman plots in Figure 5.4.

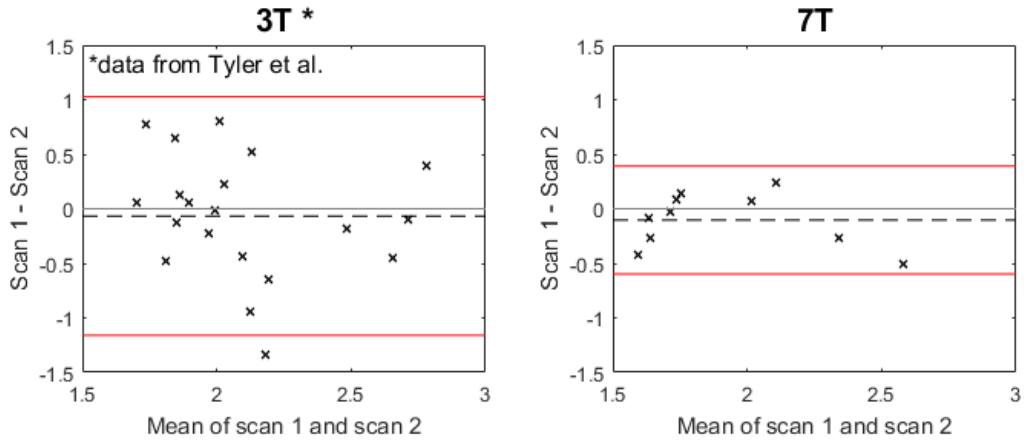


Figure 5.4 Bland altman plots for matched ^{31}P CSI protocols at 3 T and 7 T. Dashed black lines show the bias from zero (solid line). Red lines mark ±1.96 SD

5.2.3 Power calculations and sample size

Sample sizes providing sufficient power to reveal differences in PCr/ATP for paired (e.g. response to stressors or patient longitudinal cohort) studies are given in Table 1. These were calculated using the reproducibility values obtained in this chapter and literature results at 3 T.

Table 5.1 Power calculations showing the sample size needed in a paired study to determine statistical significance (α = 0.05) for 28 min CSI sequence at 7 T, and 31 minute CSI sequence at 3 T, for a change of 0.2 in the measured PCr/ATP.

ΔPCr/ATP = 0.	7 T	3 T*
	28 minutes σ=0.25, α=0.05	31 minutes σ=0.56, α=0.05
Power = 95%	23	104
Power = 90%	19	85
Power = 80%	15	64

* 3 T reproducibility values for this power calculation were taken from the study by Tyler *et al.*, (ref 15). For direct comparison to my results, I have applied my analysis pipeline, i.e. the use of a signed difference to calculate standard deviation, on the original raw data from that study provided by Prof Tyler. Therefore the values given in this table are different to those reported in ref 15, where the standard deviation of the absolute difference in PCr/ATP for scan 1 and scan 2 was used.

5.3 Discussion

I tested reproducibility for a 28 minute 3D-CSI protocol that was designed to give the best spectra in an examination tolerable to cardiac patients. I believe this study reports the first reproducibility data for human cardiac ^{31}P-MRS at 7 T. These are crucial for planning future clinical studies.

Reproducibility of human cardiac ^{31}P-MRS has previously been reported at lower field strengths (summarised in Table 5.2). These studies encompass a range of field strengths, localisation methods and voxel volumes, which makes it hard to draw quantitative conclusions when comparing these studies. However, it is clear that our 28-minute protocol has the tightest reproducibility of all the 3D-resolved protocols, and that it achieves this with a small 5.6mL nominal voxel volume.

Table 5.2 Reproducibility values of human cardiac ^{31}P-MRS from the literature

Reference	Field strength (T)	Cohort size	Acquisition time (min)	Localisation method	Nominal voxel size (cm^3)	Absolute reproducibility (%)[a]
This study	7	10	28	3D-CSI	1.5x1.5x2.5 = 5.6mL	26
Bakermans *et al*, 2017[128]	3	8	7	Single voxel 3D ISIS	$(8.0)^3$ = 512mL	40
				1D ISIS with 1D CSI	-	43
				1D ISIS with 1D CSI	-	44
Tyler *et al*, 2009[62]	3	20	30	3D CSI	1.5x1.5x2.5 = 5.6mL	53
Shivu *et al*, 2010[129]	3	1[b]	23	3D ISIS	4.4x5.5x3.7 = 90mL	31
Schaefer *et al*, 1992[88]	1.5	7	7	1D CSI	-	22
Lamb *et al*, 1996[130]	1.5	16	10	3D ISIS	6.0x7.0x7.0 = 294mL	38[c]
			15	1D CSI	-	-
			30	2D ISIS + 1D CSI	1.0cm thick slices	46[c]

[a] Absolute reproducibility is calculated as (CR ÷ Mean PCr/ATP) × 100%

[b] A single subject was scanned 8 times to assess reproducibility.

[c] Absolute reproducibility was computed by extracting raw values from Figure 5 in ref. 25 using WebPlotDigitizer (https://apps.automeris.io/wpd/

5.3.1 Analysis methods

The midseptal voxel is the most reproducible of all the single voxels and gives PCr/ATP consistent with literature values. The anterior and anteroseptal voxels have higher PCr/ATP values, probably is due to contamination of the “cardiac” spectra by small amounts of skeletal muscle signal that may not be fully suppressed in some scans by the saturation bands (PCr/ATP is approximately 3.5-4.5 in skeletal muscle vs 2 in myocardium).[46] Quantification of PCr/ATP values in the posterior voxels is the least reproducible. This is likely due to a combination of the effects of distance from the surface coil, and of motion in the posterior voxel.

In 2008, Tyler *et al*. performed a cardiac ^{31}P-MRS reproducibility study at 3 T.[62] They used the spectral sum from 3 voxels in their analysis because they observed lower PCr/ATP CRLB than for a single midseptal voxel. They attributed this increase in precision to the gain in SNR from combining signals. In this study, at 7 T, we also saw increased SNR on summing voxels, but no corresponding improvement in reproducibility.

One possibility for these differences could be due to the lower variability in measured PCr/ATP in the anterior voxels in the 3 T study. At 3 T patients were scanned prone, which reduces motion due to breathing and, potentially, therefore skeletal muscle contamination in the voxels close to the chest wall. At 7 T I scanned subjects supine: this is standard practice for 7 T ^{31}P-MRS measurements in Oxford as it facilitates swapping coils between localisation and ^{31}P measurements and is more comfortable for subjects. The increased variation in anterior PCr/ATP measurements would make including them in a summed average less favourable. Had I gated for breathing, the summed average might have been more reproducible than only using PCr/ATP from the mid-septal voxel.

Our analysis method introduces minimal user bias: no spectra were excluded from the study based on appearance and as the rest of the fitting in OXSA is automated, measured PCr/ATP is only dependent on which voxel was selected for analysis. However, as measured PCr/ATP varied at differing anatomical locations across the heart, the selection of the voxel is an

important step. It was therefore important to define anatomically which voxel will be selected for analysis at the start of the study, and ensure that it was used in all subjects.

5.3.2 Assessment of reproducibility

Measurements reported here are consistent with literature values.[6] While repeated measurements of PCr/ATP measured here showed no significant differences to each other, PCr/ATP measured in this work did show significant difference to values measured in 25 DCM patients using an identical 28-minute CSI protocol and the same hardware (1.91±0.36 vs 1.54±0.39, P = 0.01, Figure 5).[9]

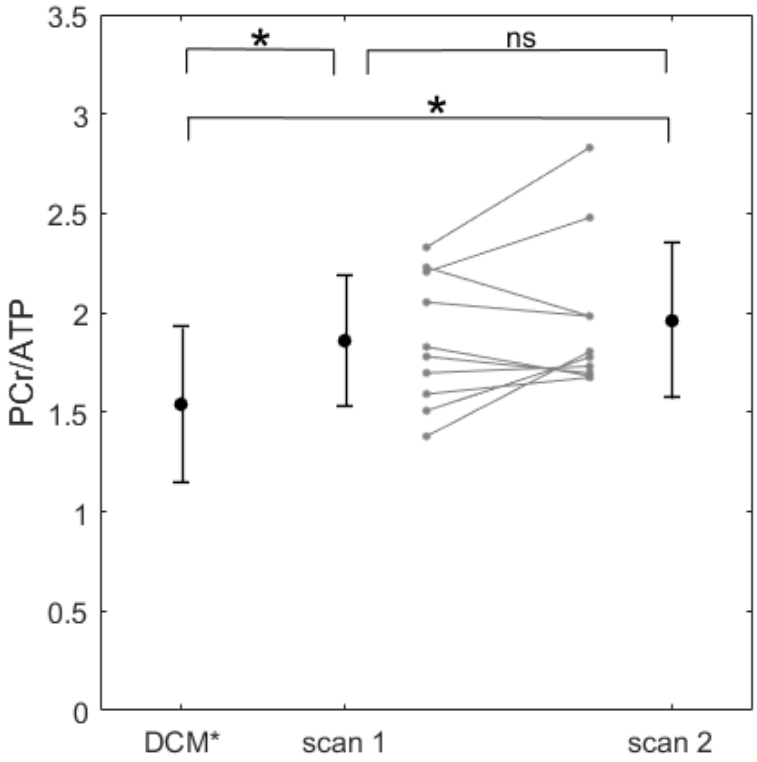


Figure 5.5 Intersubject variability between scans Error bars show ±1 SD. *The leftmost bar shows DCM patient data acquired by Stoll *et al*[49] using the same scanning protocol and hardware for comparison.

Despite SNR limitations, 3 T ^{31}P-MRS has allowed observation of cardiac energetic changes in many disease groups. In recent years, 3 T ^{31}P-MRS has been the most widely used field strength for cardiac phosphorus scans. The 28 minute CSI protocol tested here has equal voxel sizes (5.6mL nominal) and a similar scan duration (28 vs 31 minutes) to the 3 T protocol

tested by Tyler *et al*.[62] In that study, they found intra-subject percentage differences of 20% (absolute difference = 0.43, mean PCr/ATP = 2.10) and a coefficient of reproducibility of 1.1. In this study, we report lower intra-subject percentage differences of 11% (absolute difference = 0.21, mean PCr/ATP = 1.91) and a coefficient of reproducibility of 0.49 (i.e. more reproducible).

5.3.3 Power and sample size

The reproducibility values presented here enable power and sample size calculations to be performed — an important step in the design of clinical studies. The lower intra-subject variability at 7 T compared to 3 T translates to smaller sample sizes required for sufficient statistical power to detect a given effect. For example, in order to detect a change of 0.2 in PCr/ATP with 80% power in a paired study, power calculations from 3 T data from the Tyler *et al*.[62] study predict a required sample size of 64, whereas data from this work predicts only 15 subjects would be required for an equivalent length protocol.

When designing studies, cost is an important factor. Scan fees at 7 T are more expensive compared to an equivalent scan at 3 T: for example, in Oxford at the time of writing, the cost of a 7 T scan is ~35% more than a 3 T scan. Despite this, the smaller cohort size required at 7 T for sufficient statistical power would overall lead to a saving in scan fees, e.g. a 100 x (1 – 1.35 x 15/64) = 68% saving, using values for the 28 minute protocol. Additionally, there would be further savings from the use of fewer consumables and less time spent on patient recruitment. This may also enable a shorter study, delivering more timely information to clinical decision makers. However, at present, our site has more restrictive exclusion criteria for scans at 7 T than at 3 T. Nevertheless, in a recent 7 T ^{31}P-MRS study in patients with dilated cardiomyopathy[49] approximately 60% of patients who completed the laboratory screening form were found to have no safety contraindication to MR imaging at 7 T and were able to participate fully. The challenges of patient safety are not insurmountable at 7 T. In particular, fewer subjects would be excluded if there were access to complete medical device testing data that included 7 T. This is expected to become available in the coming years.

5.3.4 Limitations

The aim this chapter was to assess reproducibility of cardiac PCr/ATP at 7 T in the healthy population. At 7 T the transmit field strength B_1^+ depends strongly on coil loading. And hence the flip angle achieved in the myocardium – and scan signal-to-noise ratios may be different in patient groups whose body shape is different to the healthy volunteers in this study (e.g., obese type 2 diabetes mellitus patients). Reproducibility may need to be assessed in specific disease groups if the exact figure is critical for study design.

5.4 Conclusion

In this chapter, I have reported reproducibility values for human cardiac ^{31}P-MRS at 7 T for the first time. These have further highlighted the benefits of technical developments of performing ^{31}P-MRS at 7 T over lower field strengths will provide the necessary information to design future clinical studies using 7 T ^{31}P-MRS as an endpoint.

6 Development of a short cardiac 7 T ^{31}P MRS protocol

In the previous chapter, I tested the reproducibility of an established 28 minute ^{31}P CSI scan. Here, I modify the scan parameters to develop a much shorter, 6½ minute scan. Acquiring usable ^{31}P spectra fast is highly desirable; particularly because a finer temporal resolution would allow study of the response of cardiac energetics to stressors (e.g dobutamine infusion or exercise).

Before using a shortened protocol, it is important to check whether such a short protocol would be sufficiently robust and reproducible to detect changes in cardiac metabolism with sufficient power for the planned study. In this chapter, I assess performance and reproducibility of PCr/ATP using this 'rapid' 6½ minute 3D-CSI sequence. If sufficiently reproducible, it would allow the study of cardiac energetics at multiple steady states within a single scanning session. Comparison of reproducibility statistics from this chapter with the previous will allow informed decisions when selecting protocols in the design of future studies. Additionally, I investigate the effect of a per-subject B_0 shimming approach on spectral quality and reproducibility.

Work from this chapter contributed to the publication: Ellis, J., *et al*. 2019. Reproducibility of human cardiac phosphorus MRS (^{31}P-MRS) at 7 T. **NMR Biomed**. 32, e4095; doi: 10.1002/nbm.4095.

6.1 Data acquisition

Ten healthy volunteers (3 female, age = 29±6 years, BMI = 23±4 kg/m^2) were recruited according to local ethics regulations. The scanning protocol followed the methodology previously described (§4.3).

Three sets of ^{31}P spectra were acquired in 6 ½ minutes each. The group's standard 3D UTE-CSI protocol was adapted to enable a shorter acquisition time by using an 8×16×8 matrix; nominal voxel size 25×15×25mm^3 and 4 averages (at k=0). Using larger voxels allowed us to

reduce scan duration while keeping enough samples at k=0 to preserve a compact voxel point-spread-function with minimal side-lobes. The differences between parameters used in the 6½ min CSI sequence in this chapter, and the 28 min sequence in Chapter 5 are listed in Table 6.1.

Table 6.1 UTE-CSI sequence parameters for the established 28 minute CSI used in chapter 5, and the modified 6 ½ CSI acquisition in this chapter.

	28 min CSI	**6½ min CSI**
T_A (mins)	28	6.6
Matrix size	16 x 16 x 8	8 x 16 x 8
Nominal voxel size (mm^3)	15 x 15 x 25	25 x 15 x 25
No. of averages	10	4
T_R (s)	1	1

6.1.1 Per-subject shimming

I also tested the effect of a per-subject B_0-shimming algorithm on spectral quality and reproducibility.[131] B_0 maps were acquired as a stack of 18 dual-echo GRE slices aligned with the mid-short axis view (TR 314ms, TE_1 2.4ms TE_2 4.3ms). B_0 maps were measured starting from the scanner manufacturer's default shim settings (referred to as the "tune-up" shim settings). Per-subject shim solutions were obtained by recording a B_0 map which was altered in MATLAB by zeroing all pixels with an intensity less than that in the inferior myocardium and setting the magnitude of all remaining pixels to 1. The phases of the pixels were kept unaltered. This modified B_0 map was then used as input to the scanner's standard shim calculation routines. These modifications prevent the very high intensity pixels near the surface dominating the computed shim solution,[ii] which otherwise tends to degrade the shim quality in the inferior cardiac segments.[131]

The first and third datasets used per-subject B_0 shimming; the second used the vendor's standard "tune up" shim settings. Subjects were then removed from the magnet – this

[ii] we believe that Siemen's shim algorithm is based on a magnitude weighted least squares algorithm, although this is not formally documented anywhere.

constituted ‘session 1’. After a short (~5min) break, these steps were repeated as ‘session 2’. These datasets are labelled A-F (see Fig. 6.1 for detailed description).

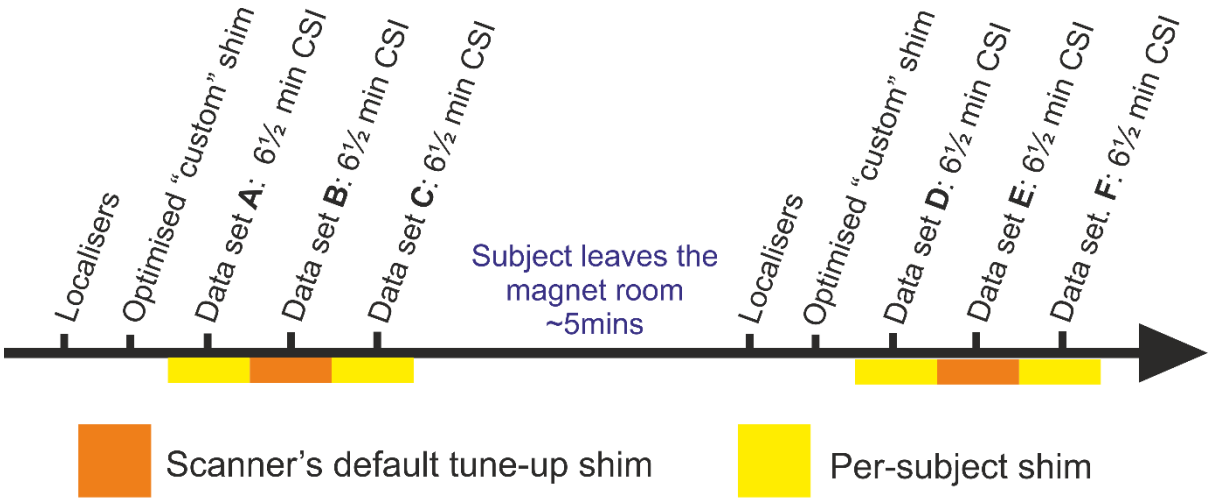


Figure 6.1 study protocol. A ‘session’ was defined as a series of consecutive sequences, acquired without the patient leaving the magnet. ‘Dataset’ refers to a single CSI sequence acquired within a session.

6.2 Data analysis

Reproducibility statistics were calculated as described in §5.1.4. Additionally, as I had repeated per-subject shim PCr/ATP measurements within a single scanning session, I could calculate an intra-session variability for these scans.

Inter-session variability was assessed through the mean and difference between PCr/ATP ratios for each subject.

Inter-subject variability was assessed by the mean and standard deviation of PCr/ATP ratios within the same datasets across all subjects.

Intra-session variability, (only calculated for the per-subject shim) was assessed through the mean and difference between PCr/ATP ratios from equivalent datasets within the same session. i.e. by comparison of dataset A with C and dataset D with F.

The coefficient of repeatability (CR) was calculated from standard deviation of the *signed* differences in PCr/ATP between two scans for each subject according to:

$$CR = SD_{intrasubject} \times 1.96. \quad [1]$$

A *lower* CR reflects a better method. A two-tailed Mann-Whitney U (non-parametric) test was used to compare repeated measurements. Variances were compared using a Brown-Forsythe test.[127] The coefficient of variation (CV), defined as the sample standard deviation divided by the mean, was also computed.

$$CV = SD \,/\, mean. \quad [2]$$

I calculated reproducibility statistics of both the four voxels in the mid-interventricular septum, as well as the statistics for their spectral sum.

6.3 Results

Example spectra from the selected voxels are shown in Figure 6.2. Figure 6.3 gives reproducibility statistics for single voxels, and combinations of voxels summed prior to fitting. As was the case with the longer scan in Chapter 5, the midseptal voxel gives the most reproducible PCr/ATP values. All subsequent analyses therefore calculated PCr/ATP from the midseptal voxel, not the summed voxels.

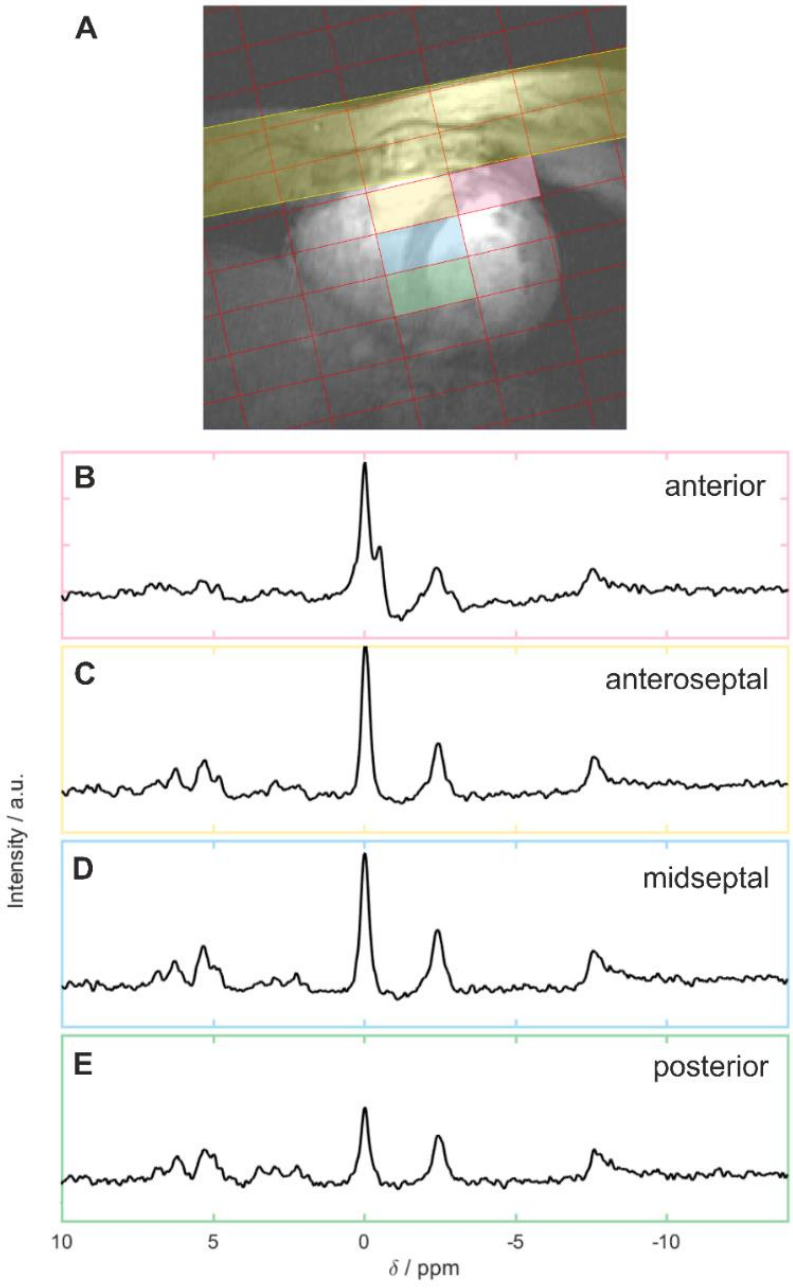
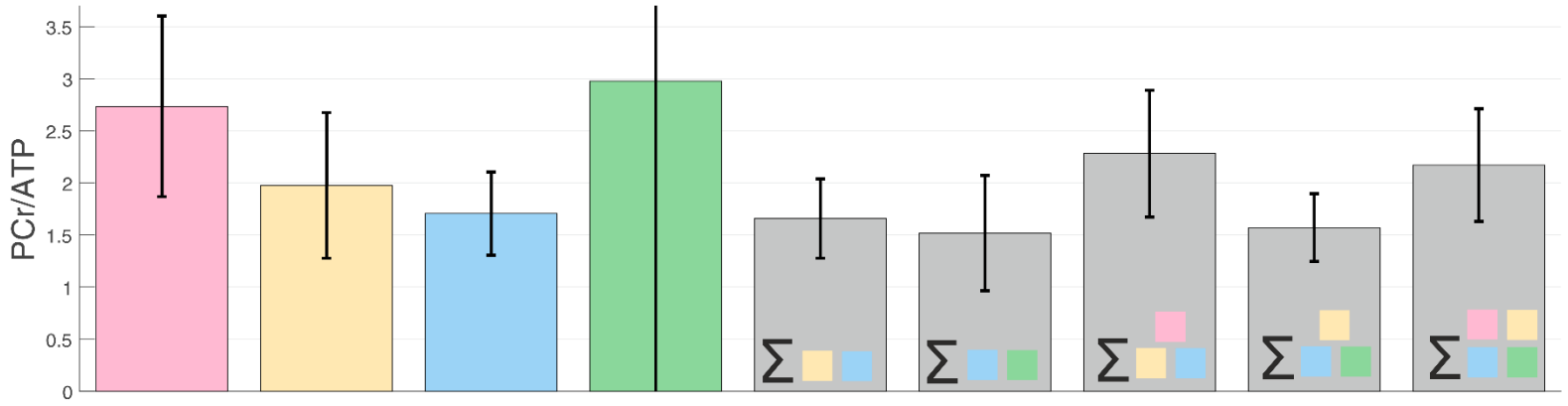


Figure 6.2 **A** Position of the CSI matrix showing the rotation of the CSI grid in the short axis view of the heart. Yellow band marks the location of the BISTRO saturation band intended to supress signal form skeletal muscle. **B-E** Spectra from the corresponding coloured voxel marked on the localiser images



	Anterior voxel	Anteroseptal voxel	Midseptal voxel	Posterior voxel	Anteroseptal + Midseptal	Midseptal + Posterior	Anterior + Anteroseptal + Midseptal	Anteroseptal + Midseptal + Posterior	All 4 voxels
PCr/ATP	2.74	1.98	1.71	2.98	1.66	1.52	2.28	1.57	2.17
PCr SNR	33	32	23	8	50	23	72	55	79
CRLB	12%	9.3%	13%	111%	9.3%	20%	10%	10%	11%
Coefficient of Variation	87%	70%	38%	539%	38%	36%	64%	33%	54%
Coefficient of Reproducibility	1.9	1.5	0.67	19.02	1.01	1.5	1.5	0.86	1.4

Figure 6.3 Variation in PCr/ATP value measured at 4 voxel locations and combinations of spectral sums of these voxels. The table below provide the PCr SNR, the Cramér Rao Lower Bound on PCr (CRLB), the coefficient of variation (CV = inter-subject SD / mean) and the coefficient of reproducibility (CR = 1.96 × inter-scan SD) of the measured PCr/ATP.

6.3.1 Per-subject shimming

There were no significant differences between sessions using the default “tune up” shim (1.69± 0.48 vs 1.79±0.30, *P* = 0.57), or the customised shimming (e.g data-set A vs. C gave 1.64±0.26 vs 1.65±0.17, *P* = 0.97; see Figure 6.5 for full comparison). Mean PCr/ATP values across all scans were 1.76±0.40 for the tune-up shim and 1.70±0.28 for the custom shim, giving CVs of 23% and 17% respectively. The intra-subject variabilities were 0.31±0.14 (tune-up) and 0.29±0.18 (per-subject shim). There was an improvement in the Cramér-Rao lower bounds (CRLBs) between tune-up and the customised shimming algorithms (13.8% vs 10.3%, *P* = 0.02), showing that the higher quality spectra obtained using the customised shimming enabled more precise metabolite quantification. The reproducibilty of PCr/ATP measurements using both shimming techniques was equivalent (CR was 0.66 for the tune-up shim vs 0.67 for the new custom shim).

The inter-examination CR was 0.75 (Figure 6.6D) and the intra-examination CR was 0.67 (Figure 6.6C, both reported for the custom shim comparison). There was no significant difference (P = 0.85) between these inter- and intra-examination changes.

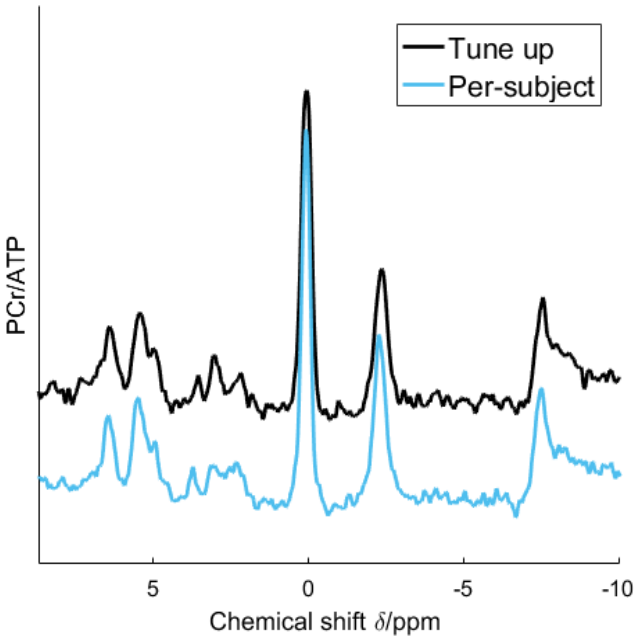


Figure 6.4 Spectra from the same scanning session acquired with tune-up and per-subject shim settings. Peaks visible: 2,3-DPG (5ppm), PDE (2ppm), PCr (0ppm), γATP (-2.5ppm), αATP (7.5pmm).

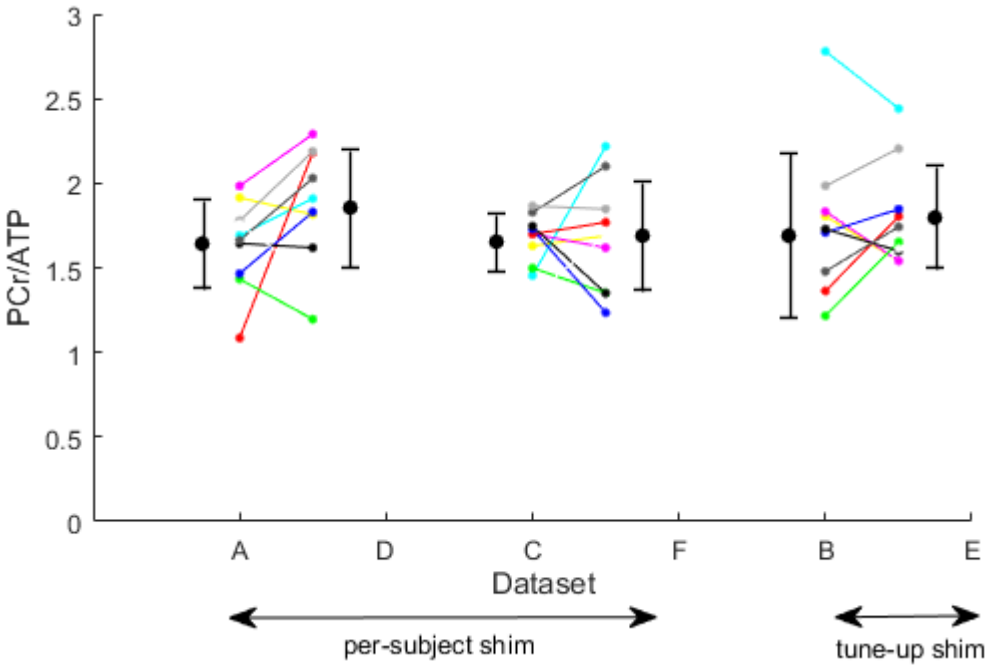


Figure 6.5 Inter-subject variability. Error bars show ±1xSD. Each colour represents PCr/ATP values measured from a particular subject.

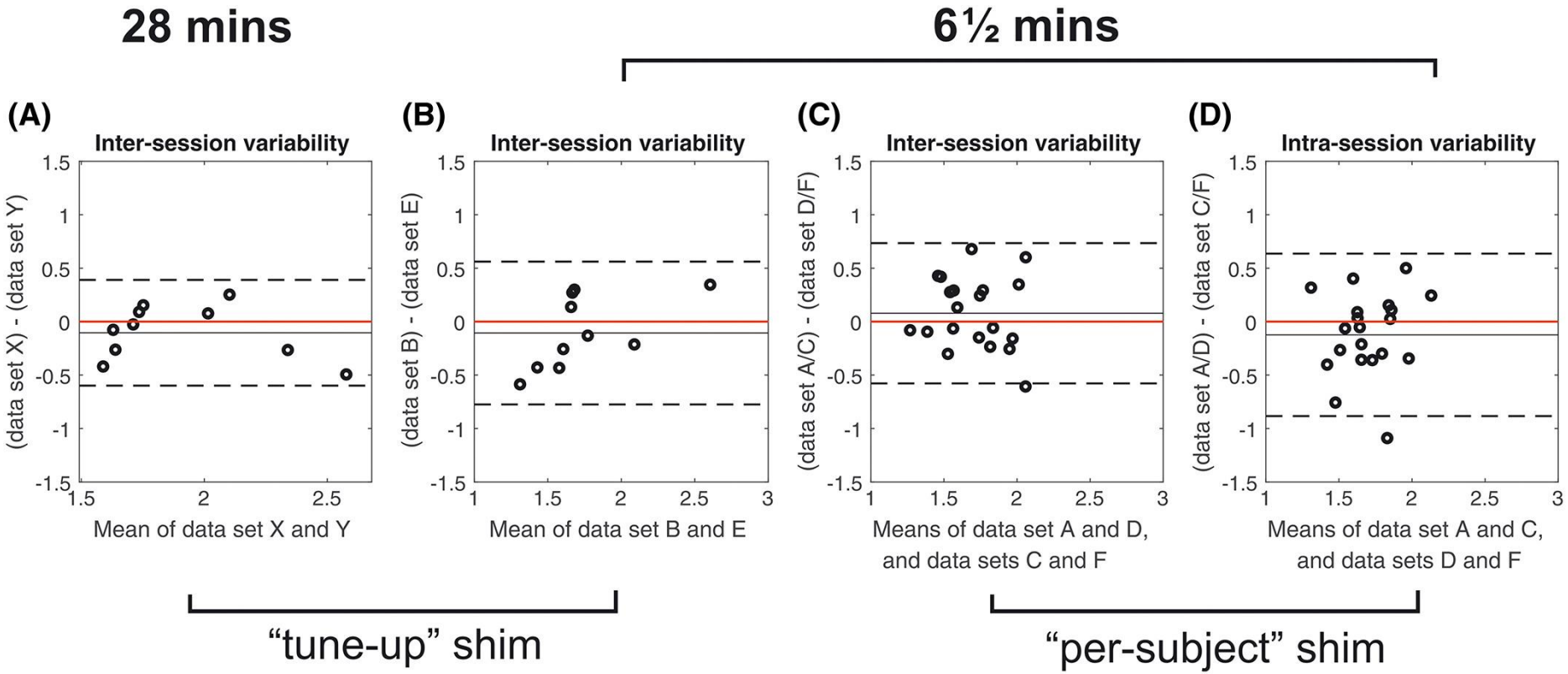


Figure 6.6 A-C, Bland–Altman plots of inter-session variability in PCr/ATP for 28 min CSI from Chapter 5 (A) and 6½ min CSI (B, C). D, plot of intra-session variability for 6½ min CSI with per-subject shimming. Solid black lines show the bias from zero (red line); dashed lines mark ±1.96 SD

6.3.2 Power calculations and sample size

Sample sizes providing sufficient power to reveal differences in PCr/ATP value for paired studies (e.g. response to stressors or patient longitudinal cohort) are given in Table 6.2. These were calculated using the reproducibility values obtained in this chapter, Chapter 5 and literature results at 3 T.

Table 6.2 Power calculations showing the sample size needed in a paired study to determine statsitcal significance (α = 0.05) for both 28 min and 6.5 min CSI sequences at 7 T, and 31 minute CSI sequence at 3 T, for a change of 0.2 in the measured PCr/ATP.

ΔPCr/ATP = 0.2	7 T		3 T*
	28 minutes σ=0.25, α=0.05	6½ minutes σ=0.34, α=0.05	31 minutes σ=0.56, α=0.05
Power = 95%	23	40	104
Power = 90%	19	33	85
Power = 80%	15	25	64

* 3 T reproducibility values for this power calculation were taken from the study by Tyler *et al.* [62] I made this analysis using the original raw data from that study provided by Prof Tyler. If comparing this table to the original study, please note that the values reported in Table 1 of that study were computed using the standard deviation of the absolute difference in PCR/ATP for scan 1 and scan 2, whereas here I have used the standard deviation of the signed difference.

6.4 Discussion

I have tested the reproducibility of a 'rapid' 6½ minute 3D-CSI protocol, which is short enough to allow the assessment of changes in PCr/ATP value during rest, stress and recovery in a single scanning session.

Across all subjects, the SNR of PCr was 1.2× greater in the 28 minute CSI scan tested in Chapter 5 compared to the 6½ minute scan used here (which has fewer averages but larger

voxels). Furthermore, in the 6 ½ minute scan, I observed a larger 2,3-DPG amplitude (3.5 ± 0.62 vs 2.9 ± 1.06, $P = 0.07$), reflecting greater blood contamination from the larger voxels.

Analysis of the midseptal voxel in isolation produced the most reproducible PCr/ATP measurements, the same result as for the longer scan tested in Chapter 5. This analysis was worth repeating for the shorter scan because it could well have been the case that the decreased SNR from the shorter scan meant that the SNR gain from summing several voxels became more favourable.

6.4.1 Assessment of reproducibility

The 'rapid' 6½ minute CSI acquired datasets in less than ¼ of the time to both those in Tyler *et al*.'s 3 T study and the established 7T 28 minute scan tested in Chapter 5. As expected, comparing the two sets of 7 T data, a decrease in scan time led to increased variability in PCr/ATP measurements and therefore a larger CR (0.49 28 minute CSI vs 0.67 6½ minute CSI). Despite this, the reproducibility of PCr/ATP measurements acquired in 6½ minutes at 7 T is still greater than those acquired in 31 minutes at 3 T,[62] meaning that a move to ultra-high field allows for quicker data acquisition without cost to reproducibility. This is important as short ^{31}P acquisition times allow the detailed study of the response of cardiac energetics to stressors, such as exercise or dobutamine infusion. For example, the British Society of Echocardiography's (BSE) recommendations for a dobutamine protocol for assessment of myocardial ischemia are to use four steps each with 3 minutes of dobutamine infusion.[132] 7 T ^{31}P stress using this 6½ min ^{31}P scan would therefore be possible during dobutamine stress complying with these guidelines, whereas a 31 minute scan at 3 T would not be. I note in passing that Dass *et al.* proposed a shorter ^{31}P scan at 3 T with nominal 8min duration (typically ~10min due to heart-rate variability and SAR limits). They demonstrated that their protocol gave similar mean PCr/ATP values to the Tyler *et al.* 31 minute 3 T protocol (Dass *et al.* 8min: 1.83 ± 0.32; Tyler *et al.* 31min: 1.78 ± 0.27).[133] However, the reproducibility of that 8min 3 T protocol has not been reported, so I cannot compare its reproducibility against my 7 T results.

Bakermans *et al* tested the reproducibility of a 7 minute sequence in the human heart at 3 T,[128] performing spatial localisation with 3D ISIS or a combination of 1D ISIS and 1D CSI either perpendicular or parallel to the surface coil.[128] 3D ISIS was found to be the most reproducible of these methods, giving a PCr/ATP of 1.57 ± 0.17 (mean ± SD) and a CR of 0.64. The reproducibility of this 7 min 3 T scan is the same as that achieved in a 6½ min 7 T scan in this work (CR 0.64 3 T vs CR 0.67 this work) but used substantially larger voxel sizes: 3D ISIS voxel size 512 mL. I observed no significant differences between the variances of the intra- and inter- examination differences (P = 0.85), suggesting that the variability in measured PCr/ATP is dominated by error from within the ^{31}P measurement itself, rather than experimental set-up (e.g. coil positioning, localisation). This is in contrast to the finding of Lamb *et al*. in their reproducibility study at 1.5 T.[130] They used a 10cm ^{31}P loop for both transmission and reception whereas in this study I used a bigger coil with a rectangular 26x28cm^2 transmit loop and a flexible 4x4 array of 4cm diameter receive elements. By using a larger transmit coil and an array of receive coils, I have mitigated some of the challenges associated with placing small loop coils and so my results were similar for intra- vs inter-session parameters, presumably because my approach was less affected by coil positioning.

There is some debate in the literature about the possible magnitude of changes in PCr/ATP. Bakermans *et al.* suggested by simulations that the changes in PCr/ATP in healthy subjects upon exercise are on the order of 10%, which they concluded would be impossible to detect by ^{31}P-MRS at 3 T. Exercise-induced changes in patients with disease are known to be more substantial, perhaps because their hearts have only a limited energetic reserve because of having to compensate for disease at rest. For example, Betim Paes Leme *et al.* observed a 57% decrease in PCr/ATP in patients with Chagas heart disease on exercise.[134] Such changes would be clearly detectable at 7 T. It is an open question whether 7 T ^{31}P-MRS can be made sensitive enough to detect changes in high-energy phosphate energetics in healthy subjects during exercise.

6.4.2 Per-subject B_0 shimming

Per-subject B_0 shimming improved the precision of the fit of PCr/ATP, as indicated by the lower CRLBs (mean 13.8% for tune-up shim *vs* 10.3% for per-subject shimming, $P = 0.02$). However, on our system, the reductions in the linewidths of PCr and γATP were not significant and there were no improvements in reproducibility (CR 0.67 tune-up, CR 0.66 per-subject). Presumably uncertainties in optimising the shim solution counter-balanced the improved spectral SNR in terms of reproducibility. Additionally, as no cardiac triggering or respiratory gating were used, the calculated shims only apply exactly at one phase in the cardiac and respiratory cycle, which might explain the lack of improvement in reproducibility. It is not therefore immediately obvious whether per-subject B_0 shimming for cardiac ^{31}P-MRS at 7 T is worth the additional examination time that is required: two iterations of the shimming algorithm add two 20s breath holds to the protocol plus a little time for ROI drawing and loading the shim.

If a single 6½ minute ^{31}P measurement is being included in an examination, then it is likely that per subject B_0 shimming is not worth the extra time. In this case, if time permits, better data would probably be obtained by using the time that would have been spent shimming to acquire more averages in the CSI protocol. However, if stress-response energetics are being monitored (and therefore a CSI protocol is being repeated multiple times while the subject remains in the magnet) then all of the datasets would benefit from performing the per-subject shimming algorithm at the start of the scan.

Our difficulties with image-based shimming at 7 T may stem from the inhomogeneous transmit fields produced by the 10cm ^{1}H surface coil I used. More sophisticated proton coil designs with better coverage, and dual-tuned designs may tip the balance in favour of per-subject B_0 shimming.[135]

6.5 Conclusion

I have presented a short 6½ min CSI protocol that gives reproducible spectra of a quality

previously reported for 30min acquisitions at 3 T,[62] but in a time short enough for use in stress-response studies. The combined reproducibility statistics from this chapter and Chapter 5 now allow informed decisions to be made when deciding on a 7 T ^{31}P MRS cardiac protocol for future studies. Additionally, I have shown that per-subject B_0 shimming improved spectral quality, but had a negligible impact on measurement reproducibility.

7 The effect of a ketone drink on cardiac energetics

Exogenous ketones have been shown to improve cardiac output in patients with heart failure with reduced ejection fraction (HFrEF).[136] In this Chapter I perform a pilot study for investigating whether the mechanism via which exogenous ketones act to improve cardiac output involves changes to the cardiac PCr/ATP ratio. PCr/ATP is assessed before and after consumption of ΔG® – a commercially available ketone drink – in a group of healthy volunteers using the 6½ minute CSI protocol developed in Chapter 6.

The work in this chapter was performed in collaboration with Dr Adrian Soto from the Department of Physiology, Anatomy and Genetics (DPAG) at the University of Oxford. He recruited the participants and has kindly provided the data obtained from blood samples that are included in this chapter. Unless otherwise stated, all the other work is my own. The scan fees for this work were funded by the creators of ΔG®, TΔS Ltd.

7.1 Introduction

For people living with type 2 diabetes, cardiovascular disease is the primary cause of death. Diabetes Mellitus (DM) is an independent risk factor for heart failure[137] of which one of the hallmarks is impaired cardiac energetics.[5] PCr/ATP is known to be suppressed in diabetic patients.[138] However, there is currently no specific treatment available for cardiovascular disease associated with diabetes; one possibility are exogenous ketones which have been shown to improve cardiac output in patients with heart failure.[136] In this chapter I present a proof of principle study, assessing the feasibility of using a ketone ester drink (known as "ΔG®") as a treatment for heart failure in those with diabetes, measuring PCr/ATP as a

surrogate biomarker for heart failure using 7 T ^{31}P-MRS. I measured PCr/ATP values in a group of 12 healthy volunteers before and after consumption of the drink, using the 6½ minute ^{31}P CSI scan, developed in Chapter 6.

7.1.1 Background

In the healthy heart, metabolism of free fatty acids (FFA), glucose, and lactate produce ATP in the mitochondria. However, in the diabetic heart, glucose and lactate oxidation are decreased[139,140] and fatty acid oxidation is increased.[141] Since FFA metabolism is a less efficient source of energy compared to glucose metabolism (in terms of amount of ATP produced for a given amount of oxygen consumed), the oxygen demands of the diabetic heart are greater. [141–143]

In 'healthy' metabolism, insulin plays a role in the inhibition of lipolysis (see Figure 7.1). However, in diabetes, insulin resistance leads to lipolysis inhibition being impaired, causing a rise in free fatty acid (FFA) levels in the blood.[144]

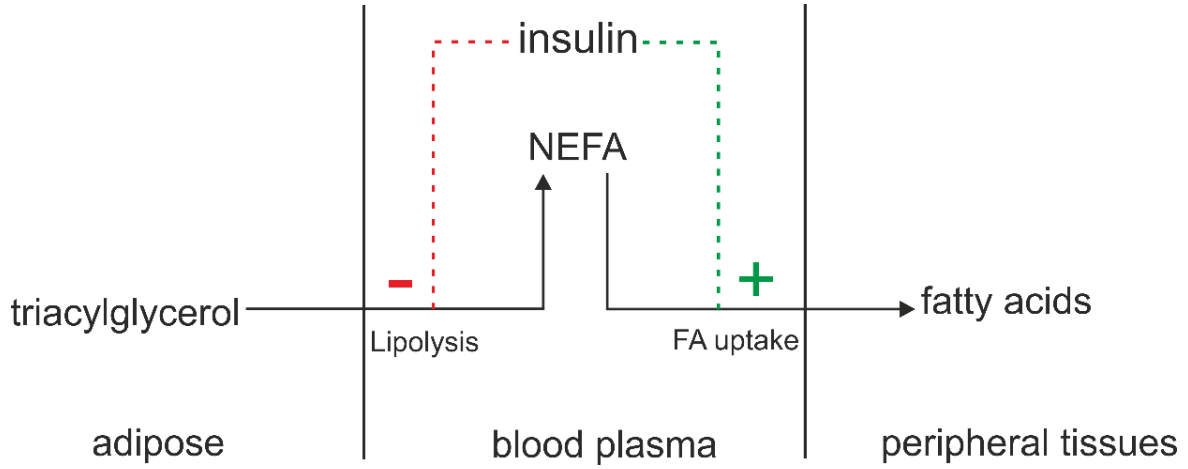


Figure 7.1 The role of insulin in non-esterified fatty acid (NEFA) dynamics. Two processes are regulated by insulin: 1) fatty acid (FA) release from adipose tissues and 2) FA uptake by peripheral tissues (adipose, heart, skeletal muscle). Insulin resistance therefore causes a rise in plasma FFA concentrations. Figure adapted from Ramos-Roman *et al.*[145]

Fatty acids are the natural ligand of the peroxisome proliferator-activated receptors, PPAR-α. PPARs are pivotal in the control of uncoupling protein (UCP) genes.[146] When PPAR-α is activated by FFA ligands, it upregulates the transcription of UCPs. FFA blood concentration

has already been shown to correlate with the expression of UCPs in the heart[147]. UCPs are mitochondrial membrane transporters – they expend the mitochondrial membrane proton gradient producing heat rather than ATP. This process is important for thermoregulation, e.g. in brown adipose tissue. But, it necessarily reduces the production of ATP and may be undesirable in the heart.[146] Furthermore, PCr/ATP has been shown to correlate negatively with plasma FFA acid concentrations in both healthy and diabetic subjects.[138]

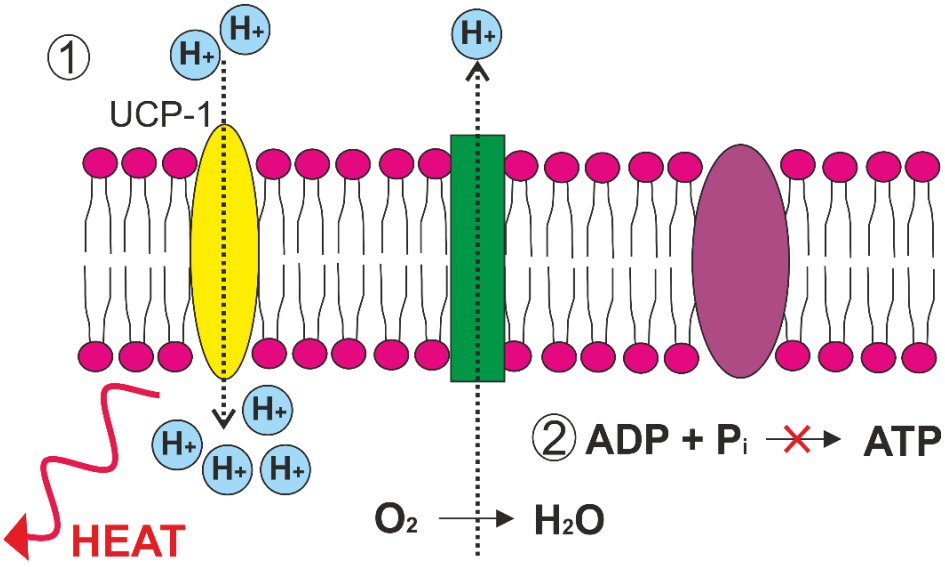


Figure 7.2 1) activation of the UCP1 channel by fatty acids (via PPAR-α) lowers the proton gradient by allowing H^+ to return to the mitochondria, producing heat. 2) The reduced proton gradient leads to a drop in the production of ATP. Adapted from Figure 18.45 in the textbook 'Biochemistry' by Berg *et al*.[148]

7.1.2 The potential role of ketone bodies

In diabetes, increased lipolysis causes a rise in FFA levels in the blood. The ketone body, beta-hydroxybutyrate (βOHB or 3-OHB), has been shown to inhibit lipolysis via a separate pathway (the PUMA-G receptor).[149] In the 1990s, isolated rat hearts perfused with a combination of βOHB and insulin showed an improvement in hydraulic work and improved energetics of cytosolic ATP hydrolysis.[150] More recently, a human study by Nielsen *et al* investigated the effect of infusing patients with heart failure with reduced ejection fraction (HFrEF) with βOHB.[136] They observed a dose-dependent improvement in cardiac output, left ventricular ejection fraction (LVEF), and a reduction in systemic vascular resistance (SVR) upon infusion of the ketone body. Furthermore, there was no effect on the myocardial external energy efficiency (MEE), defined as stroke work/myocardial oxygen consumption (MVO_2), in

either the HFrEF group, or age matched healthy volunteers. This led to the conclusion that βOHB may potentially constitute a novel treatment for heart failure patients.

In the meantime, a ketone ester drink named ΔG® has been developed by Prof Clarke's group at DPAG, University of Oxford and then through her spin-out company TΔS Ltd. The drink quickly elevates βOHB blood levels and has been proven to be safe for consumption by healthy humans.[151] We therefore wanted to test the effect of consumption of ΔG® on cardiac energetics (via measurement of PCr/ATP), with a view to assessing it as a potential treatment for heart failure in patients with diabetes.

7.1.3 Study design and aims

The long term goal of this study would be to test whether PCr/ATP is restored in diabetic heart failure on consumption of ΔG. However, in the first instance, we performed a feasibility study in healthy volunteers aged 18-70. The primary aim of this pilot study was therefore to investigate whether the proposed protocol of fasting, ΔG consumption, blood samples and two ^{31}P scanning sessions was feasible.

We also investigated whether effects of ΔG consumption on cardiac PCr/ATP could be seen in healthy subjects. Using the reproducibly statistics from Section 6.3.2, we calculated that in order to detect a change in PCr/ATP of 0.3 with a statistical power of 80% and an α probability of 0.05, 12 participants would be needed. Subjects fasted for 24 hours before the study to increase FFA levels. FFA levels have been shown to correlate inversely with PCr/ATP in healthy subjects[138] – it therefore seems reasonable to expect PCr/ATP to be reduced in these healthy volunteers after fasting for 24 hours. We hypothesised that consuming the ΔG ketone drink would reduce the concentration of FFA (by inhibiting lipolysis) and restore PCr/ATP.

7.2 Methods

Study design

12 healthy volunteers (6M/6F, 38±14 yrs, BMI 22.9±2.3 kg/m^2) were recruited and scanned in accordance with ethical guidelines. Subjects were asked to fast for the 24 hours prior to their scan. The study protocol is shown in Figure 7.3. Briefly, a single 6½ ^{31}P MRS CSI data-set

was acquired as described in Section 6.1. Following this, the subject was removed from the scanner and a blood sample was collected prior to consumption of the ketone drink. A second ^{31}P-MRS CSI data-set was acquired 30-40 minutes after consumption of the drink, followed immediately by a second blood sample.

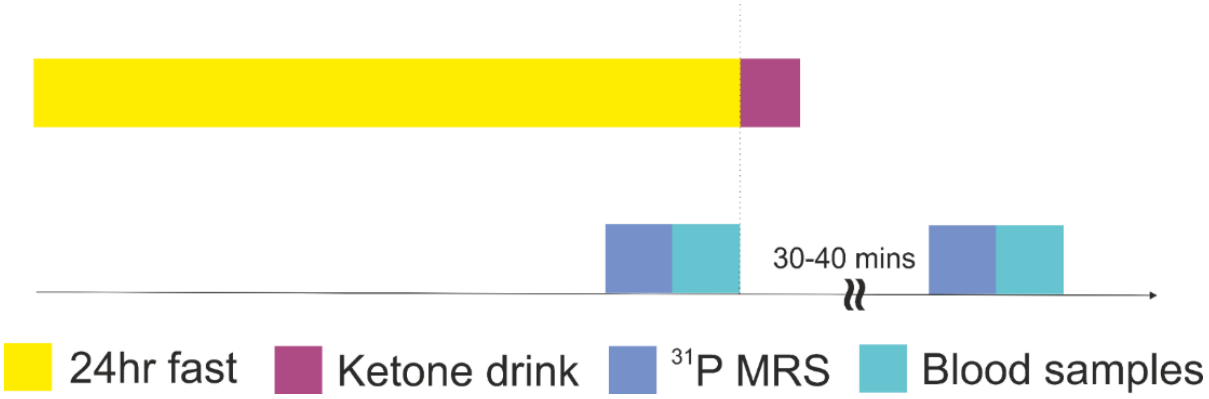


Figure 7.3 Study protocol

Blood samples

Blood samples were collected and analysed by Dr Adrian Soto. Plasma glucose, free fatty acids (FFA), lactate and βOHB were assayed using a commercial semi-automated bench-top analyzer (ABX Pentra, Montpellier, France).

^{31}P-MRS data

Data acquisition followed the protocol laid out in Section 6.1. The quadrature coil was used for localisation, and the 16-channel array used for ^{31}P measurements. PCr/ATP was quantified using the midseptal voxel only, as this was previously shown to give the most reproducible PCr/ATP (Section 6.3). Analysis followed the procedure described in Section 6.2. Significances in difference in PCr/ATP before and after the consumption of the ketone drink were tested for using a Mann Whitney-U test.

7.3 Results

The ^{31}P scan before and after the ketone drink was well tolerated by all subjects. After consumption of the ketone drink, plasma levels of βOHB were increased in all subjects

(0.73±0.32mmol/L before vs 3.98±1.07mmol/L after, p= 7.4 x 10^{-7}), and concentrations of FFAs and glucose were reduced in all subjects (1.08±0.32mmol/L vs 0.55±0.20mmol/L, p=0.000032 and 5.00±1.01mmol/L vs 3.56±0.66, p=0.00047 respectively). Blood lactate also decreased from 1.84±0.45mmol/L to 1.32±0.32mmol/L (p=0.0037, Figure 7.4)

There were, however, no changes in cardiac PCr/ATP after 35-40 minutes of acute ketosis induced by the ketone drink, (1.86±0.30 before vs 1.83±0.32 after, p=0.99, Mann Whitney U test). The mean CRLB for PCr/ATP across all 24 PCr/ATP measurements was 13%.

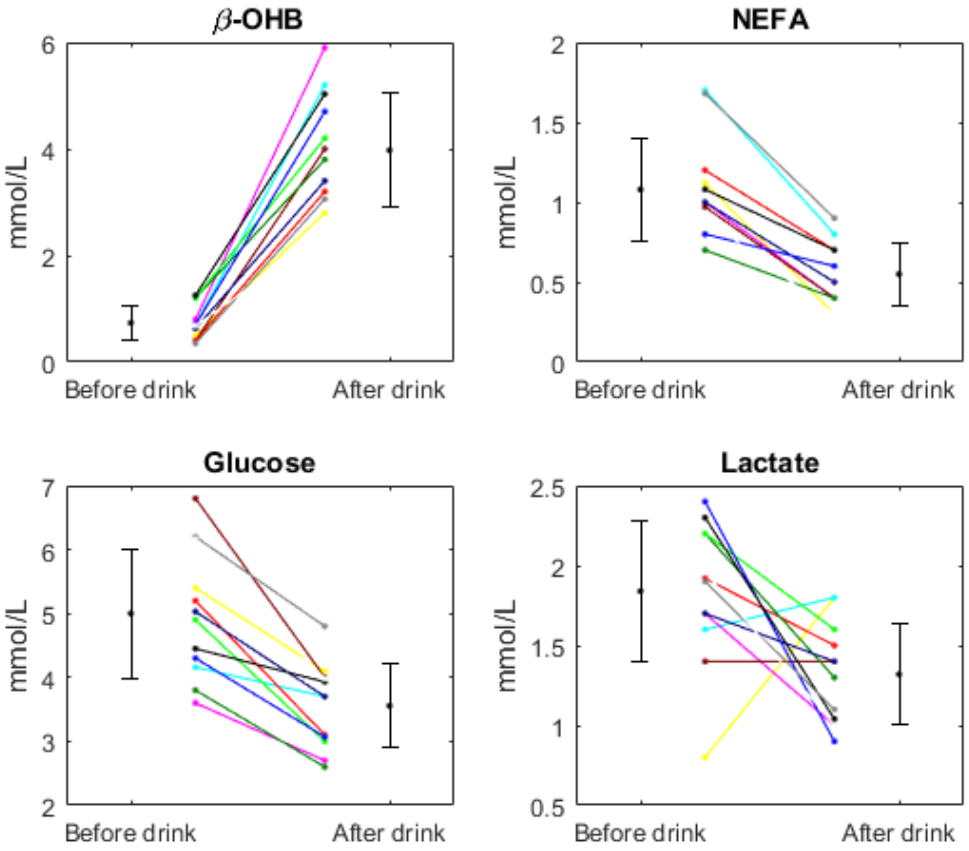


Figure 7.4 Plasma concentrations of the ketone body β-OHB, non-esterified fatty acids (NEFA), glucose and lactate before and after the concentrations of ΔG. Coloured lines correspond to results from the same participant. Black error bars mark the mean±SD across all volunteers. Data was collected by Dr Soto, DPAG, University of Oxford.

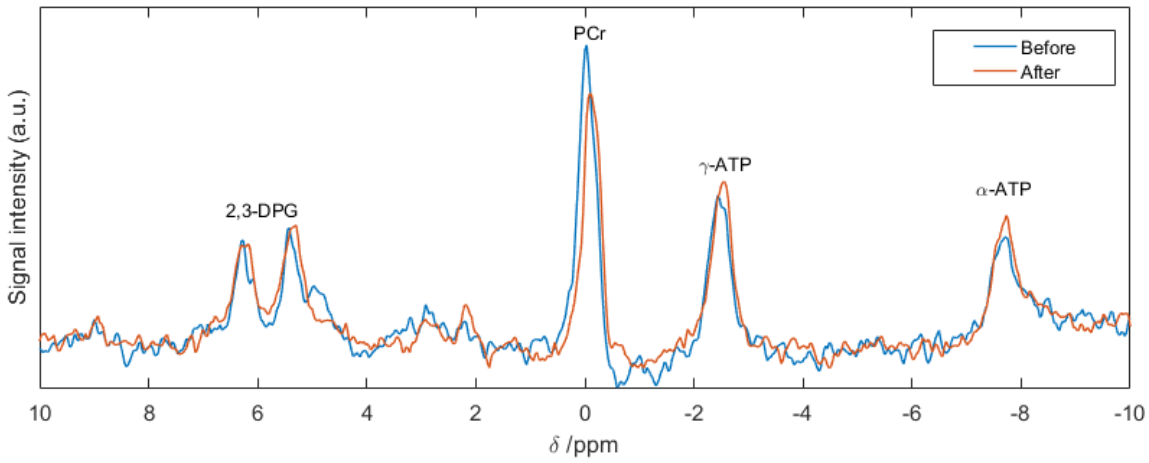


Figure 7.5 Example of a typical midseptal cardiac ^{31}P spectra before and after consumption of ΔG.

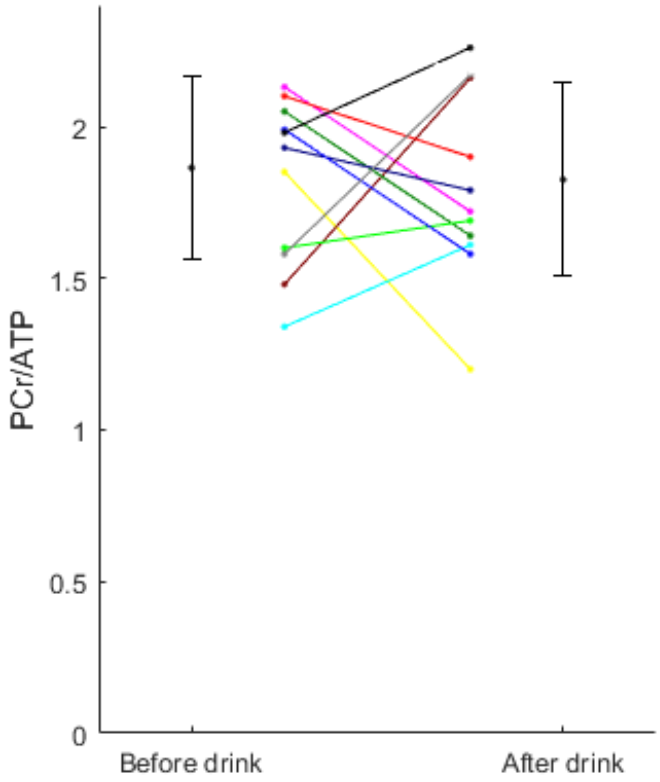


Figure 7.6 PCr/ATP before and after consumption of ΔG. Lines have been coloured to match those from Figure 4. Black error bars mark the mean±SD across all volunteers.

7.4 Discussion

The mean CRLB of PCr/ATP across all 24 measurements was 13%, which is the same as the CRLB measured in healthy volunteers in the reproducibility study of the ^{31}P-MRS protocol (Chapter 6) that I used in this chapter. From a ^{31}P-MRS methods point of view, this study has been a success – we have shown the feasibility of the protocol and the improved sensitivity of 7 T allowed us to show that ΔG® has no effect on PCr/ATP (1.86±0.30 before vs 1.83±0.32 after, p=0.99) with a small cohort size (12). In order to demonstrate this effect at 3 T, calculations from 3 T reproducibility statistics[62] show that 30 subjects would have been required for the same statistical power. This is a large number of participants for a 'proof of principle' study. Furthermore, the longer scan time required at 3 T would have resulted in participants spending longer in the scanner (~2hrs total at 3 T compared to ~90 minutes in total at 7 T) in order to obtain two PCr/ATP measurements, which may have been intolerable

to some of our volunteers. The longer required scan time at 3 T would also give a lower temporal resolution – i.e. the measurement at 7 T shows PCr/ATP over a 6 ½ minute window, whereas at 3 T any effect would have been blurred over the 30 minute scan. Furthermore, the cost of scan fees would also have been more – accounting for a longer scan slot, and the larger sample size at 3 T, the cost of performing the study would have been 65% more.

Consumption of ΔG® ketone ester drink significantly elevated levels of βOHB in the blood. At the end of the study, mean βOHB plasma concentrations were 4mM – these are endogenous ketone levels that would be expected with more prolonged fasting periods than 24 hours. [152,153] Concentrations of FFAs in the blood were successfully reduced, but this did not translate into an increase in PCr/ATP, contrary to previous observations that these two parameters are inversely correlated in healthy subjects.[154]

Of course, the primary limitation of this study was the use of healthy volunteers, where PCr/ATP was not suppressed as it is known to be in diabetic subjects. While the idea that fasting for 24 hours would reduce PCr/ATP was reasonable based on previous data showing an inverse correlation between FFA levels and PCr/ATP in healthy subjects,[136] the PCr/ATP that we measured are still within the normal range in healthy subjects.[6,62,155] We did not measure PCr/ATP in our specific group of volunteers before they started their fast, but given that after fasting PCr/ATP was still 'normal', the size of the effect (if any) of this fasting protocol on PCr/ATP in healthy subjects is likely to be below the threshold for detection by 6 ½ min 7 T ^{31}P-MRS.

Now that we have established feasibility of this protocol, to answer our wider question as to whether ΔG® can improve cardiac energetics in diabetic patients, the next step should be to repeat these measurements in a cohort of diabetic patients.

In this study, we were not able to obtain cardiac hemodynamic measurements such as ejection fraction that have previously been shown to be improved in heart failure patients administered exogenous ketones.[136] This is because the quality of ^{1}H images obtained at 7 T with currently

available hardware in Oxford is not good enough to allow measurement of such parameters while also acquiring ^{31}P measurements. Ejection fraction would have been possible to measure at 3 T, as there is a built in ^{1}H body coil. In the future, the use of a combined ^{1}H and ^{31}P body coil at 7 T should make these measurements possible in a single scan session.[135]

Another limitation is that we take just one measurement after the ketone drink. In the full study, it could be interesting to monitor PCr/ATP after a more prolonged period of ketosis, e.g. 4 hours after consumption of ΔG.

7.5 Conclusions

I have demonstrated that the 'short' ^{31}P-CSI scan I developed in Chapter 6 can be used to successfully obtain multiple PCr/ATP measurements in an interventional study. The ^{31}P-MRS scan session following consumption of ΔG was well tolerated by all subjects – this suggests that the protocol proposed in this chapter is feasible for use in a larger study of diabetic patients. We have also shown, that in healthy volunteers, there are no detectable changes in PCr/ATP after 25-40mins of acute ketosis from consumption of ΔG®.

8 A multiple spin-echo CSI sequence for ^{31}P MRS at 7 T

This chapter presents a multiple spin-echo (MSE) CSI sequence for cardiac ^{31}P-MRS at 7 T that has the aim of measuring ^{31}P transverse relaxation times (T_2 values). Previous chapters have focussed on the impacts of the improved SNR inherently available at 7 T compared to lower field strengths. However, in other organs at 7 T, further SNR improvements have been achieved by use of ^{31}P MSE sequences, notably in breast tissue and the liver.[156,157] The secondary motivation of the work in this chapter was therefore to investigate the suitability of applying such an approach in the heart to further improve SNR above that afforded by the standard UTE-CSI acquisitions.

While I was performing the work in this chapter, the COVID-19 pandemic led to the closure of university buildings. It was sadly therefore not possible to test the proposed sequence *in vivo.* These will be important experiments to perform once scanning can resume. The proposed sequence has been implemented in IDEA, Siemens' pulse programming environment, and is ready for testing once scanning can resume. A plan of future phantom validation and *in vivo* experiments is included in this chapter for discussion. Despite this setback, the results of the simulations in this chapter still represent a significant contribution to assessing the potential success of ^{31}P MSE in the heart at 7 T with currently available hardware.

8.1 Background and motivation

I had two motivations for implementing a multi echo sequence:

1) Measuring the transverse relaxation times (T_2 values) of ^{31}P metabolites
2) Enhancing SNR by combining the signal from the FID and subsequent echoes.

The rest of this section discusses the motivation and background for these aims.

8.1.1 Aim 1: MSE sequences to measure T_2 values

The ultimate goal of ^{31}P-MRS is quantitation of metabolites: T_2 determination is therefore important as knowledge of metabolites T_2 values are essential for reliable quantification at intermediate and long TEs. Familiarity of relaxation times are also significant for protocol design (e.g. determining the optimal TR, or as a design parameter in RF pulse optimisation). Furthermore, ^{31}P T_2 values could even be a useful biomarker. There is precedent for this since lower ^{31}P T_2 values have been measured in breast cancer tissue.[158]

The first ^{31}P study of the human heart at 7 T was published by Rodgers *et al* in 2014.[6] In that study, the T_1s of Pi, 2,3-DPG, PCr and α-,β- and γ-ATP were determined using a Look-Locker chemical shift imaging (LL-CSI) sequence. The study also reported T_2 values of these metabolites as, in order to determine the T_1s, it was necessary to fit T_2 values in the Bloch simulation of the pulse sequence. However the only sensitivity to T_2 relaxation times in that study came from the inversion pulse, leading to T_2 measurements with high standard deviations.[6] To my knowledge, these are the only ^{31}P T_2 values to have been reported in the human heart, at any field strength.[iii]

8.1.2 Aim 2: MSE sequences for SNR enhancement

The rationale for using MSE sequences as a way to enhance SNR is given clearly by van der Kemp *et al*[159] as they introduced the AMESING method for breast applications. Their argument can be summarised as follows.

[iii] Web of Science search using terms ‘phosphorus spectroscopy relaxation heart’ resulted in no papers reporting human cardiac T_2 values. Search performed December 2020.

Improvements in SNR can in theory be achieved by averaging signal from the FID and multiple echoes. The signal from each symmetric echo can be thought of as twice the signal S_0 from a half echo, or FID, with the same difference in echo time (ΔTE). Assuming perfect refocussing, the summed signal of the two parts of the j^{th} symmetric echo is therefore:

$$S_j = 2S_0 e^{-j\Delta TE/T_2}$$

[8.1]

The total signal, S_t, from a FID and n symmetric echoes can hence be written:

$$S_t = S_0(1 + 2\sum_{j=1}^{n} e^{-j\Delta TE/T_2})$$

[8.2]

We can form a weighted average signal S_{wa}, where the signals are multiplied by a weighting factor w_j and divided by the sum of the weighting factors:

$$S_{wa} = \frac{S_0 w_0 + \sum_{j=1}^{n}[S_j w_j]}{w_0 + 2\sum_{j=1}^{n} w_j}$$

[8.3]

If we assume that the noise in every FID or half echo is Gaussian with standard deviation σ_0^2, then the weighted average noise variance is:

$$\sigma_{wa}^2 = \sigma_0^2 . \frac{w_0^2 + 2\sum_{i=1}^{n} w_i^2}{(w_0 + 2\sum_{i=1}^{n} w_i)^2}.$$

[8.4]

Using the weightings:

$$w_0 = 1 \text{ and } w_j = e^{-j\times\Delta TE/T_2},$$

[8.5]

and substituting in equation [8.1] we can rewrite the average signal as:

$$S_{wa} = S_0 . \frac{1 + 2\sum_{i=1}^{n} e^{-2i\Delta TE/T_2}}{1 + 2\sum_{i=1}^{n} e^{-i\Delta TE/T_2}},$$

[8.6]

and the weighted average noise as:

$$\sigma_{wa}^2 = \sigma_0^2 . \frac{1+2\sum_{i=1}^{n}[e^{-\frac{2i\Delta TE}{T_2}}]}{(1+2\sum_{i=1}^{n}[e^{-i\Delta TE/T_2}])^2}.$$

[8.7]

Combining [8.6] with the square root of [8.7] and defining as $SNR = \frac{S}{\sigma}$, gives:

$$SNR_{wa} = SNR_0 . \sqrt{(1 + 2\sum_{i=1}^{n}[e^{-\frac{2i\Delta TE}{T_2}}])}.$$

[8.8]

The SNR enhancement E_{wa} attributed to a weighted average of multiple spin echoes is therefore:

$$E_{wa} = \sqrt{(1 + 2\sum_{i=1}^{n}[e^{-\frac{2i\Delta TE}{T_2}}])}.$$

[8.9]

Figure 8.1A shows the SNR enhancement as a function of $\frac{T_2}{\Delta TE}$ for weighted averaging using this model. SNR enhancement is predicted for all T_2 values, with the greatest benefits seen at high T_2 values; as $T_2 \rightarrow \infty$, the predicted SNR enhancement tends to $\sqrt{2n+1}$. The SNR benefit is also greater at shorter echo times, which makes intuitive sense: at short echo times, the signal in the echoes will be greater as there will have been less time for signal to be lost due to intrinsic T_2 decay.

Assuming steady state conditions, T_1 effects can also be considered. Figure 8.1B shows the SNR per unit time for different pulse sequences: a pulse-acquire (PA) sequence at both 90º and the Ernst angle (EA), and an MSE sequence with 7 full echoes at differing values of $T_2/\Delta TE$.

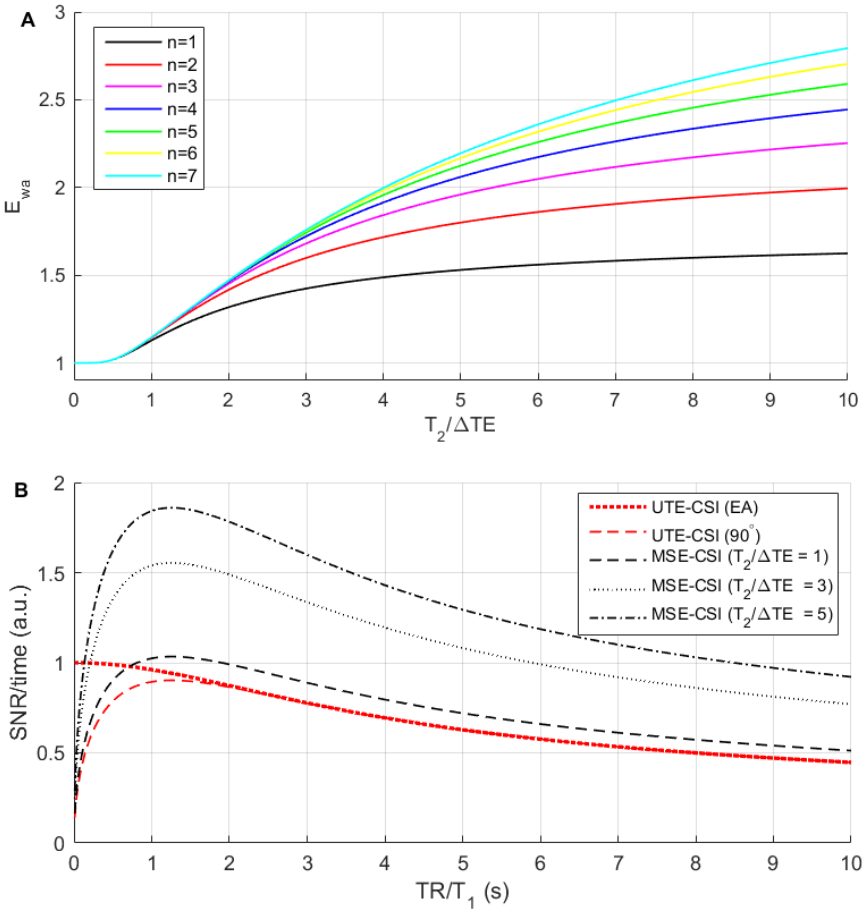


Figure 8.1 A Expected SNR enhancement by performing a weighted average of one FID and n symmetric echoes (equation [8.9]) with fixed TR and T1. **B** SNR per unit time comparison for the standard pulse-acquire UTE-CSI sequence (red) run at 90º and the Ernst angle (EA). Black lines show SNR/time for MSE-CSI sequences with 7 full echoes at differing values of $T_2/\Delta TE$.

8.2 Previous measurement approaches

In this section I discuss the multiple spin echo ^{31}P MRS sequences and protocols that have been applied in other organs, and assess whether these could be used in the human heart at 7 T. There are two pulse sequences in the literature (Figure 8.2):

1) AMESING Adiabatic Multiple Echo Spectroscopic Imaging (AMESING) uses an adiabatic half passage (AHP) pulse[160] for excitation and a BIR-4 pulses (i.e. 4 AHP segments with phase shifts) for refocusing. The number of echoes can be chosen to be between one and five. AMESING has been implemented to both enhance SNR and measure ^{31}P T_2 values.[156,157]

2) Composite block pulse refocusing MSE A 3D-CSI MSE sequence with composite block pulses for refocusing. The sequence measures a FID and seven full echoes with an echo spacing of 45 ms. This sequence has been used to measure ^{31}P T_2 values in the human brain at 7 T.[161]

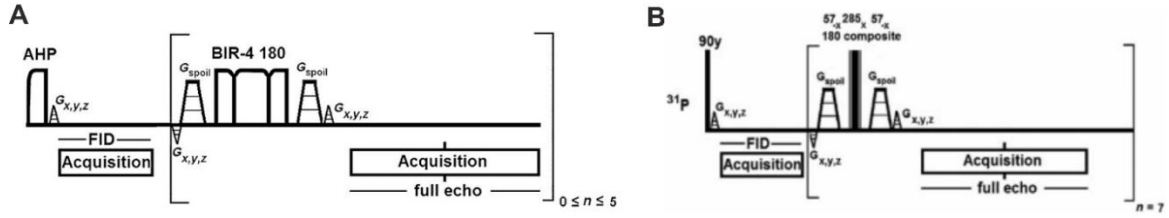


Figure 8.2 The AMESING (**A**) and composite-block refocusing (**B**). Figures adapted from refs.1 and 6. ***A*** *Reproduced with permission, copywright John Wiley & Sons,* ***B*** *used under the CC BY-NC 4.0 licence.*

8.2.1 Suitability of previous approaches for cardiac ^{31}P-MRS at 7 T

AMESING uses adiabatic pulses. Adiabatic pulses are desirable because they result in a uniform flip angle across a range of B_1^+ values. AHP pulses have been shown by Valkovic *et al* to be feasible in the heart at 7 T.[48] In that work, the main challenge was designing a pulse that had an adiabatic threshold of less than 16.5 μT which was the maximum available B_1^+ in the heart at the time (with the "quadrature coil", section 4.1.2). The resulting AHP pulse had 7.5 ms duration compared to the 2 ms AHP pulse used in AMESING for the liver.[159] A BIR-4 pulse comprising four of these AHP segments would therefore be impractical, both due to the amount of non-recoverable T_2 relaxation that would occur during the long (30 ms) pulse (section 8.3), and due to SAR limitations. It is also possible that the Siemens broadband RF amplifier would introduce "droop" during such a long, high-amplitude pulse.[iv]

Another family of adiabatic pulses are the hyperbolic secant (HS^n) pulses.[162] A ^{31}P HS inversion pulse has been implemented in the heart at 7 T by Rodgers *et al*, but required a pulse length of 28 ms.[6] Again, a pulse this long may not be practical to use for refocusing owing to the relaxation that would occur while the pulse is being played out. Furthermore, the

[iv] "Droop" refers to the amplifier running out of "oomph".

quadratic phase following HS pulses is problematic for selective refocusing. In the popular semi-LASER single-voxel MRS sequence, this phase is compensated using pairs of HS pulses with reversed phase, but for MSE MRS this would double what is already a very long pulse.[163,164]

Numerically optimised composite pulses offer an attractive solution. They offer a degree of insensitivity to B_1^+, while typically requiring lower peak B_1^+ and SAR requirements than their adiabatic counterparts.[165] However, the composite pulses used in the "Composite block pulse refocusing MSE" sequence had a peak B_{1+} = 40 μT, higher than that which is achievable with hardware currently available in Oxford. It was therefore necessary to optimise a new pulse, bearing in mind these hardware constraints.

8.3 MSE pulse design considerations

While ^{31}P metabolite T_2 values have not been measured in the heart at 7 T, based on literature values in other organs they are expected to be short (ranging from ~20-200 ms, Table 8.2). This means that for the MSE sequence to be successful – both at enhancing SNR and measuring T_2 values – a similarly 'short' echo time will be required. This is illustrated in Figure 8.1A, where for $\frac{T_2}{\Delta TE} < 0.5$ there is no signal enhancement. We therefore expect a minimum ΔTE of approximately 40 ms to be required in order for SNR enhancement in metabolites with the lowest T_2 values (e.g. αATP).

The minimum echo time will largely be dictated by the length of the refocusing pulse: refocusing pulse length and other design considerations are considered in the following section.

8.4 Refocussing pulse design

Selecting an appropriate refocusing pulse was an important first step in designing the MSE sequence as characteristics of the chosen pulse (e.g. pulse length, SAR deposition) inform acquisition parameters of the final sequence (e.g. echo time, TR).

The following factors were considered when choosing a refocusing pulse that was suitable to use with the hardware available in Oxford:

- **Performance at peak B_1^+ of 16.5μT.** The "quadrature coil" surface coil can reliably achieve a maximum B_1^+ of 16.5μT at the depth of the human heart (Chapter 4). This excluded the use of adiabatic pulses, as discussed in the previous section.

- **B_1^+ sensitivity.** The use of a surface coil meant that B_{1+} varied across both the myocardium, and between volunteers. While the limited peak B_{1+} afforded by the "quadrature coil" rules out adiabatic pulses, B_{1+} insensitivity was still highly desirable.

- **Available bandwidth of the pulse**. A broadband pulse (with bandwidth at least 16 ppm) would simultaneously refocus all spins in the cardiac ^{31}P spectrum. However, broadband pulses are typically short. It was therefore questionable whether a peak B_{1+} of 16.5 μT was enough to achieve a 180º rotation in a sufficiently short pulse. An alternative option was to use a longer, lower amplitude selective pulse. This second approach required the experiment to be repeated at multiple offset frequencies to cover all cardiac ^{31}P metabolites. With this approach, some of the time lost from having to repeat the experiment could be regained by interleaving measurements at different frequencies.

- **Pulse length.** The ideal pulse would be infinitely short. T_2 dephasing during the pulse is non-recoverable. Therefore, a reasonably short pulse was important for accurate measurement of metabolite T_2 values. Shorter pulses also allow for shorter echo times; $\frac{T_2}{\Delta TE}$ is a key parameter in the SNR enhancement offered by an MSE sequence (Figure 8.1), so a short pulse was also favourable from an SNR perspective.

- **RF Heating / SAR.** Pulses that produce high levels of RF heating were undesirable. SAR is proportional to $\int |B_{1+}|^2 dt$, so from a SAR perspective, long, low-power pulses were preferable.

The "optimal" pulse for cardiac ^{31}P-MRS at 7 T is a compromise between these factors.

8.4.1 Methods

The potential refocusing pulses that I considered are described as follows, and will be referred to using the names given here for the rest of this chapter. The amplitude and phase modulation waveforms of all evaluated pulses are shown in Figure 8.3. I considered two 'types' of each pulse – one selective and one broadband (17ppm).

BLOCK

A block-shaped pulse with the required duration to achieve the desired bandwidth calculated from equation 2.13, section 2.4. The pulse amplitude was set to the lower of the calculated B_{1+} required to achieve a 180º flip angle, or 16.5μT.

COMP-BLOCK

Three-part composite block pulses, where the length of each block shaped component was set to the same value as the BLOCK pulse of the corresponding desired bandwidth. Sub-pulses were optimised over discrete grids of B_0 and B_{1+} ranges. A B_{1+} range of ±20% was used for both pulses: optimisation was performed between 13.2 -19.8μT at intervals of 0.2μT. The γB_0 grid varied from -1000Hz to +1000Hz in intervals of 100Hz. For the broadband pulse, the target flip angle at all points in the B_0 grid was 180º. For the selective pulse, the target flip angle was 180º between -100Hz and +100Hz and set to zero elsewhere.

The amplitudes (A) and phases (ϕ) of the sub-pulses were numerically optimised by minimisation of the cost- function:[166]

$$\delta_\alpha(A,\phi) = \frac{1}{mn}\sum_{i,j=1}^{m,n}\left|\frac{\alpha_{i,j}^{S}(A,\phi)-\alpha^{T}}{\alpha^{T}}\right|,$$

[8.10]

where α^T is the target flip angle and α^S is the simulated flip angle, calculated by $\cos^{-1}(\frac{M_z}{M_0})$. m and n correspond to the discrete grid of B_0 offsets and the B_{1+} range over which the optimisation was performed. Sub-pulse amplitudes were allowed to vary freely between 0 and 16.5 μT, and phases were free to vary over the entire range of $\pm\pi$ radians. Minimisation was performed using MATLAB's "fmincon" function.

COMP-SINC

A three-part composite pulse, whereby each sub-pulse is the central lobe of a sinc function. The motivation for this being to reduce the "ripple" in the frequency response outside of the desired bandwidth. Optimisation was performed in the same manner as for the COMP-BLOCK pulses.

OPT-CONTROL

A numerically optimised composite pulse consisting of a series of block-shaped sub-pulses (i.e. constant amplitude and phase within each sub-pulse). Each pulse was comprised of 101 sub-pulses, with a total pulse duration of 8 ms.

Optimisation was based on code provided by Vencel Somai (University of Cambridge) and employed a Shinnar-Le Roux design,[167] fine-tuned using the "fminunc" function in MATLAB, which was used to adjust the amplitude and phase of the individual pulse points.[168]

The ideal frequency profiles were specified as a passband of 150Hz for the selective pulse and 2000Hz for the broadband pulse. B_1^+ was limited to a maximum of 16.5 µT. The weights of the frequencies in the passband double those in the stop band. The corresponding RF pulses for the desired frequency responses were first calculated using an inverse Shinnar-Le Roux transform.[169]The amplitude and phase of the resulting RF pulse were then fine-tuned by minimising the residual sum of squares between the ideal and observed excitation profiles. This optimisation was performed over a discrete grid of B_{1+} amplitudes ($i = 0..m$, 13.2 -19.8 µT at intervals of 0.2 µT) and frequencies ($j = 0..n$ ± 1000Hz, in intervals of 100Hz).

$$minimise \sum_{i=0}^{m} w_i \sum_{j=0}^{n} \left\| \boldsymbol{M}_{i,j}^{S} - \boldsymbol{M}_{i,j}^{T} \right\|^2$$

[8.11]

Where $\| . \|^2$ is the l^2 norm and w_i is the weighting assigned to the each frequency offset.

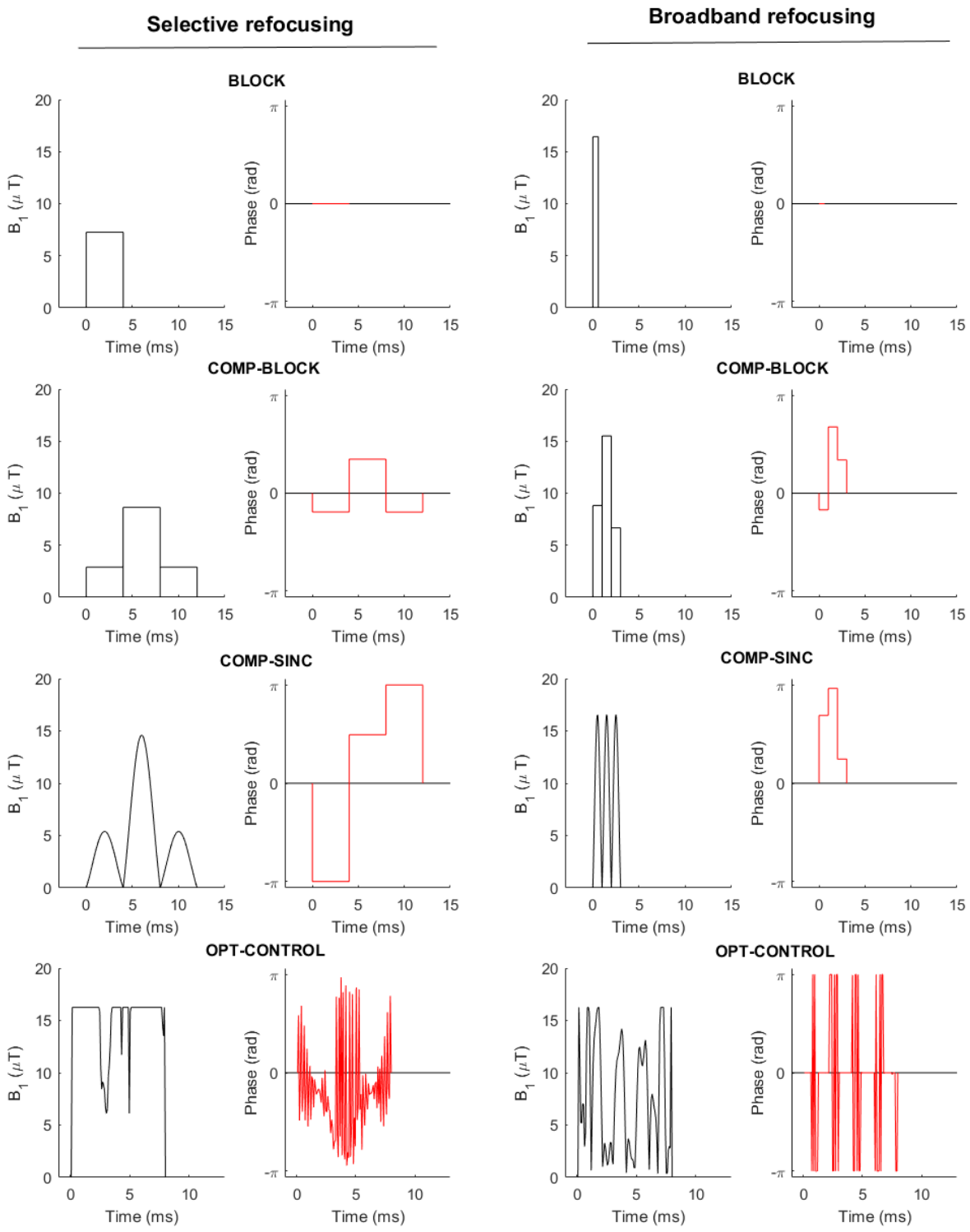


Figure 8.3 Amplitude (black) and phase (red) modulation waveforms for the 8 refocusing pulses considered for the MSE sequence. Rows correspond to a pulse type. The left hand column corresponds to selective pulses, the right hand column to broadband pulses. All pulses are plotted with the same axes limits for easy comparison.

8.4.2 Results

The simulated flip angles are presented for the grid of optimised B_0 and B_1^+ values in Figure 8.4. The presentation order corresponds to that of Figure 8.3. The peak B_1^+ is not high enough to produce a flip angle of 180º in the BLOCK, COMP-BLOCK and COMP-SINC broadband pulses. The longer broadband OPT-C pulse achieves the desired flip angle in regions, but does not do so consistently over all frequencies in the ^{31}P spectrum. A broadband refocusing pulse with a maximum $B_1^+{}_{max}$ = 16.5μT was therefore considered an unfeasible approach for the remainder of this work.

Flip angles of 180º were achieved by all of the selective pulses. As expected, the BLOCK pulse shows the lowest degree of insensitivity to varying B_1^+. For the composite pulse, replacing the block shaped sub-pulses with the central lobe of a sinc function reduces ripples in the stop-band.

Both the COMP-SINC and OPT-CONTROL selective pulses offer selective refocusing over the optimised B_{1+} range. Table 8.1 gives the relative SAR of each pulse. Of all the pulses, the relative SAR of the optimal control pulses is the highest, perhaps because SAR was not included in the cost function for optimisation.

Table 8.1 Pulse length and relative SAR for all considered pulses. Relative SAR calculated as $\int {B_{1+}}^2 dt$ where peak B1+ was the same for all pulses. Rows are grouped by target bandwidth of the refocusing pulse.

	Refocusing pulse	T_p (ms)	Relative SAR (a.u.)
Selective	BLOCK	4	1.00
	COMP-BLOCK	12	2.10
	COMP-SINC	12	2.98
	OPT-CONTROL	8	11.6
Broadband	BLOCK	0.6	0.366
	COMP-BLOCK	3	1.78
	COMP-SINC	3	2.23
	OPT-CONTROL	8	4.52

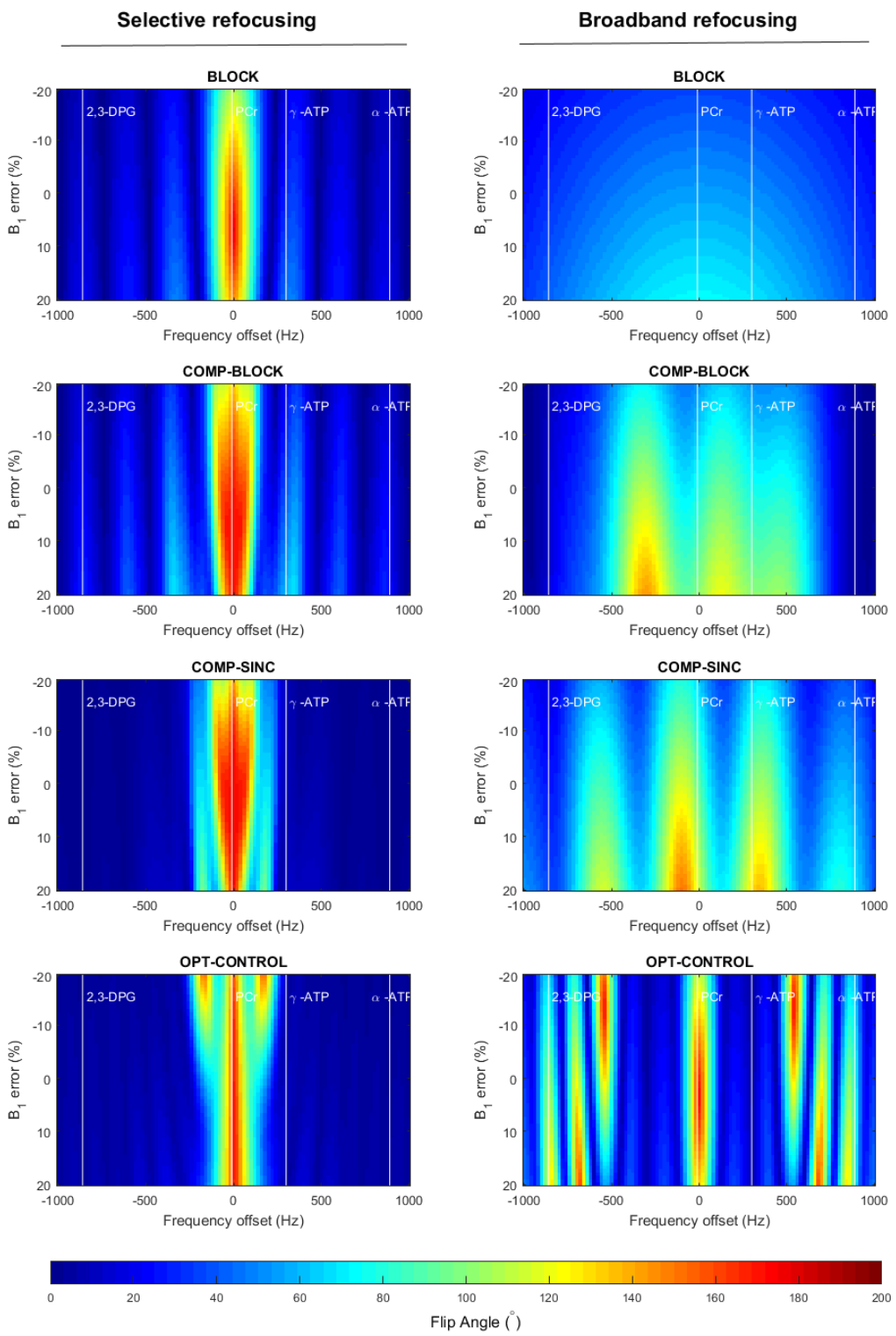


Figure 8.4 Simulation results indicating performance of refocusing pulse on B_{1+} – $\gamma\Delta B_0$ grids relevant to ^{31}P cardiac MRS in the human heart at 7 T. The left hand column corresponds to selective pulses, the right hand column to broadband pulses.

8.4.3 Planned point-source phantom validation

The COVID-19 pandemic and the resulting closure of University buildings meant that it was not possible to validate the simulated refocusing pulse performance in a phantom. Had scanning been possible, I would have performed the following experiments in a phantom containing a main saline-filled chamber (18 L of 73 mM NaCl) with a single, small cube (2 × 2 × 2 cm^3 of 1.8 M K_2HPO_4) inside. This phantom gives one singlet signal that originates only from the cube.

By using inversion as a proxy for refocusing, I intended to assess the flip angles of the refocusing pulses over a range of B_{1+} amplitudes and frequency offsets. I have implemented the sequence shown Figure 8.5 in IDEA (Appendix B). The 180° refocusing pulse would invert the spins, followed by a 90° pulse calibrated at the start of each scan session to produce a FID. The time between pulses would be kept to a minimum.

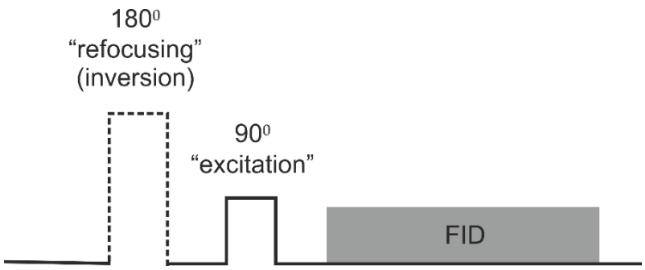


Figure 8.5 Pulse sequence for 180º pulse phantom validation. Dotted line shows where 180º pulse can be exchanged for the refocusing pulse being tested.

B_{1+} insensitivity

I planned to assess the B_{1+} profile of the pulses by sweeping the voltage of the 180° pulse from 0 V to the maximum. A plot of S/S_0, where S is the measured signal and S_0 is the signal at 0 V, should have resembled the sketch in Figure 8.6 if the pulse were performing as desired.

S/S_0 would initially be at a maximum – in the absence of the 180° pulse, all signal would be excited into xy-plane by the calibrated 90º block pulse. As B_{1+} of the refocusing pulse is increased, S/S_0 would decrease, passing through y=0 where the flip angle of the “180°” pulse, α, equaled 90º. At this point, the combined effect of both the ‘180°’ and excitation pulses

together would have been a 180º inversion. Then, at B_{1+} values corresponding to $90^0 < \alpha < 180^0$, S/S_0 would decrease further, reaching a minimum where α = 180º. Provided the refocusing pulses were somewhat insensitive to B_{1+} (as they were designed to be) the plot would 'flatten off' at this minimum, indicating that the pulses had achieved α = 180º over a range of B_{1+} values. If it were possible to achieve a higher B_{1+}, S/S_0 would have then increased again, indicating $\alpha > 180^0$.

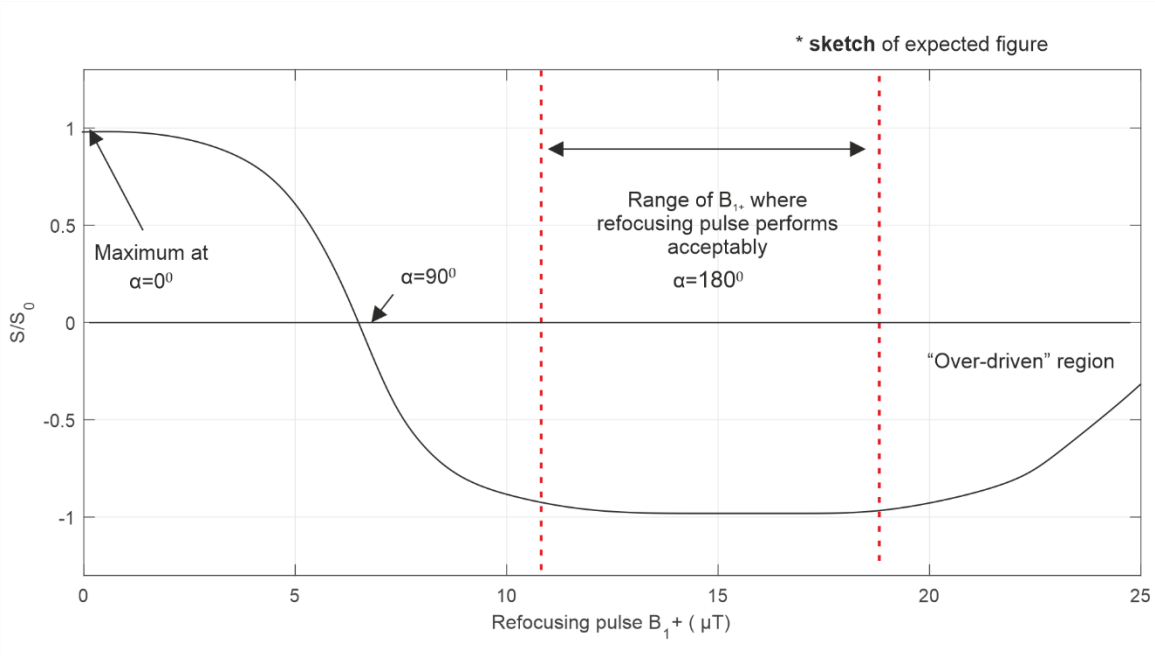


Figure 8.6 Sketch of expected signal as a function of B_{1+} in proposed phantom validation experiment using the 180° pulse initially for inversion because we have prior experience of inversion recovery sequences.

Off-resonance performance

I would also have tested the off-resonance performance of the refocusing pulse by sweeping the frequency of the refocusing pulse from -1000Hz to +1000Hz, while keeping the 90º pulse on resonance. In the frequencies corresponding to the refocusing pulse passband and stopband, $\frac{S}{S_0}$ would be expected to equal -1 and +1 respectively, consistent with α = 180º and α = 0º, respectively. After the initial assessment as an inversion pulse, I would have repeated the assessment with the order of the FID and the 180º swapped and used a variable TE to verify that the refocussing performance broadly matches the inversion performance.

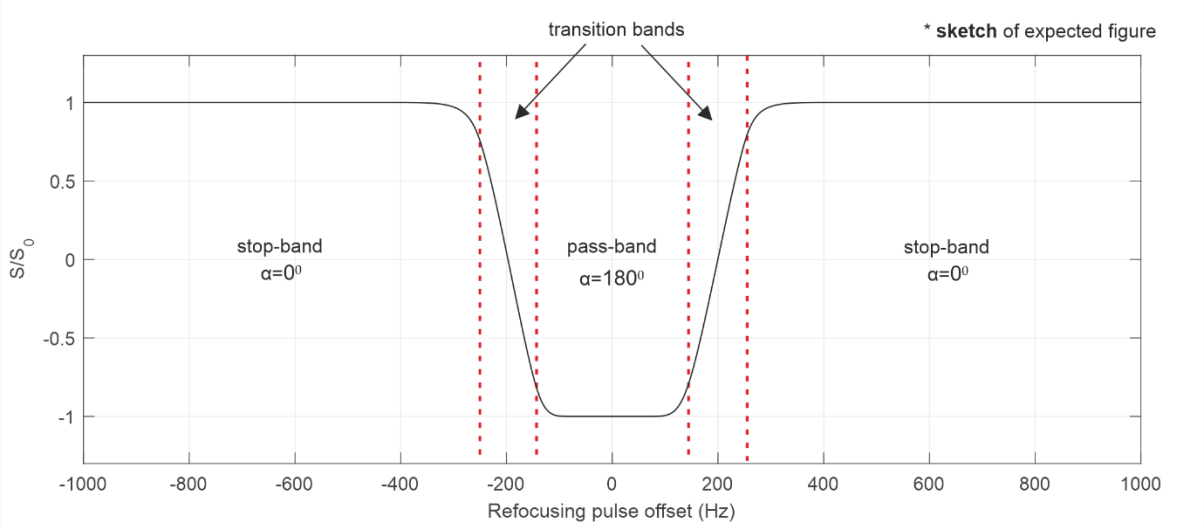


Figure 8.7 Sketch of expected signal as a function of frequency offset in proposed phantom validation experiment.

8.4.4 Chosen refocusing pulse

The 12 ms COMP-SINC selective pulse offered the best combination of B_1^+ insensitivity, frequency selectivity and SAR requirements of all the pulses that were considered, and was therefore used in the remainder of this work.

8.5 Proposed ^{31}P MSE CSI sequence

The proposed MSE CSI sequence is shown in Figure 8.8. Since it was not possible to use a broadband refocusing pulse covering the full spectrum, it was necessary to repeat acquisitions centred on each metabolite. However, as the chosen refocusing pulse is selective, scan time was reduced by interleaving acquisitions. An interleaved approach required the excitation pulse to also be selective – I chose to use a 12ms sinc pulse with a 4ms central lobe to match the bandwidth of the COMP-SINC pulse (Figure 8.9).

Using the following parameters: 8 x 16 x 8 matrix size; 25 x 15 x 25 mm^3 nominal voxel size; 4 averages; ΔTE = 45 ms; and TI = 1 s (defined here as time between interleaves), effective TR = 5 s for each interleaf, gave a total acquisition time of 33 minutes.

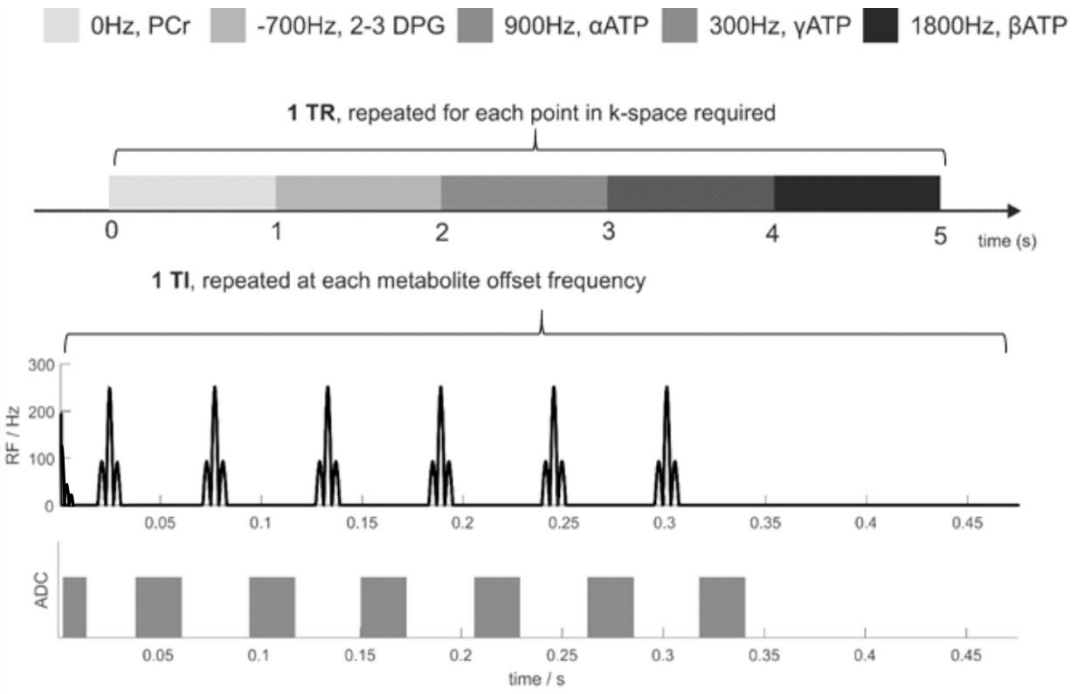


Figure 8.8 Pulse sequence diagram of proposed ^{31}P MSE CSI sequence. Each TR is made up of five time intervals (TI), each centred on a different metabolite from the ^{31}P spectrum.

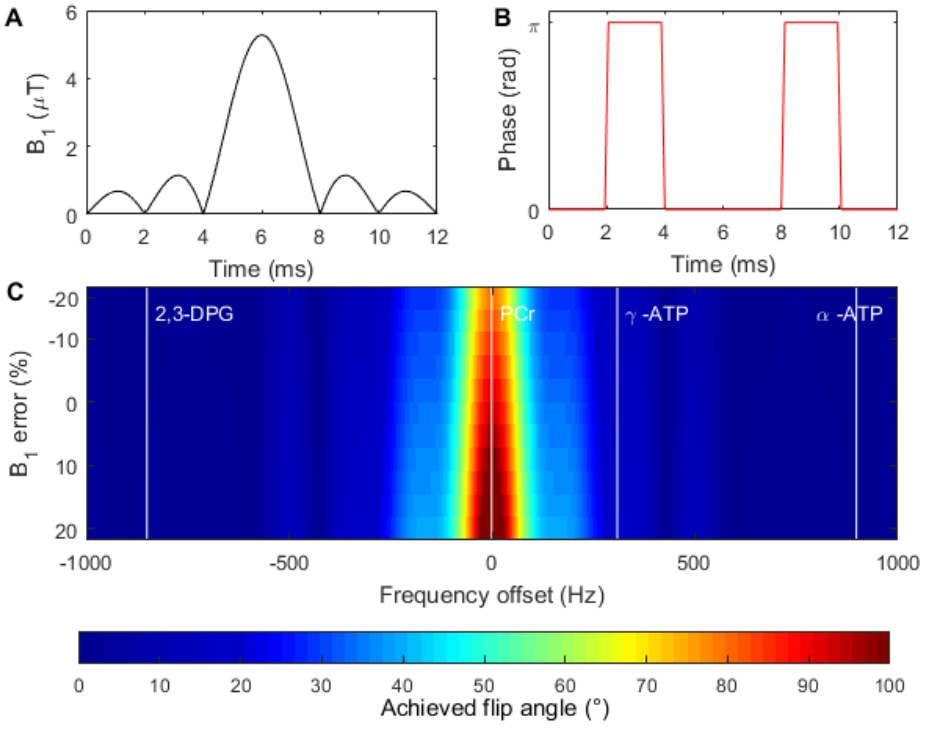


Figure 8.9 Amplitude (**A**) and phase (**B**) modulation waveforms of the 12ms sinc **excitation** pulse. **C** Simulated flip angle of sinc pulse on B_{1+} – ΔB_0 grid relevant to ^{31}P cardiac MRS in the human heart at 7 T.

8.5.1 Simulations

8.5.1.1 Methods

The following simulations were performed to assess the expected performance of the proposed sequence *in vivo*. Magnetisation values were calculated using a numerical Bloch-McConnell simulation of a single TR of the MSE sequence. T_1 = 3.05 s was used in all simulations, which is the measured T_1 of PCr in the heart at 7 T.[55] Simulations were performed over a range of T_2 values from 0 to 600 ms. The effects of field inhomogeneities that lead to short T_2* at 7 T were simulated by averaging over 1000 isochromats with a normal distribution of B_0 offsets with a standard deviation of 25 Hz.

SNR enhancement

Figure 8.1 shows the predicted SNR enhancement with 'perfect' pulses – i.e. ones that are infinitely short and achieve perfect excitation and refocusing. To predict the potential SNR enhancement of the MSE sequence more accurately, I simulated a TI with eight echoes for a range of T_2 values. The TR of the MSE CSI sequence is 5 seconds – I compared this to a pulse acquire sequence with TR= 1 s, under steady state conditions at the Ernst angle. The simulation ignored any B_1^+ variation, and assumes the experiment is perfectly on-resonance. For a fair comparison, the total scan time of the sequences were matched.

T_2 measurement

To assess the optimum number of echoes for accurate T_2 measurement, I performed Monte Carlo simulations to fit T_2 at a range of SNR levels. I also calculated the minimum TI required for each number of echoes, according to the 10s SAR limit. The calculation was performed with the pulses at a voltage of 449V (which corresponds to a peak B_{1+} of approximately 16.5 µT at the depth of the heart).

Finally, I explored the impact of variation in B_{1+} by further Monte Carlo analysis. The effect of error in B_{1+} ranging from 10 – 20 µT was simulated over the range of ^{31}P T_2 values measured in other organs at 7 T (Table 8.2). In these simulations, SNR (the maximum of peak divided by SD of real part of baseline) was set to 20.

8.5.1.2 Results

SNR enhancement

Figure 8.10 shows the simulated SNR enhancement from combining FID and echo signals, compared to a pulse acquire sequence with the same TR (5 s). Unlike Figure 8.1, where combining signals is beneficial for all T_2 values, using real pulse shapes means that – from an SNR perspective – combining signals is only worthwhile at T_2 values of ~70 ms and above. At T_2 < 70ms, the additional noise from the extra echoes outweighs the benefit of the increased signal afforded by combining them with the FID.

Furthermore, when compared to a steady-state pulse acquire sequence with TR = 1 s run at the Ernst angle (black dashed line), the relative SNR of the MSE sequence is further reduced. In this case, the SNR of MSE sequence is only greater than a pulse-acquire approach for T2 value > 200 ms.

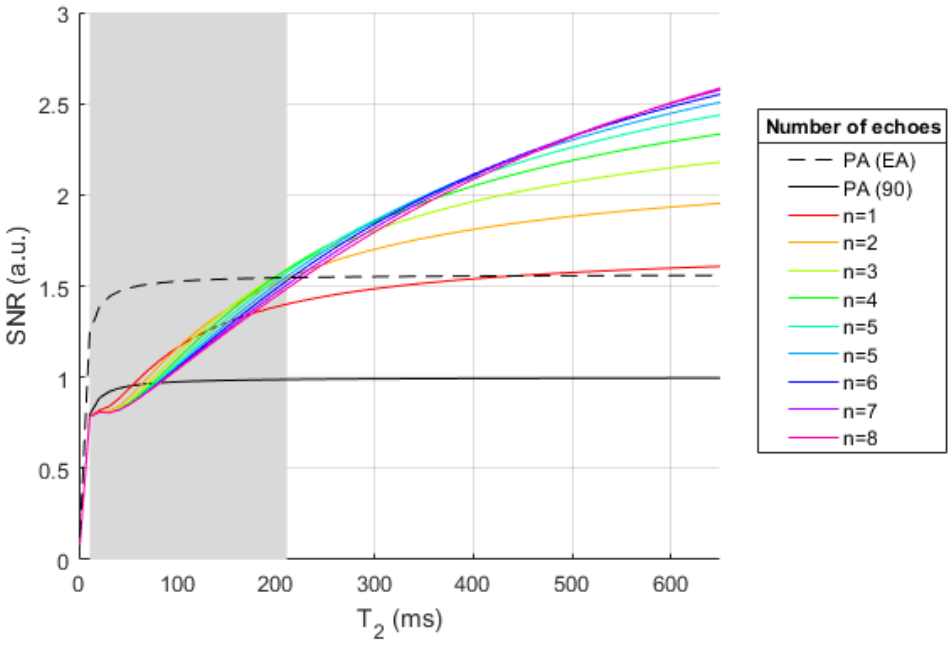


Figure 8.10 Simulated SNR enhancement using the COMP-SINC refocusing pulse in a multi echo sequence with a ΔTE = 45ms, TR=5s. Black dotted line marks SNR from a pulse acquire sequence run at the Ernst angle with a TR=1s. Grey shaded region mark the range of T_2 values of ^{31}P metabolites in other organs at 7 T reported in the literature.

T_2 measurements

For each number of refocusing pulses, Figure 8.11 A shows the minimum TI dictated by the 10 second SAR limit. With six echoes or less, TI can be kept to 1 second, enabling an effective TR = 5 s for 5 interleaves to catch the major ^{31}P metabolites or TR = 2s for PCr and gATP alone. Figure 8.11 B-D shows the results of Monte Carlo analysis evaluating the effect of the number of echoes on the accuracy and precision of T_2 measurements. As expected, both the accuracy and precision of the T_2 fits increase with improved SNR. Deciding upon the number of echoes is a balance – for longer T_2 values (200ms), a larger number of echoes improves the precision of T_2 measurement. However, at shorter T_2 values, increasing the number of echoes actually decreases the precision of T_2 fitting: the signal has decayed by the later echoes, so sampling more points further along the T_2 curve is essentially just adding noise.

Six echoes is a good compromise – there is minimal improvement in precision beyond six echoes when T_2 is long, and fitting still performs adequately at shorter T_2 values. This number of echoes also allows 1s TI.

Figure 8.12 shows the accuracy and precision of T_2 fitting for a six echo sequence for a range of B_1^+. At $T_2 < 20$ ms, T_2 fitting fails. For $T_2 > 50$ ms and $12 < B_{1+} < 20$ μT, the mean error in T_2 measurements are <10%, with a CV between 15-20%.

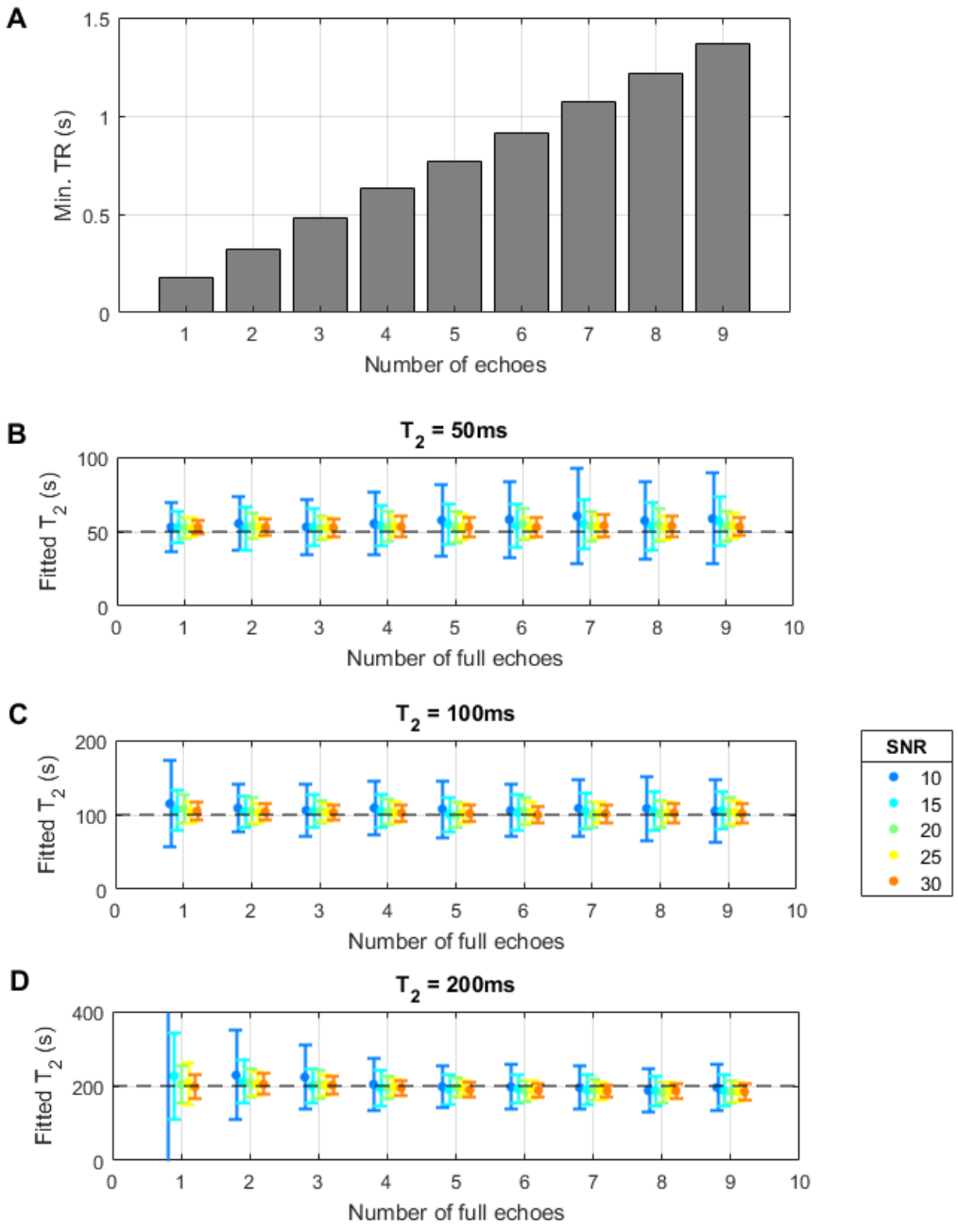


Figure 8.11 A Number of echoes vs. corresponding minimum TI to comply with 10 s SAR limitations. **B-D** Number of echoes vs. fitted T_2 at a range of SNRs. Actual T_2 values were 50ms (**B**), 100ms (**C**), and 200ms (**D**). Error bars mark ±1 SD.

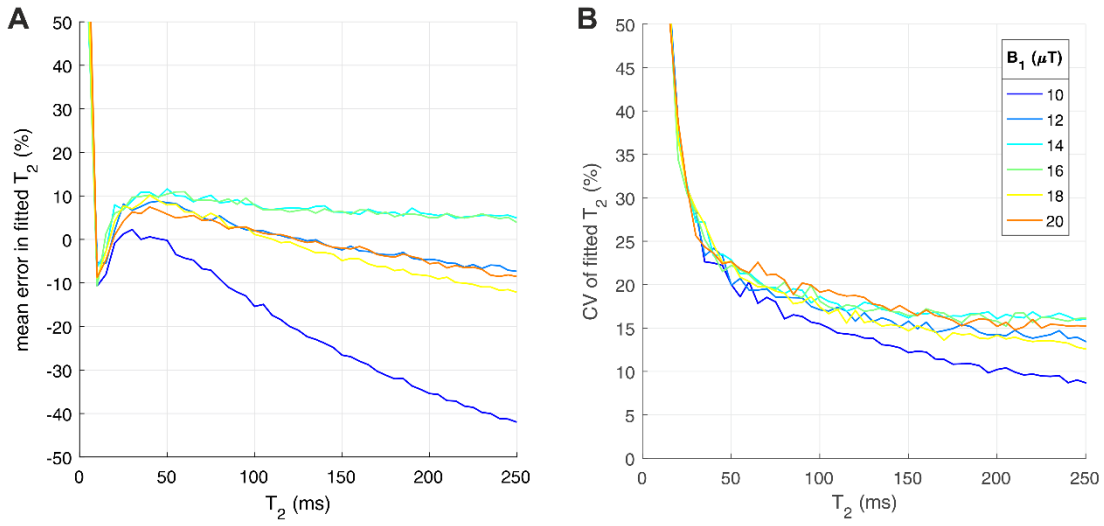


Figure 8.12 A Accuracy and **B** precision of Monte-Carlo T_2 fitting at a range of B_1^+. Coefficient of variation, CV calculated as $\frac{SD}{mean} \times 100\%$.

8.5.2 Planned in vivo experiments

I have implemented the MSE sequence in IDEA, Siemens's pulse sequence programming environment (Appendix B). It is ready to be tested on the scanner once scanning can resume, which at the time of writing, is subject to COVID-19 restrictions. To give context to the significance of the work in this chapter, this section outlines the *in vivo* experiments that I had planned to perform.

Initially, I had planned to run scans without interleaving acquisitions centred on different metabolites. This would allow the performance of the sequence to be tested whilst the off-resonance behaviour of the pulses could be ignored. After performing this proof-of-concept I then planned to re-run the scans using the interleaving. This approach would have allowed the impact of interleaving to quantitatively assessed.

Skeletal muscle validation

^{31}P metabolite T_2 values have been measured in the human calf at 7 T.[170] I would have validated the T_2 values measured by my MSE sequence by scanning the calf muscle of 3 healthy volunteers and comparing the measured T_2 values to literature values. I would have expected to see PCr $T_2 \approx 217$ ms, Pi $T_2 \approx 109$ ms and PDE $T_2 \approx 314$ ms.

I would also test the effect of reducing the peak B_1^+ in skeletal muscle to see whether values are still robust at the cardiac B_1^+ of 16.5μT.

Cardiac T_2 measurements in healthy volunteers

I had planned to perform cardiac scans in 10 healthy volunteers. I expected to validate the results of the SNR simulations and, report ^{31}P T_2 values in the human heart at 7 T.

8.6 Discussion

8.6.1 Refocusing pulse

Simulation results suggest that selective COMP-SINC pulse is able to selectively refocus spins over a range of B_{1+} values at a peak B_{1+} = 16.5μT. Once tested *in vivo,* this will be the first implementation of a composite pulse in the heart at 7 T.

The simulated performance of selective OPT-CONTROL pulse is similar to the COMP-SINC but was not chosen due to its high SAR deposition; SAR performance could be improved by including a SAR constraint in the optimisation.[171] The frequent, large, changes in the pulse's phase might also mean that the RF amplifier is unable to play out the pulse waveform with complete fidelity, increasing the discrepancy between simulation and *in vivo* results.

A broadband pulse would have been desirable as not having to repeat the experiment at differing frequency offsets would reduce the acquisition time. Sadly, the relatively low B_{1+} of 16.5μT meant that the design of an effective broadband refocusing pulse proved infeasible. However, if one could increase the peak B_1^+ to 30μT a pulse with a bandwidth high enough to simultaneously refocus two metabolites could well be possible and would reduce the required number of interleaves from five to three. The extra B_1^+ could also be used to shorten the refocusing pulse, thus making shorter echo times possible. Our group have been developing a whole-body solution for ^{31}P-MRS for a few years. *In vivo* data from a prototype of this "^{31}P body coil" suggest that B_1^+ = 30μT may be achievable for cardiac ^{31}P-MRS in future.[172] Furthermore, the body coil had a more favourable k-factor (less sample heating per "unit" of

B_1^+) – this might allow the sequence to be run at a shorter TI (or TR), further boosting SNR per unit time.

The limitations of broadband pulse design highlight a technical challenge of performing experiments at ultra-high field strengths: in this work, at 7 T, a refocusing pulse covering 16ppm equates to a bandwidth of ~2000Hz. A 16ppm pulse at 3 T would correspond to a bandwidth of just 830 Hz. Combined with the lower B_{1+} available at 7 T, broadband pulses are therefore much more difficult to achieve at 7 T. Improving the B_1^+ achievable in the body at 7 T and minimising the corresponding SAR dose are topics of active ongoing research.

8.6.2 MSE sequence

The acquisition time of the proposed sequence protocol is 33 minutes. Once time spent localising and shimming is taken into account, the total scan time will be similar to the 28 min UTE-CSI tested in Chapter 5; a scan time which is feasible for clinical research.

Simulations show that both the potential SNR enhancement offered by the MSE CSI and the accuracy and precision of T_2 measurements depend critically on the range of T_2 values expected in vivo in the target organ. While we wait for our first measurements of cardiac T_2 values, it is instructive to consider values that have been measured in other organs (Table 8.2). Figure 8.13 highlights the field strength dependence of measured T_2 values. There is a trend for decreasing ^{31}P T_2 values at higher field strengths, which can be explained by the increasing efficiency of T_2 relaxation mechanisms (such as chemical shift anisotropy) at higher field strengths.[173] At 7 T, reported T_2 values range is from 19 – 217 ms in the human body.

8.6.2.1 SNR

Literature values suggest that cardiac ^{31}P T_2 values (other than perhaps PCr) are likely too short for the interleaved MSE-CSI sequence to improve SNR when compared to a pulse-acquire UTE-CSI sequence with matched total acquisition time and an optimised (shorter) TR compared to the MSE-CSI.

The necessity to increase the TR is the biggest (experimentally controllable) factor that hinders the potential SNR enhancement of the MSE.

If under fully relaxed conditions, increasing the TR from 1 to 5 seconds reduces the SNR per unit time by a factor of $\sqrt{5} \approx 2.2$. In practice, the SNR penalty of the 5 s TR will be less than this: experiments are run under steady state conditions, so acquisitions at shorter TRs will contribute less signal per transient. In fact, one benefit of the interleaved acquisition is that it would be possible to set metabolite-specific excitation flip angles to achieve the Ernst angle for each metabolite (computed from the metabolite T_1).

Table 8.2 Papers reporting attempts to measure T_2 values of ^{31}P metabolites in humans. Grey shaded cells indicate where a multi-echo sequence has been used to acquire data.

				T2 (ms)								
Ref	**n**	**B_0/ T**	**Organ**	**Pi**	**PDE**	**PCR**	**γ-ATP**	**αATP**	**βATP**	**PE**	**PC**	**GPC**
[170]	8	3	Calf muscle	153±9	414±128	354±16	-	-	-	-	-	-
[170]	8	7	Calf muscle	109±17	314±35	217±14	-	-	-	-	-	-
[18]	6	3	Calf muscle	148±17	-	334±30	-	-	-	-	-	-
[174]	6	1.5	Calf muscle	205±14	-	424±21	16±5	22±6	8±2	-	-	-
[175]	12	1.5	Calf muscle	-	-	-	89±9	84±6	62±3	-	-	-
[176]	16	1.5	Calf muscle	-	-	-	-	-	-	-	-	-
[176]	16	1.5	Calf muscle	-	-	-	95	74	75	-	-	-
[177]	3	9.4	Calf muscle	85±5	220±14	158±8	18.5±1.3	13.4±5.1	-	-	-	-
[19]		2	Brain	80	20	150	30	30	-	-	-	-
[178]	10	1.5	Brain	-	-	-	89±9	84±6	62±3	-	-	-
[179]	1	7	Brain	-	-	-	-	21.4±3.3	-	-	-	-
[180]	6	7	Brain	-	-	132±12.8	26.1±9.6	25.8±6.6	-	-	-	-
[161]	9	7	Brain	86±2	-	-	-	-	-	202±6	129±6	213±11
[157]	10	7	Liver	46.4±1.1	-	-	-	18.2±0.4	-	-	51.2±2.3	50.4±0.8

[181]	8	7	Breast	180 ± 4	-	-	19 ± 3	-	-	199 ± 8	239 ± 14	177 ± 6
[182]		7	Breast	-	-	-	-	-	-	-	-	-
[158]	5	7	Breast	189	-	-	-	-	-	155	174	24
[183]	7	7	Breast	188	-	-	-	-	-	154	173	23
[6]		7	Heart	-	-	220±195	105±127	14±4	70±140	-	-	-
[184]	5	9.4	Brain	43 ± 9	-	99 ± 4	31 ± 6	41 ± 5	-	98 ± 16	108 ± 22	110 ± 11

[a] Data extracted from figure in paper using WebPlotDigitizer, https://automeris.io/WebPlotDigitizer/

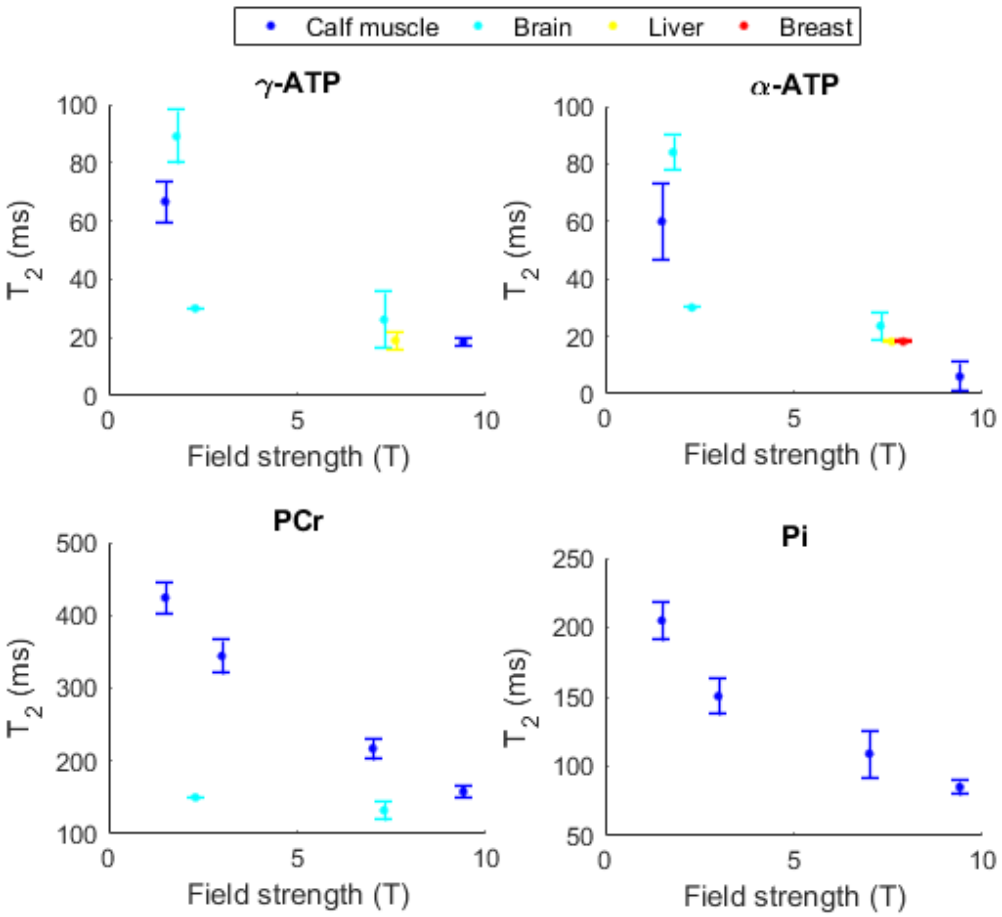


Figure 8.13 Variation of T_2 with field strength. Mean±SD of literature T_2 values presented in Table 1. Where more than one value was available at a single field strength the mean was taken, and the SD is the mean of the individual SDs.

8.6.2.2 T_2 measurement

Monte Carlo analysis suggests that between 12 μT < B_{1+} < 20μT, the MSE CSI will be able to measure T_2 values to a precision of ±10% over the range of T_2 values expected from the literature.

Figure 8.11 suggests that precision could be improved by including fewer echoes in the analysis. Simulations in Figure 8.12 assumed a FID spectrum SNR of 20. This value was chosen as it was the average SNR of the PCr peak obtained from the 6½ minute scan in Chapter 6, from which the scan parameters for the proposed MSE CSI protocol are based on. In reality, it is expected that SNR from the 33 minute MSE CSI should be higher than that of the 6½ UTE CSI – although both protocols are 'matched' in terms of number of

averages and voxel size, the higher excitation flip angle for the 5s TR in the MSE CSI will mean that more signal will be contributed by each TR.

It is worth noting that the T_2 values of α-, β- and γ-ATP will be likely underestimated due to the homonuclear ^{31}P scalar (J) coupling. The full effect of this may be hard to quantify because the other ATP spins will not be refocused by the frequency-selective refocusing pulse.

The UTE-CSI acquisitions from previous chapters have employed saturation bands to suppress signal in the chest wall and reduce contamination. The addition of refocusing pulses in the MSE CSI sequence mean that it is unlikely that there would be sufficient SAR "budget" for saturation bands. However, any skeletal muscle contamination present in the ^{31}P-MRS spectrum is more likely to affect PCr/ATP than T_2 measurements; PCr/ATP in skeletal muscle is approximately 4 times that of cardiac tissue (section 3.3.3) – it would be surprising if T_2 varied by this much. Nevertheless, any contamination is still undesirable. It may therefore prove worthwhile to reduce the number of echoes in the sequence, to "free-up" some of the SAR budget for saturation bands. Alternatively, we may discover that the MSE CSI is inherently more resistant to signal contamination because B_1^+ in skeletal muscle is likely to be far from the optimum for echo generation so the MSE CSI sequence could show an inbuilt suppression of skeletal muscle signal. Or finally, we could repeat these scans using the meander coil concept for local gradient based suppression of skeletal muscle signal without the SAR budget needed for saturation bands.

Validating the sequence by scanning human calf muscle will be an important next step. If T_2 values measured by the MSE CSI sequence in the calf are consistent with literature values, confidence in any measured cardiac T_2 values will be greatly increased. One possible extension to the proposed *in vivo* experiments would be to also implement the sequence at 3 T. Human cardiac ^{31}P T_2 values have not yet been measured at 3 T and

doing so would also contribute understanding the field strength dependence of transverse relaxation times.

8.7 Conclusions

I have presented a novel MSE CSI sequence for ^{31}P-MRS at 7 T where consideration was paid to the design of a refocusing pulse that offers a degree of B_{1+} insensitivity at a low peak B_{1+}. Simulations predict the sequence will be able to measure T_2 to with ±10%. While the closure of University buildings meant that it was not possible to test the sequence on the scanner, it has been implemented in IDEA ready for testing once scanning can resume – there are plans for this to happen in Spring 2021. The work in this chapter has laid the foundations for being able to measure ^{31}P T_2 values in the human heart for the first time.

Appendix B

8.9 Appendix B Sequence implementations in IDEA

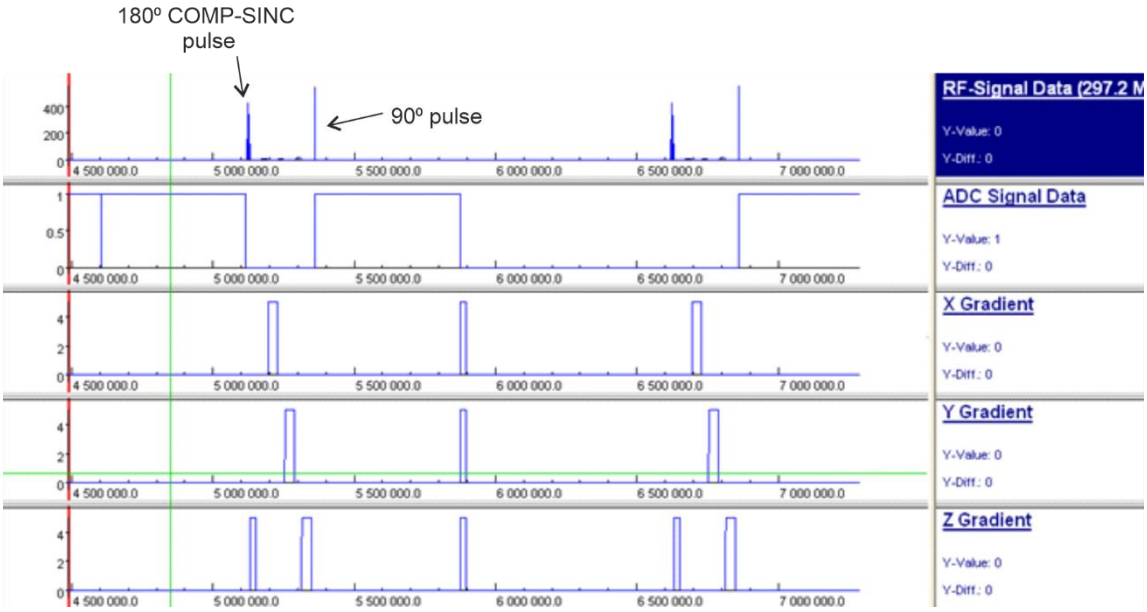


Figure 8.14 Screenshot of modified IR-FID sequence for phantom validation scans. The refocusing pulse of interest is followed by a 90º excitation pulse. This example features the selective COMP-SINC pulse

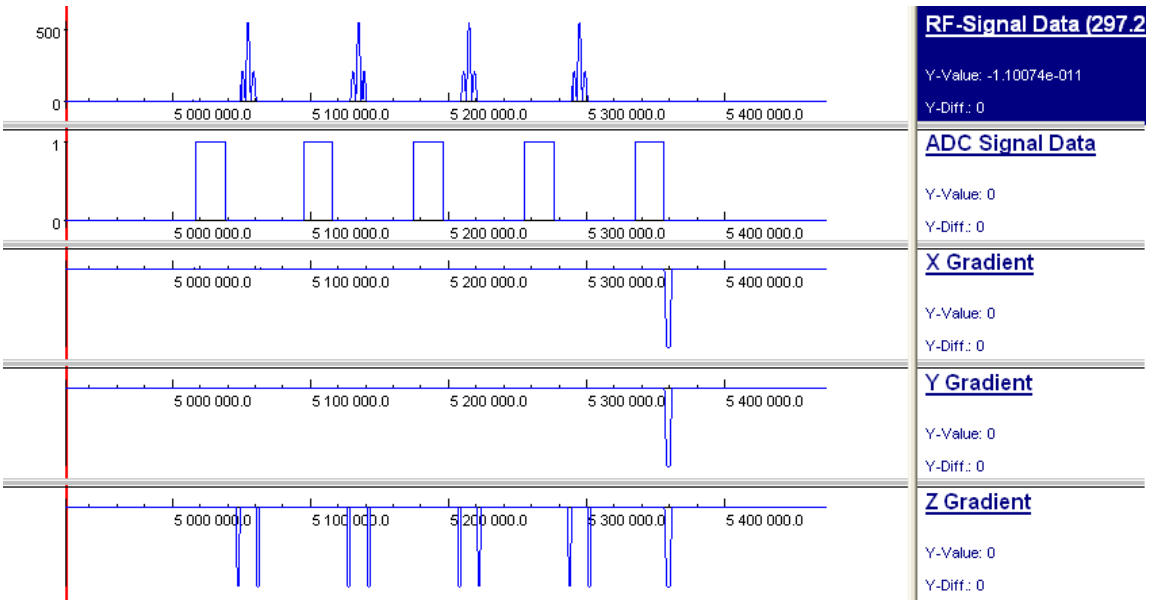


Figure 8.15 Screenshot of a single TI from the MSE CSI sequence using the selective COMP-SINC refocusing pulse.

9 Conclusion and future work

The overall aims of this work were to quantify the benefits of the improved SNR available by scanning at 7 T and develop a multi-echo CSI sequence that could be used to measure human cardiac ^{31}P T_2 values for the first time. Development of the multi-echo sequence also had the complementary aim of improving SNR by combining FID and echo data. In this chapter I summarise the contributions of this thesis and suggest some possible future directions for research.

9.1 Improved reproducibility of ^{31}P-MRS at 7 T

9.1.1 Specific achievements

The first aim of this thesis was to quantify how the improved SNR and precision at 7 T would affect future studies measuring PCr/ATP in the human heart. I assessed the reproducibility of an existing, 28 minute UTE-CSI sequence (Chapter 5) and demonstrated that the high SNR achievable at 7 T translates into more reproducible PCr/ATP measurements than those reported at lower field strengths.[62] This represents an important contribution as these reproducibility statistics will be used to perform power calculations for future studies. I illustrated how ^{31}P-MRS studies performed at 7 T will require much smaller cohorts to those performed at lower field strengths, saving both research time and study costs.

I also developed a shorter, 6½ minute, UTE-CSI protocol, which I showed to have equivalent reproducibility to a scan that takes 30 minutes 3 T. The results of the work in Chapters 5 and 6 are summarised in the publication:

Ellis, J., et al. 2019. Reproducibility of human cardiac phosphorus MRS (^{31}P-MRS) at 7 T. ***NMR Biomed****. 32, e4095; doi: 10.1002/nbm.4095.*

The 6½ minute scan is short enough to allow multiple PCr/ATP measurements at differing steady states within a single scanning slot. This has already been demonstrated in the work in Chapter 7, where I investigated the effect of a ketone drink on cardiac energetics. 6½ minutes is also within the British Society of Echocardiography's recommendations for a dobutamine protocol for assessment of myocardial ischemia:[132] the 6½ minute scan could therefore be used for rest, stress and recovery assessments of cardiac PCr/ATP under pharmacologically induced stress.

9.1.2 Extensions and potential improvements

A proof-of concept study of whole-body ^{31}P transmit coil,[135] with a 35 kW ^{31}P RF amplifier and a 30-element receive array has been published.[172] This is a study for which I am a co-author. The coil can achieve adiabatic excitation across the heart, so that there is a uniform excitation flip angle in all cardiac voxels. It could well be the case that the uniform excitation provided by a ^{31}P body coil makes combining signal from multiple voxels a viable option for further increasing reproducibility.

Results were analysed in terms of the PCr/ATP ratio. The PCr/ATP is the most commonly measured parameter in cardiac ^{31}P-MRS, meaning that it was easier to compare our results to those measured at other field strengths. However, the PCr/ATP ratio is typically used under the assumption that [PCr] changes while [ATP] remains constant. This assumption is reasonable in the healthy heart, but at high workloads as well as later stages of heart failure [ATP] decreases and so using the PCr/ATP ratio may obscure changes in ATP concentration.[5] Using 7 T, many more possibilities are opened for pulse sequence development to probe cardiac energy metabolism in greater depth and are likely to be a key focus of future technical development.[47,106,185]

The exclusion criteria for scanning at 7 T is currently more extensive than those at lower field strengths. This is in large part because few implants or surgical devices have yet been approved by manufacturers as safe at 7 T; this situation is expected to improve in the next few years with the growing popularity of 7 T scanners.

Finally, scan times could be reduced further by utilising different k-space sampling trajectories. For example, a 7 T 3D CONCEPT sequence, in which k-space is sampled using a density weighted concentric ring trajectory has recently been shown by our group to be able to measure cardiac PCr/ATP in just 2½ minutes, over 2.5 x faster than a matched sequence using traditional acquisition weighting.[186]

9.2 A multi-echo sequence for ^{31}P-MRS at 7 T

9.2.1 Specific achievements

Simulations suggest that the MSE CSI sequence I developed will be able to measure T_2 values to within an accuracy of ±10%. I overcame the limitations of a low, varying transmit field by designing a novel composite refocusing pulse. I was also able to answer whether a MSE CSI sequence is a viable option for SNR improvement – the answer being no, or at least not with currently available hardware.

It was sadly not possible to validate the designed pulse in a phantom experiment because of ongoing scanning restrictions due to the COVID-19 pandemic. Nonetheless, the simulation and optimisation framework that I developed will be useful to future studies requiring pulse design. When it is possible to test the proposed sequence *in vivo*, measuring cardiac T_2 values at 7 T will constitute a novel finding.

9.2.2 Extensions and potential improvements

The design of a broadband refocusing pulse was limited by the relatively low peak B_1^+ of the available coils. Fortunately, the proof-of concept study of a whole-body ^{31}P transmit coil powered by a 35 kW amplifier, was able to achieve a peak B_1^+ at the depth of the heart of almost double that achieved by any of the coils currently available for 7 T ^{31}P

scanning in Oxford.[172] There are plans to test my proposed approach in spring 2021 in the Rodgers' group in Cambridge as part of an EU Future and Emerging Technologies project. The group are currently performing pilot scans on a ^{31}P dipole coil that has performance similar to that of the proof-of-concept body coil – it may be that this improved hardware makes SNR improvement by an MSE approach a viable option in the heart. Furthermore, an updated coil will be installed in Oxford next year. It will be interesting to see the pulse designs that are possible with this new hardware.

One possible extension to the proposed *in vivo* experiments would be to also implement the sequence at 3 T. Human cardiac ^{31}P T_2 values have not yet been measured at 3 T and doing so would also contribute understanding the field strength dependence of transverse relaxation times.

Transverse relaxation times tell us about the chemical environment of metabolites; lower ^{31}P T_2 values have been observed in tumour tissue of breast cancer patients.[158] It is therefore possible that cardiac ^{31}P T_2 values differ between healthy and failing myocardium. Measuring cardiac ^{31}P T_2 values in a cohort of heart failure patients could be considered as another possible extension.

Finally, if cardiac T_2 values differ markedly between metabolites – e.g. DPG and Pi, or α-ATP and NAD/NADH – then a T_2 selective sequence (e.g. dual inversion) may be useful to probe these important, but relatively small, peaks more effectively.

References

1. Roger, V. L. *et al.* Heart disease and stroke statistics-2012 update: A report from the American heart association. *Circulation* **125**, e2 (2012).

2. Levy, D. *et al.* Long-Term Trends in the Incidence of and Survival with Heart Failure. *N. Engl. J. Med.* **347**, 1397–1402 (2002).

3. Sutherland, K. *Identify Innovate Demonstrate Encourage Bridging the quality gap: Heart failure*. (2010).

4. Bottomley, P. A., Bottomley & A., P. MRS Studies of Creatine Kinase Metabolism in Human Heart. in *eMagRes* 1183–1202 (John Wiley & Sons, Ltd, 2016). doi:10.1002/9780470034590.emrstm1488.

5. Neubauer, S. The Failing Heart — An Engine Out of Fuel. *N. Engl. J. Med.* **356**, 1140–1151 (2007).

6. Rodgers, C. T. *et al.* Human cardiac ^{31} P magnetic resonance spectroscopy at 7 tesla. *Magn. Reson. Med.* **72**, 304–315 (2014).

7. de Graaf, R. A. *In vivo NMR spectroscopy: principles and techniques*. (John Wiley & Sons, Inc., 2007).

8. Haacke, E. *Magnetic resonance imaging : physical principles and sequence design*. (Wiley-Liss, 1999).

9. Bernstein MA, King KF, Z. Z. *Handbook of MRI pulse sequences*. (Academic Press, 2004).

10. Bottomley, P. A. Turning Up the Heat on MRI. *J. Am. Coll. Radiol.* **5**, 853–855 (2008).

11. Bottomley, P. A., Foster, T. B. & Darrow, R. D. Depth-resolved surface-coil spectroscopy (DRESS) for in Vivo1H, 31P, and 13C NMR. *J. Magn. Reson.* **59**, 338–342 (1984).

12. Brown, T. R., Kincaid, B. M. & Ugurbil, K. NMR chemical shift imaging in three dimensions. *Proc. Natl. Acad. Sci. U. S. A.* **79**, 3523–3526 (1982).

13. Mareci, T. H. & Brooker, H. R. High-resolution magnetic resonance spectra from a sensitive region defined with pulsed field gradients. *J. Magn. Reson.* **57**, 157–163 (1984).

14. Garwood, M., Schleich, T., Robin Bendall, M. & Pegg, D. T. Improved fourier series windows for localization in in vivo NMR spectroscopy. *J. Magn. Reson.* **65**, 510–515 (1985).

15. Hu, X., Levin, D. N., Lauterbur, P. C. & Spraggins, T. SLIM: Spectral localization by imaging. *Magn. Reson. Med.* **8**, 314–322 (1988).

16. Zhang, Y., Gabr, R. E., Schär, M., Weiss, R. G. & Bottomley, P. A. Magnetic resonance Spectroscopy with Linear Algebraic Modeling (SLAM) for higher speed

and sensitivity. *J. Magn. Reson.* **218**, 66–76 (2012).

17. von Kienlin, M. *et al.* Advances in human cardiac ^{31} P-MR spectroscopy: SLOOP and clinical applications. *J. Magn. Reson. Imaging* **13**, 521–527 (2001).

18. Meyerspeer, M., Kr??&#65533;k, M. & Moser, E. Relaxation times of31P-metabolites in human calf muscle at 3 T. *Magn. Reson. Med.* **49**, 620–625 (2003).

19. Merboldt, K. D. *et al. Imalized 31P NMR Spectroscopy of the Ad& Ikaiu in Viw Using Stimulated-Echo (STEAM) Ssequences*. *JOURNAL OF MAGNETIC RESONANCE* vol. 89 https://pure.mpg.de/rest/items/item_602921/component/file_2357825/content (1990).

20. Ziessow, D. R. R. Ernst, G. Bodenhausen u. A. Wokaun: *Principles of Nuclear Magnetic Resonance in One and Two Dimensions* , Clarendon Press, Oxford 1987. 610 Seiten. *Berichte der Bunsengesellschaft für Phys. Chemie* **92**, 1563–1565 (1988).

21. Kreis, R. Issues of spectral quality in clinical 1 H-magnetic resonance spectroscopy and a gallery of artifacts. *NMR Biomed. NMR Biomed* **17**, 361–381 (2004).

22. Bottomley, P. A. NMR Spectroscopy of the Human Heart. in *eMagRes* (John Wiley & Sons, Ltd, 1996). doi:10.1002/9780470034590.emrstm0345.pub2.

23. Hyde, J. S. *et al.* Parallel image acquisition from noninteracting local coils. *J. Magn. Reson.* **70**, 512–517 (1986).

24. Roemer, P. B., Edelstein, W. A., Hayes, C. E., Souza, S. P. & Mueller, O. M. The NMR phased array. *Magn. Reson. Med.* **16**, 192–225 (1990).

25. Ernst, R. R. & Anderson, W. A. Application of Fourier Transform Spectroscopy to Magnetic Resonance. *Rev. Sci. Instrum.* **37**, 93–102 (1966).

26. Neubauer, S. The failing heart--an engine out of fuel. *N. Engl. J. Med.* **356**, 1140–51 (2007).

27. Taegtmeyer, H. Cardiac metabolism as a target for the treatment of heart failure. *Circulation* vol. 110 894–896 (2004).

28. Depre, C., Vanoverschelde, J.-L. J. & Taegtmeyer, H. Glucose for the Heart. *Circulation* **99**, 578–588 (1999).

29. Doenst, T., Nguyen, T. D. & Abel, E. D. Cardiac metabolism in heart failure: Implications beyond atp production. *Circ. Res.* **113**, 709–724 (2013).

30. Gibbs, C. L. Cardiac energetics. *Physiological Reviews* vol. 58 174–254 (1978).

31. Suga, H. Ventricular energetics. *Physiological Reviews* vol. 70 247–277 (1990).

32. Bessman, S. & Geiger, P. Transport of energy in muscle: the phosphorylcreatine shuttle. *Science (80-.).* **211**, 448–452 (1981).

33. Katz, A. M. Is the failing heart energy depleted? *Cardiol. Clin.* **16**, 633–644 (1998).

34. Glancy, B. *et al.* Mitochondrial reticulum for cellular energy distribution in muscle.

Nature **523**, 617–620 (2015).

35. BUNDKIRCHEN, A. Epidemiology and economic burden of chronic heart failure. *Eur. Hear. J. Suppl.* **6**, D57–D60 (2004).

36. Bui, A. L., Horwich, T. B. & Fonarow, G. C. Epidemiology and risk profile of heart failure. *Nature Reviews Cardiology* vol. 8 30–41 (2011).

37. Francone, M., Borasi, G., Hyafil, F. & Souftas, V. D. Role of Cardiac Magnetic Resonance in the Evaluation of Dilated Cardiomyopathy: Diagnostic Contribution and Prognostic Significance. (2014) doi:10.1155/2014/365404.

38. Richardson, P. *et al.* Report of the 1995 World Health Organization/International Society and Federation of Cardiology Task Force on the Definition and Classification of Cardiomyopathies. *Circulation* **93**, 841–842 (1996).

39. Wight, J. N. & Salem, D. Sudden Cardiac Death and the 'Athlete's Heart'. *Arch. Intern. Med.* **155**, 1473–1480 (1995).

40. Firoozi, S., Sharma, S. & McKenna, W. J. Risk of competitive sport in young athletes with heart disease. *Heart* vol. 89 710–714 (2003).

41. Dei Cas, A. *et al.* Impact of diabetes on epidemiology, treatment, and outcomes of patients with heart failure. *JACC: Heart Failure* vol. 3 136–145 (2015).

42. Levelt, E. *et al.* Relationship between left ventricular structural and metabolic remodeling in type 2 diabetes. *Diabetes* **65**, 44–52 (2016).

43. Lopatin, Y. Metabolic Therapy in Heart Failure. *Card. Fail. Rev.* **1**, 112 (2015).

44. Milinković, I., Rosano, G., Lopatin, Y. & Seferović, P. M. The Role of Ivabradine and Trimetazidine in the New ESC HF Guidelins. *Card. Fail. Rev.* **2**, 123 (2016).

45. Noordali, H., Loudon, B. L., Frenneaux, M. P. & Madhani, M. Cardiac metabolism — A promising therapeutic target for heart failure. *Pharmacology and Therapeutics* vol. 182 95–114 (2018).

46. Kemp, G. J., Meyerspeer, M. & Moser, E. Absolute quantification of phosphorus metabolite concentrations in human muscle in vivo by 31P MRS: a quantitative review. *NMR Biomed.* **20**, 555–65 (2007).

47. Clarke, W. T., Robson, M. D., Neubauer, S. & Rodgers, C. T. Creatine kinase rate constant in the human heart measured with 3D-localization at 7 tesla. *Magn. Reson. Med.* **78**, 20–32 (2017).

48. Valkovič, L. *et al.* Adiabatic excitation for ^{31}P MR spectroscopy in the human heart at 7 T: A feasibility study. *Magn. Reson. Med.* (2016) doi:10.1002/mrm.26576.

49. Stoll, V. M. *et al.* Dilated Cardiomyopathy: Phosphorus 31 MR Spectroscopy at 7 T. *Radiology* **281**, 409–417 (2016).

50. Bashir, A. & Gropler, R. Reproducibility of creatine kinase reaction kinetics in human heart: a 31P time-dependent saturation transfer spectroscopy study. *NMR Biomed.* **27**, 663–671 (2014).

51. Bottomley, P. A. & Ouwerkerk, R. Optimum flip-angles for exciting NMR with

uncertainT1 values. *Magn. Reson. Med.* **32**, 137–141 (1994).

52. El-Sharkawy, A. E. M., Schar, M., Ouwerkerk, R., Weiss, R. G. & Bottomley, P. A. Quantitative cardiac 31P spectroscopy at 3 Tesla using adiabatic pulses. *Magn. Reson. Med.* **61**, 785–795 (2009).

53. Horn, M. *et al.* 31P-NMR spectroscopy of human blood and serum: first results from volunteers and patients with congestive heart failure, diabetes mellitus and hyperlipidaemia. *MAGMA Magn. Reson. Mater. Physics, Biol. Med.* **1**, 55–60 (1993).

54. Tyler, D. J., Hudsmith, L. E., Clarke, K., Neubauer, S. & Robson, M. D. A comparison of cardiac ^{31} P MRS at 1.5 and 3 T. *NMR Biomed.* **21**, 793–798 (2008).

55. Rodgers, C. T. *et al.* Human cardiac 31P magnetic resonance spectroscopy at 7 tesla. *Magn. Reson. Med.* **72**, 304–315 (2014).

56. Bottomley, P. A. Noninvasive study of high-energy phosphate metabolism in human heart by depth-resolved 31P NMR spectroscopy. *Science (80-.).* **229**, 769–772 (1985).

57. Löffler, R., Sauter, R., Kolem, H., Haase, A. & Von Kienlin, M. Localized Spectroscopy from Anatomically Matched Compartments: Improved Sensitivity and Localization for Cardiac 31P MRS in Humans. *J. Magn. Reson.* **134**, 287–299 (1998).

58. Smith, C. S., Bottomley, P. A., Schulman, S. P., Gerstenblith, G. & Weiss, R. G. Altered creatine kinase adenosine triphosphate kinetics in failing hypertrophied human myocardium. *Circulation* **114**, 1151–1158 (2006).

59. Weiss, R. G., Bottomley, P. A., Hardy, C. J. & Gerstenblith, G. Regional Myocardial Metabolism of High-Energy Phosphates during Isometric Exercise in Patients with Coronary Artery Disease. *N. Engl. J. Med.* **323**, 1593–1600 (1990).

60. Beer, M. *et al. Absolute Concentrations of High-Energy Phosphate Metabolites in Normal, Hypertrophied, and Failing Human Myocardium Measured Noninvasively With 31 P-SLOOP Magnetic Resonance Spectroscopy*. *Journal of the American College of Cardiology* vol. 40 (2002).

61. Dass, S. *et al.* Exacerbation of cardiac energetic impairment during exercise in hypertrophic cardiomyopathy: a potential mechanism for diastolic dysfunction. *Eur. Heart J.* **36**, 1547–1554 (2015).

62. Tyler, D. J. *et al.* Reproducibility of ^{31} P cardiac magnetic resonance spectroscopy at 3 T. *NMR Biomed.* **22**, 405–413 (2009).

63. Neubauer, S. *et al.* 31P magnetic resonance spectroscopy in dilated cardiomyopathy and coronary artery disease. Altered cardiac high-energy phosphate metabolism in heart failure. *Circulation* **86**, (1992).

64. Neubauer, S. *et al.* Contributions of 31P-magnetic resonance spectroscopy to the understanding of dilated heart muscle disease. *Eur. Heart J.* **16 Suppl O**, 115–8 (1995).

65. Neubauer, S. *et al.* Myocardial Phosphocreatine-to-ATP Ratio Is a Predictor of

Mortality in Patients With Dilated Cardiomyopathy. *Circulation* **96**, 2190–2196 (1997).

66. Neubauer, S. *et al.* 31P magnetic resonance spectroscopy in dilated cardiomyopathy and coronary artery disease. Altered cardiac high-energy phosphate metabolism in heart failure. *Circulation* **86**, 1810–8 (1992).

67. Phan, T. T. *et al.* Heart Failure With Preserved Ejection Fraction Is Characterized by Dynamic Impairment of Active Relaxation and Contraction of the Left Ventricle on Exercise and Associated With Myocardial Energy Deficiency. *J. Am. Coll. Cardiol.* **54**, 402–409 (2009).

68. Fragasso, G. *et al.* Effects of metabolic modulation by trimetazidine on left ventricular function and phosphocreatine/adenosine triphosphate ratio in patients with heart failure. *Eur. Heart J.* **27**, 942–8 (2006).

69. Weiss, R. G., Bottomley, P. A., Hardy, C. J. & Gerstenblith, G. Regional Myocardial Metabolism of High-Energy Phosphates during Isometric Exercise in Patients with Coronary Artery Disease. *N. Engl. J. Med.* **323**, 1593–1600 (1990).

70. Yabe, T. *et al.* Detection of myocardial ischemia by 31P magnetic resonance spectroscopy during handgrip exercise. *Circulation* **89**, 1709–1716 (1994).

71. Hudsmith, L. E. *et al.* 31P cardiac magnetic resonance spectroscopy during leg exercise at 3 Tesla. *Int. J. Cardiovasc. Imaging* **25**, 819–826 (2009).

72. Schaefer, S. *et al.* Metabolic response of the human heart to inotropic stimulation: In vivo phosphorus-31 studies of normal and cardiomyopathic myocardium. *Magn. Reson. Med.* **25**, 260–272 (1992).

73. Rider, O. J. *et al.* Effects of Catecholamine Stress on Diastolic Function and Myocardial Energetics in Obesity. *Circulation* **125**, 1511–1519 (2012).

74. Lamb, H. J. *et al.* Metabolic Response of Normal Human Myocardium to High-Dose Atropine-Dobutamine Stress Studied by ^{31} P-MRS. *Circulation* **96**, 2969–2977 (1997).

75. Lamb, H. J. *et al.* Diastolic dysfunction in hypertensive heart disease is associated with altered myocardial metabolism. *Circulation* **99**, 2261–2267 (1999).

76. Köstler, H. *et al.* Age and gender dependence of human cardiac phosphorus metabolites determined by SLOOP31P MR spectroscopy. *Magn. Reson. Med.* **56**, 907–911 (2006).

77. Schocke, M. F. H. *et al.* Impact of aging on cardiac high-energy phosphate metabolism determined by phosphorus-31 2-dimensional chemical shift imaging (31P 2D CSI). *Magn. Reson. Imaging* **21**, 553–559 (2003).

78. Okada, M., Mitsunami, K., Inubushi, T. & Kinoshita, M. Influence of aging or left ventricular hypertrophy on the human heart: Contents of phosphorus metabolites measured by 31P MRS. *Magn. Reson. Med.* **39**, 772–782 (1998).

79. Perseghin, G. *et al.* Effect of the sporting discipline on the right and left ventricular morphology and function of elite male track runners: A magnetic resonance imaging and phosphorus 31 spectroscopy study. *Am. Heart J.* **154**, 937–942

(2007).

80. Perseghin, G. *et al.* Left ventricular function and energy metabolism in middle-aged men undergoing long-lasting sustained aerobic oxidative training. *Heart* **95**, 630–635 (2009).

81. Rider, O. J. *et al.* Effects of catecholamine stress on diastolic function and myocardial energetics in obesity. *Circulation* **125**, 1511–1519 (2012).

82. Bottomley, P. A., Herfkens, R. J., Smith, L. S. & Bashore, T. M. Altered phosphate metabolism in myocardial infarction: P-31 MR spectroscopy. *Radiology* **165**, 703–707 (1987).

83. Kalil-Filho, R. *et al.* Normal high energy phosphate ratios in 'stunned' human myocardium. *J. Am. Coll. Cardiol.* **30**, 1228–1232 (1997).

84. Hardy, C. J., Weiss, R. G., Bottomley, P. A. & Gerstenblith, G. Altered myocardial high-energy phosphate metabolites in patients with dilated cardiomyopathy. *Am. Heart J.* **122**, 795–801 (1991).

85. Auffermann, W. *et al.* Normal and diffusely abnormal myocardium in humans: Functional and metabolic characterization with P-31 MR spectroscopy and cine MR imaging. *Radiology* **179**, 253–259 (1991).

86. De Roos, A. *et al.* Cardiac metabolism in patients with dilated and hypertrophic cardio-myopathy: Assessment with proton-decoupled P-31 MR spectroscopy. *J. Magn. Reson. Imaging* **2**, 711–719 (1992).

87. Masuda, Y. *et al.* High-energy Phosphate Metabolism of the Myocardium in Normal Subjects Patients with Various Cardiomyopathies —The study using ECG gated MR spectroscopy with a localization technique. *Jpn. Circ. J.* **56**, 620–626 (1992).

88. Schaefer, S. *et al.* Metabolic response of the human heart to inotropic stimulation:In vivo phosphorus-31 studies of normal and cardiomyopathic myocardium. *Magn. Reson. Med.* **25**, 260–272 (1992).

89. Hansch, A. *et al.* Noninvasive measurements of cardiac high-energy phosphate metabolites in dilated cardiomyopathy by using 31P spectroscopic chemical shift imaging. *Eur. Radiol.* **15**, 319–323 (2005).

90. Scheuermann-Freestone, M. *et al.* Abnormal cardiac and skeletal muscle energy metabolism in patients with type 2 diabetes. *Circulation* **107**, 3040–6 (2003).

91. Diamant, M. *et al.* Diastolic dysfunction is associated with altered myocardial metabolism in asymptomatic normotensive patients with well-controlled type 2 diabetes mellitus. *J. Am. Coll. Cardiol.* **42**, 328–335 (2003).

92. Jung, W. I. *et al.* Differences in cardiac energetics between patients with familial and nonfamilial hypertrophic cardiomyopathy. *Circulation* vol. 101 (2000).

93. Jung, W. I. *et al.* 31P NMR spectroscopy detects metabolic abnormalities in asymptomatic patients with hypertrophic cardiomyopathy. *Circulation* **97**, 2536–42 (1998).

94. Neubauer, S. *et al.* Direct measurement of spin-lattice relaxation times of

Phosphorus Metabolites in Human Myocardium. *Magn. Reson. Med.* **26**, 300–307 (1992).

95. Esposito, A. *et al.* Impaired left ventricular energy metabolism in patients with hypertrophic cardiomyopathy is related to the extension of fibrosis at delayed gadolinium-enhanced magnetic resonance imaging. *Heart* **95**, 228–233 (2009).

96. Bottomley, P. A. *et al.* Metabolic rates of ATP transfer through creatine kinase (CK flux) predict clinical heart failure events and death. *Sci. Transl. Med.* **5**, (2013).

97. Beer, M. *et al.* Absolute concentrations of high-energy phosphate metabolites in normal, hypertrophied, and failing human myocardium measured noninvasively with 31P-SLOOP magnetic resonance spectroscopy. *J. Am. Coll. Cardiol.* **40**, 1267–1274 (2002).

98. Weiss, R. G., Gerstenblith, G. & Bottomley, P. A. ATP flux through creatine kinase in the normal, stressed, and failing human heart. *Proc. Natl. Acad. Sci.* **102**, 808–813 (2005).

99. Yabe, T., Mitsunami, K., Inubushi, T. & Kinoshita, M. Quantitative Measurements of Cardiac Phosphorus Metabolites in Coronary Artery Disease by 31P Magnetic Resonance Spectroscopy. *Circulation* **92**, (1995).

100. Bottomley, P. A. *et al.* Reduced myocardial creatine kinase flux in human myocardial infarction an in vivo phosphorus magnetic resonance spectroscopy study. *Circulation* **119**, 1918–1924 (2009).

101. Clarke, W. T. *et al.* Localized rest and stress human cardiac creatine kinase reaction kinetics at 3 T. *NMR Biomed.* **32**, (2019).

102. Schär, M., El-Sharkawy, A. M. M., Weiss, R. G. & Bottomley, P. A. Triple repetition time saturation transfer (TRiST) 31P spectroscopy for measuring human creatine kinase reaction kinetics. *Magn. Reson. Med.* **63**, 1493–1501 (2010).

103. Schär, M. *et al.* Two repetition time saturation transfer (TwiST) with spill-over correction to measure creatine kinase reaction rates in human hearts. *J. Cardiovasc. Magn. Reson.* **17**, 70 (2015).

104. Gabr, R. E. *et al.* Cardiac work is related to creatine kinase energy supply in human heart failure: A cardiovascular magnetic resonance spectroscopy study. *J. Cardiovasc. Magn. Reson.* **20**, 81 (2018).

105. Moon, R. B. & Richards, J. H. Determination of intracellular pH by 31P magnetic resonance. *J. Biol. Chem.* **248**, 7276–7278 (1973).

106. Valkovič, L. *et al.* Measuring inorganic phosphate and intracellular pH in the healthy and hypertrophic cardiomyopathy hearts by in vivo 7T 31P-cardiovascular magnetic resonance spectroscopy. *J. Cardiovasc. Magn. Reson.* **21**, 19 (2019).

107. Faller, K. M. E., Lygate, C. A., Neubauer, S. & Schneider, J. E. 1H-MR spectroscopy for analysis of cardiac lipid and creatine metabolism. in *Heart Failure Reviews* vol. 18 657–668 (2013).

108. Gibbs, C. The cytoplasmic phosphorylation potential. Its possible role in the control of myocardial respiration and cardiac contractility. *J. Mol. Cell. Cardiol.* **17**, 727–31

(1985).

109. Solaiyappan, M., Weiss, R. G. & Bottomley, P. A. Neural-network classification of cardiac disease from 31P cardiovascular magnetic resonance spectroscopy measures of creatine kinase energy metabolism. *J. Cardiovasc. Magn. Reson.* **21**, 49 (2019).

110. Kemp, G. J., Meyerspeer, M. & Moser, E. Absolute quantification of phosphorus metabolite concentrations in human musclein vivo by31P MRS: a quantitative review. *NMR Biomed.* **20**, 555–565 (2007).

111. Luo, Y., de Graaf, R. A., DelaBarre, L., Tannús, A. & Garwood, M. BISTRO: An outer-volume suppression method that tolerates RF field inhomogeneity. *Magn. Reson. Med.* **45**, 1095–1102 (2001).

112. Schaller, B., Clarke, W. T., Neubauer, S., Robson, M. D. & Rodgers, C. Myocardial skeletal muscle signal spoiling using a crusher coil: a human cardiac phosphorus (31P) MR spectroscopic imaging study at 7 Tesla. *J. Cardiovasc. Magn. Reson.* **17**, (2015).

113. Rodgers CT, Clarke WT, Berthel D, Neubauer S, R. M. A 16-element receive array for human cardiac 31P MR spectroscopy at 7T. In Proceedings of the 22th Annual Meeting of ISMRM. in *22nd Annual Meeting of ISMRM* (2014).

114. (ISMRM 2016) Quadrature 31P and single 1H dual-tune coil for cardiac 31P-MRS at 7T. http://archive.ismrm.org/2016/4006.html.

115. Clarke, W. T., Robson, M. D. & Rodgers, C. T. Bloch-Siegert B1+-mapping for human cardiac ^{31} P-MRS at 7 Tesla. *Magn. Reson. Med.* **76**, 1047–1058 (2016).

116. Sacolick, L. I., Wiesinger, F., Hancu, I. & Vogel, M. W. B 1 mapping by Bloch-Siegert shift. *Magn. Reson. Med.* **63**, 1315–1322 (2010).

117. Duan, Q., van Gelderen, P. & Duyn, J. Improved Bloch-Siegert based B1 mapping by reducing off-resonance shift. *NMR Biomed.* **26**, 1070–1078 (2013).

118. Clarke, W. T., Robson, M. D. & Rodgers, C. T. Bloch-Siegert B1+-mapping for human cardiac ^{31} P-MRS at 7 Tesla. *Magn. Reson. Med.* **76**, 1047–1058 (2016).

119. Robson, M. D., Tyler, D. J. & Neubauer, S. Ultrashort TE chemical shift imaging (UTE-CSI). *Magn. Reson. Med.* **53**, 267–274 (2005).

120. Rodgers, C. T. & Robson, M. D. Receive array magnetic resonance spectroscopy: Whitened singular value decomposition (WSVD) gives optimal Bayesian solution. *Magn. Reson. Med.* **63**, 881–891 (2010).

121. Purvis, L. A. B. *et al.* OXSA: An open-source magnetic resonance spectroscopy analysis toolbox in MATLAB. *PLoS One* **12**, e0185356 (2017).

122. Vanhamme, L., van den Boogaart, A. & Van Huffel, S. Improved Method for Accurate and Efficient Quantification of MRS Data with Use of Prior Knowledge. *J. Magn. Reson.* **129**, 35–43 (1997).

123. Cady, E. B. A reappraisal of the absolute concentrations of phosphorylated metabolites in the human neonatal cerebral cortex obtained by fitting Lorentzian

curves to the 31P NMR spectrum. *J. Magn. Reson.* **91**, 637–643 (1991).

124. Parasoglou, P., Xia, D., Chang, G. & Regatte, R. R. 3D-mapping of phosphocreatine concentration in the human calf muscle at 7 T: Comparison to 3 T. *Magn. Reson. Med.* **70**, 1619–1625 (2013).

125. Chmelík, M. *et al.* Flip-angle mapping of 31P coils by steady-state MR spectroscopic imaging. *J. Magn. Reson. Imaging* **40**, 391–397 (2014).

126. Cavassila, S., Deval, S., Huegen, C., van Ormondt, D. & Graveron-Demilly, D. Cramér-Rao bounds: an evaluation tool for quantitation. *NMR Biomed.* **14**, 278–283 (2001).

127. Brown, M. B. & Forsythe, A. B. Robust Tests for the Equality of Variances. *J. Am. Stat. Assoc.* **69**, 364–367 (1974).

128. Bakermans, A. J. *et al.* Human Cardiac 31P-MR Spectroscopy at 3 Tesla Cannot Detect Failing Myocardial Energy Homeostasis during Exercise. *Front. Physiol.* **8**, 939 (2017).

129. Abozguia, K. *et al.* Metabolic Modulator Perhexiline Corrects Energy Deficiency and Improves Exercise Capacity in Symptomatic Hypertrophic Cardiomyopathy. *Circulation* **122**, 1562–1569 (2010).

130. Lamb, H. J. *et al.* Reproducibility of Human Cardiac31P-NMR Spectroscopy. *NMR Biomed.* **9**, 217–227 (1996).

131. Delabarre, L., Neubauer, S., Robson, M. D., Vaughan, J. T. & Rodgers, C. T. B 0 SHIMMING FURTHER IMPROVES HUMAN CARDIAC P-MRS AT 7 TESLA. in *ISMRM 23rd Annual Meeting* (2015).

132. BSE procedure guidelines for the clinical application of stress echocardiography, recommendations for performance and interpretation of stress echocardiography. *Heart* **90**, 23–30 (2004).

133. Dass, S. *et al.* Development and validation of a short 31P cardiac magnetic resonance spectroscopy protocol. *J. Cardiovasc. Magn. Reson.* **12**, P123 (2010).

134. Betim Paes Leme, A. M. *et al.* Exercise-Induced Decrease in Myocardial High-Energy Phosphate Metabolites in Patients With Chagas Heart Disease. *J. Card. Fail.* **19**, 454–460 (2013).

135. Valkovič, L. *et al.* Using a whole-body 31P birdcage transmit coil and 16-element receive array for human cardiac metabolic imaging at 7T. *PLoS One* **12**, e0187153 (2017).

136. Nielsen, R. *et al.* Cardiovascular Effects of Treatment With the Ketone Body 3-Hydroxybutyrate in Chronic Heart Failure Patients. *Circulation* **139**, 2129–2141 (2019).

137. Boudina, S. & Abel, E. Diabetic cardiomyopathy, causes and effects. *Rev Endocr Metab. Disord* **11**, 31–39 (2010).

138. Scheuermann-Freestone, M. *et al.* Abnormal Cardiac and Skeletal Muscle Energy Metabolism in Patients With Type 2 Diabetes. *Circulation* **107**, 3040–3046 (2003).

139. Chatham, J. C. & Seymour, A. M. L. Cardiac carbohydrate metabolism in Zucker diabetic fatty rats. *Cardiovasc. Res.* **55**, 104–112 (2002).

140. Sidell, R. J. *et al.* Thiazolidinedione treatment normalizes insulin resistance and ischemic injury in the Zucker fatty rat heart. *Diabetes* **51**, 1110–1117 (2002).

141. Stanley, W. Regulation of energy substrate metabolism in the diabetic heart. *Cardiovasc. Res.* **34**, 25–33 (1997).

142. Taegtmeyer, H., McNulty, P. & Young, M. E. Adaptation and maladaptation of the heart in diabetes: Part I. General concepts. *Circulation* vol. 105 1727–1733 (2002).

143. Tune, J. D., Yeh, C., Setty, S., Zong, P. & Downey, H. F. Coronary blood flow control is impaired at rest and during exercise in conscious diabetic dogs. *Basic Res. Cardiol.* **97**, 248–257 (2002).

144. Haag, M. & Dippenaar, N. G. Dietary fats, fatty acids and insulin resistance: short review of a multifaceted connection. *Med. Sci. Monit.* **11**, RA359-67 (2005).

145. Ramos-Roman, M. A., Lapidot, S. A., Phair, R. D. & Parks, E. J. Insulin activation of plasma nonesterified fatty acid uptake in metabolic syndrome. *Arterioscler. Thromb. Vasc. Biol.* **32**, 1799–808 (2012).

146. Villarroya, F., Iglesias, R. & Giralt, M. PPARs in the control of uncoupling proteins gene expression. *PPAR Res.* **2007**, (2007).

147. Murray, A. J., Anderson, R. E., Watson, G. C., Radda, G. K. & Clarke, K. Uncoupling proteins in human heart. **364**, 1786–1788 (2004).

148. Berg, J. M., Tymoczko, J. L. & Stryer, L. The Regulation of Cellular Respiration Is Governed Primarily by the Need for ATP. (2002).

149. Taggart, A. K. P. *et al.* {(d)-β-Hydroxybutyrate} Inhibits Adipocyte Lipolysis via the Nicotinic Acid Receptor {PUMA-G}. *J Biol Chem* **280**, 26649–26652 (2005).

150. Sato, K. *et al.* Insulin, ketone bodies, and mitochondrial energy transduction. *{FASEB} J.* **9**, 651–658 (1995).

151. Clarke, K. *et al.* Kinetics, safety and tolerability of {(R)-3-hydroxybutyl} {(R)-3-hydroxybutyrate} in healthy adult subjects. **63**, 401–408 (2012).

152. Balasse, E. O. Kinetics of ketone body metabolism in fasting humans. *Metabolism* **28**, 41–50 (1979).

153. Robinson, A. M. & Williamson, D. H. Physiological roles of ketone bodies as substrates and signals in mammalian tissues. *Physiological Reviews* vol. 60 143–187 (1980).

154. Scheuermann-Freestone, M. *et al.* Abnormal cardiac and skeletal muscle energy metabolism in patients with type 2 diabetes. *Circulation* **107**, 3040–3046 (2003).

155. Ellis, J., Valkovič, L., Purvis, L. A. B., Clarke, W. T. & Rodgers, C. T. Reproducibility of human cardiac phosphorus MRS (^{31} P-MRS) at 7 T. *NMR Biomed.* **32**, e4095 (2019).

156. van der Kemp, W. J. M. *et al.* Adiabatic multi-echo ^{31} P spectroscopic imaging

(AMESING) at 7 T for the measurement of transverse relaxation times and regaining of sensitivity in tissues with short T_2* values. *NMR Biomed.* **26**, 1299–1307 (2013).

157. Runge, J. H. *et al.* 2D AMESING multi-echo 31P-MRSI of the liver at 7T allows transverse relaxation assessment and T2-weighted averaging for improved SNR. *Magn. Reson. Imaging* **34**, 219–226 (2016).

158. Van Der Kemp, W. J., Stehouwer, B. L., Luijten, P. R., Aaj Van Den Bosch, M. & Klomp, D. W. *Detection of alterations in membrane metabolism during neoadjuvant chemotherapy in patients with breast cancer using phosphorus magnetic resonance spectroscopy at 7 Tesla*. http://www.springerplus.com/content/3/1/634 (2014) doi:10.1186/2193-1801-3-634.

159. van der Kemp, W. J. M. *et al.* Adiabatic multi-echo ^{31}P spectroscopic imaging (AMESING) at 7 T for the measurement of transverse relaxation times and regaining of sensitivity in tissues with short T_2* values. *NMR Biomed.* **26**, 1299–1307 (2013).

160. Garwood, M. & Ke, Y. Symmetric pulses to induce arbitrary flip angles with compensation for rf inhomogeneity and resonance offsets. *J. Magn. Reson.* **94**, 511–525 (1991).

161. van der Kemp, W. J. M., Klomp, D. W. J. & Wijnen, J. P. ^{31}P T_2s of phosphomonoesters, phosphodiesters, and inorganic phosphate in the human brain at 7T. *Magn. Reson. Med.* **80**, 29–35 (2018).

162. Tesiram, Y. A. Implementation equations for HSn RF pulses. *J. Magn. Reson.* **204**, 333–339 (2010).

163. Park, J.-Y. & Garwood, M. Spin-echo MRI using π/2 and π hyperbolic secant pulses. *Magn. Reson. Med.* **61**, 175–187 (2009).

164. Hwang, T. L., Van Zijl, P. C. M. & Garwood, M. Broadband Adiabatic Refocusing without Phase Distortion. *Journal of Magnetic Resonance* vol. 124 250–254 (1997).

165. Moore, J., Jankiewicz, M., Zeng, H., Anderson, A. W. & Gore, J. C. Composite RF pulses for B1+-insensitive volume excitation at 7 Tesla. *J. Magn. Reson.* **205**, 50–62 (2010).

166. Moore, J., Jankiewicz, M., Anderson, A. W. & Gore, J. C. Slice-selective excitation with B 1+ -insensitive composite pulses. *J. Magn. Reson.* **214**, 200–211 (2012).

167. Pauly, J., Le Roux, P., Nishimura, D. & Macovski, A. Parameter relations for the Shinnar-Le Roux selective excitation pulse design algorithm (NMR imaging). *IEEE Trans. Med. Imaging* **10**, 53–65 (1991).

168. Somai, V., Wright, A. J., Fala, M., Hesse, F. & Brindle, K. M. A multi spin echo pulse sequence with optimized excitation pulses and a 3D cone readout for hyperpolarized ^{13}C imaging. *Magn. Reson. Med.* **84**, 1895–1908 (2020).

169. Pauly, J., Le Roux, P., Nishimura, D. & Macovski, A. Parameter relations for the Shinnar-Le Roux selective excitation pulse design algorithm (NMR imaging). *IEEE Trans. Med. Imaging* **10**, 53–65 (1991).

170. Bogner, W. *et al.* Assessment of ^{31} P relaxation times in the human calf muscle: A comparison between 3 T and 7 T in vivo. *Magn. Reson. Med.* **62**, 574–582 (2009).

171. Moore, J., Jankiewicz, M., Anderson, A. W. & Gore, J. C. Evaluation of non-selective refocusing pulses for 7 T MRI. *J. Magn. Reson.* **214**, 212–220 (2012).

172. (ISMRM 2018) Whole-body 7T 31P birdcage transmit coil driven by a 35kW RF amplifier with an integrated 30-element 31P receive array and an 8-element 1H transmit/receive array. http://archive.ismrm.org/2018/0143.html.

173. Andrew, E. R. & Gaspar, R. Mechanisms of31P relaxation in phosphorus metabolites. *Magma Magn. Reson. Mater. Physics, Biol. Med.* **2**, 421–423 (1994).

174. Thomsen, C., Jensen, K. E. & Henriksen, O. 31P NMR measurements of T2 relaxation times of metabolites in human skeletal muscle in vivo. *Magn. Reson. Imaging* **7**, 557–559 (1989).

175. Jung, W.-I. *et al.* 31P Transverse Relaxation Times of the ATP NMR Signals of Human Skeletal Muscle in Vivo. *Magn. Reson. Med.* **28**, 305–310 (1992).

176. Straubinger, K. *et al.* Spin-echo methods for the determination of 31P transverse relaxation times of the ATP NMR signals in vivo. *Magn. Reson. Imaging* **12**, 121–129 (1994).

177. Y. Sui, H. X., T. Claiborne & K. R. Thulborn, and X. J. Z. Relaxation Time Measurements of 31P Metabolites in Human Muscle at 9.4 Tesla. in *ISMRM* (2011).

178. Jung, W.-I. *et al.* 31P transverse relaxation times of ATP in human brainin vivo. *Magn. Reson. Med.* **30**, 741–743 (1993).

179. Lei, H. *et al.* 31P-31P coupling and ATPT2 measurement in human brain at 7T. *Magn. Reson. Med.* **50**, 656–658 (2003).

180. Lei, H., Zhu, X.-H., Zhang, X.-L., Ugurbil, K. & Chen, W. In vivo31P magnetic resonance spectroscopy of human brain at 7 T: An initial experience. *Magn. Reson. Med.* **49**, 199–205 (2003).

181. van der Kemp, W. J. M. *et al.* Proton and phosphorus magnetic resonance spectroscopy of the healthy human breast at 7 T. *NMR Biomed.* **30**, e3684 (2017).

182. van der Kemp, W. J. M. *et al.* Glycerophosphocholine and Glycerophosphoethanolamine Are Not the Main Sources of the In Vivo31P MRS Phosphodiester Signals from Healthy Fibroglandular Breast Tissue at 7 T. *Front. Oncol.* **6**, 29 (2016).

183. Stehouwer, B. L. *et al.* 31P magnetic resonance spectroscopy of the breast and the influence of the menstrual cycle. *Breast Cancer Res. Treat.* **144**, 583–589 (2014).

184. Dorst, J., Borbath, T., Ruhm, L., Avdievich, N., & Henning, A. 31P Transversal Relaxation Times in the Human Brain at 9.4T. in *ISMRM & SMRT Virtual Conference & Exhibition* (2020).

185. Apps, A. *et al.* Quantifying the effect of dobutamine stress on myocardial Pi and pH

in healthy volunteers: A ^{31} P MRS study at 7T. *Magn. Reson. Med.* mrm.28494 (2020) doi:10.1002/mrm.28494.

186. Clarke, W., Lukas Hingerl, L., Bogner, W., Valkovic, L. & Rodgers, C. 31P-MRSI of the human heart in 2 ½ minutes at 7T using concentric rings (CONCEPT). in *ISMRM 28th Annual Meeting* (2020).